UNIVERSIDADE FEDERAL DE SANTA MARIA
CENTRO DE CIÊNCIAS NATURAIS E EXATAS
PROGRAMA DE PÓS-GRADUAÇÃO EM FÍSICA

Vanessa Lorenzoni

EVOLUTION OF CENTRAL GALAXIES IN MASSIVE HALOS

Santa Maria, RS
2024

Vanessa Lorenzoni

EVOLUTION OF CENTRAL GALAXIES IN MASSIVE HALOS

Tese de Doutorado apresentada ao Programa de Pós-Graduação em Física, Área de Concentração em Astronomia, da Universidade Federal de Santa Maria (UFSM, RS), como requisito parcial para obtenção do grau de **Doutora em Física**.

ADVISOR: Prof. Sandro B. Rembold

COADVISOR: Prof. Reinaldo R. de Carvalho

Santa Maria, RS
2024

Vanessa Lorenzoni

EVOLUTION OF CENTRAL GALAXIES IN MASSIVE HALOS

Tese de Doutorado apresentada ao Programa de Pós-Graduação em Física, Área de Concentração em Astronomia, da Universidade Federal de Santa Maria (UFSM, RS), como requisito parcial para obtenção do grau de **Doutora em Física**.

Approved on February 09, 2024

Sandro B. Rembold, Dr. (UFSM)
(President/Advisor)

Ignacio Ferreras, Dr. (IAC)

Thiago Signorini Gonçalves, Dr. (UFRJ)

Rogemar Andre Riffel, Dr. (UFSM)

Jaderson da Silva Schimoia, Dr. (UFSM)

Santa Maria, RS
2024

ABSTRACT

EVOLUTION OF CENTRAL GALAXIES IN MASSIVE HALOS

AUTHOR: Vanessa Lorenzoni
ADVISOR: Sandro B. Rembold
CO-ADVISOR: Reinaldo R. de Carvalho

Central galaxies of spheroidal morphology experience specific evolutionary processes due to their privileged location in the center of massive dark matter halos. This is reflected in differences between their physical properties and those of non-central spheroidals of comparable stellar mass. Such processes, however, are not well understood, in particular regarding their impact on the development of the baryonic content of central galaxies. Understanding how centrals evolve will help to understand the physical mechanisms that dominate the core region of clusters. This study focus on trying to understand how the baryonic content of central galaxies evolves and how both external (driven by interaction with environment) and internal mechanisms participate in this process. For this purpose, we investigate the stellar populations and the interstellar medium (ISM) in 15,107 early-type central galaxies from the SPIDER survey by using optical spectra from the Sloan Digital Sky Survey - DR12. We investigate the stellar age (Age) and metallicities (Z), using a stellar population synthesis code and also estimate the [α/Fe] abundance ratio to constrain their star formation history. Visual extinction ($A_{\rm V}$) and Hα emissions are measured to characterize the properties of the ionized gas. In order to obtain information about radio-loud nuclear activity on central galaxies we investigate the radio luminosity ($L_{\rm R}$) using radio photometric data from the VLA FIRST survey. The main goal is to analyze systematic differences between these properties as a function of halo mass ($M_{\rm halo}$) and velocity dispersion (σ) for isolated centrals (ICs) and group centrals (GCs). Our results reveals that the stellar populations and gas properties of ICs and GCs are primarily influenced by σ, with $M_{\rm halo}$ playing a secondary role. Higher σ values correlate with older, more metal-rich stellar populations and shorter star formation timescales in both ICs and GCs. At fixed σ values, younger ages are observed at higher $M_{\rm halo}$ values regardless of the environment. For $A_{\rm V}$ and equivalent width Hα (EWHα), both parameters decrease with increasing σ and increase with $M_{\rm halo}$ in ICs. We also explore the ionization sources of warm gas and propose that ionized gas properties result from a confrontation between intracluster medium (ICM) cooling and Active Galactic Nuclei (AGNs) feedback, assuming a Bondi accretion regime. In ICs, our model successfully reproduces observed EWHα values. By including radio emission data in our analysis, we find a trend between radio and optical emissions originated by nuclear activity. Using the $L_{\rm R}$ as an indicator of AGN kinetic power instead of the Bondi scenario in our model, we successfully reproduce Hα emission in the case of ICs more accurately than previously. However, this model fails to adequately describe EWHα values in GCs, suggesting more complex interactions beyond AGN-ICM dynamics in these galaxies. Overall, we observe inherent differences between ICs and GCs, suggesting that the ratio between AGN kinetic power and ICM thermal energy influences EWHα in ICs. Meanwhile, gas deposition in GCs appears to involve a more complex interplay beyond a singular AGN–ICM interaction.

Keywords: galaxies: active – galaxies: evolution – galaxies: clusters: general - (galaxies:) cooling flows

LIST OF FIGURES

LIST OF TABLES

LIST OF ABBREVIATIONS

AGN	*Active Galactic Nucleus*
SMBH	*Supermassive Black hole*
FWHM	*Full Width at Half Maximum*
LINER	*Low-Ionization Nuclear Emission-Line Region*
QUASAR	*Quasi-Stellar Radio Source*
SF	*Star-Forming*
SDSS	*Sloan Digital Sky Survey*
ETG	*Early-type Galaxies*
LTG	*Late-type Galaxies*
IC	*Isolated Central Galaxies*
GC	*Group Central Galaxies*
BO	*Butcher–Oemler*
ICM	*Intra-Cluster Medium*
ISM	*Interstellar Medium*
RPS	*Ram Pressure Stripping*
DM	*Dark Matter*
BCG	*Brightest Cluster Galaxies*
FR	*Fanaroff-Riley*
HERG	*High-Excitation Radio Galaxies*
LERG	*Low-Excitation Radio Galaxies*
SHMR	*Stellar-to-Halo-Mass Relation*

LIST OF SYMBOLS

Gyr	10^9 years
Myr	10^6 years
$Z_\odot$	Solar metallicity (0.0177)
kpc	10^3 parsec (1 pc$= 3.086 \times 10^{16}$ m)
$L_\odot$	Solar luminosity (3.83×10^{26} W)
$M_\odot$	Solar mass (1.9891×10^{30} kg)
Å	Ångström (10^{-10} m)
Jy	Jansky (10^{-26}W/m^{2}Hz)

CONTENTS

1 INTRODUCTION

According to the standard cosmological model (ΛCDM), only 5% of the mass-energy content of the Universe is in the form of baryonic matter, while the contributions of dark matter (DM, the nature of which is still unknown) and dark energy (DE) amount to 27% and 68% respectively. What makes cosmology remarkably challenging is that most of what we know comes from this tiny little 5%, which means stars, gas, dust, etc. The second most dominant component, DM, dominates the dynamics of galaxies, groups and clusters of galaxies and it is solely detected by its gravitational effect. It is important to stress that we measure this gravitational pull by assessing the photons emitted by those objects forming the baryonic component. Groups and clusters cover a wide range of mass, 10^{12} to $10^{15}\,M_{\odot}$, and are dominated by DM (contributing with 80% of their dynamical mass), with the baryonic component being concentrated in galaxies and in the intra-cluster medium (ICM). Groups and clusters are ideal systems for studying how galaxies evolve in response to their environment. From the central region to the outskirts, the local galactic density varies by seven orders of magnitude while velocity dispersion drops by ∼15%. In galaxy clusters, a variety of dynamical processes, including merging and tidal encounters, are likely to occur, significantly influencing the evolution and properties of the galaxies within these environments.. The ICM, in the form of a hot ($T \sim 10^8$ K, Takizawa (2000)) plasma, can also play an important role in shaping the stellar and gas content of the galaxies in such environments, particularly those at the centers of clusters. Central galaxies are subjected to many physical processes such as gravitational interactions and the accretion of cold gas from the ICM which significantly influence their morphological structures and star formation rates. These objects become pivotal in our understanding of how environmental processes within clusters drive galaxy evolution. This work focuses on the study of the central galaxies in clusters by means of optical-infrared and radio observations. Understanding how centrals evolve will help grasping the physical mechanisms responsible for the buildup of the stellar content in the central region of clusters and groups role of active galactic nuclei (AGN) feedback, one of the key elements of current investigations.

1.1 GROUPS AND CLUSTERS OF GALAXIES

When we observe the Universe on large scales ($\gtrsim 10$ Mpc), we find that galaxies are not randomly distributed but rather aggregated into distinct structures. These include smaller, low-mass systems known as *Groups*, comprising a few dozen galaxies, and the more massive *Clusters*, encompassing hundreds of galaxies. The mass range of these structures extends from approximately 10^{12} to $10^{15} M_{\odot}$, (Erfanianfar et al., 2019; Cimatti; Fraternali; Nipoti, 2019), with density contrasts significantly higher than the overall galaxy density in both cases (see

Figure 1.1). There is no clear separation between groups and clusters; for this reason, several studies investigating the properties of galaxies in these systems look for trends with halo mass. Their high surface density make them easy to identify even at higher redshifts ($z \sim 1$). This is why they are useful not only as cosmological probes but also to investigate the galaxy population. Hubble & Humason (1931) were the first to notice that denser environments (clusters) were dominated by early-type systems, paving the way to the morphology-density relation later properly established by Dressler (1980). Figure 1.2 displays this fundamental relation, which shows that the fraction of late-type galaxies drops from $\sim$60% in the periphery of clusters to 10% in their centers. The early-type galaxies show the opposite behavior. Dressler et al. (1997) extended the study to $0.37 \leq z \leq 0.56$ clusters and found evidence that a certain degree of morphological segregation happens hierarchically influencing richer, denser groups of galaxies earlier; even more important, it seems that early-type galaxies are formed before the cluster itself, probably in the loose groups phase. They also find that lenticular galaxies were profusely formed only after the parent cluster is virialized.

Figure 1.1 – Central region of the cluster Abell 2261. A dominant elliptical galaxy, referred to as *central galaxy*, is seen at the cluster core; the remaining galaxies are called *satellites*. Credit: NASA; ESA; M. Postman, STScI; T. Lauer, NOAO, Tucson; CLASH team.

The radial number density distribution of galaxies in clusters has been studied by several authors over the years (e.g. van der Marel et al., 2000) and they find consistency with the DM halo profile put upfront by Navarro, Frenk & White (1997) in terms of both the profile shape and the characteristic scale length, reassuring that galaxies seem to trace the mass distribution in clusters. However, there is an additional observation to consider. As previously mentioned, there is some segregation based on mass and morphology/color. More massive, red, early-type

galaxies follow a more concentrated number density distribution than less massive, blue, late-type galaxies (e.g. Carlberg et al., 1997; Adami et al., 1998; van den Bosch et al., 2008). This indicates that while galaxies generally trace the DM distribution in clusters, this correlation must be interpreted with an awareness of the segregation effects based on galaxy mass and type/color. Butcher & Oemler A. (1984), using photometric observations of 33 clusters, find a significant increase in the fraction of blue galaxies (many with disturbed morphology) at the central region of high redshift galaxy clusters when compared to the nearby ones. This relation, known as the Butcher–Oemler (BO) effect, indicates intense star formation activity in clusters at higher redshift (Couch et al., 1994). Besides, current observations show that in the last 1-2 Gyr star formation is being quenched, a clear indication that the population of galaxies in clusters is rapidly evolving with redshift.

The dominant baryonic content in galaxy clusters, the hot gas in the ICM, is responsible for a diffuse X-ray emission which, given the high temperatures, is dominated by thermal Bremsstrahlung. Due to X-ray emission, the gas loses its pressure and thermal energy and consequently cools. Gravity plays its role, taking this cooled gas towards the cluster potential well in a process called *cooling flow* (Fabian, 1994). The compression of this cold gas by the overlying gas weight would initiate an intense star formation. However, many authors modeling cold gas found that the star formation rate at the center of clusters is lower than predicted by a factor of $\sim 10-100$ times (McNamara; O'Connell, 1989; Cardiel; Gorgas; Aragon-Salamanca, 1998). In view of this problem, Molendi & Pizzolato (2001) suggested referring to clusters with high central density as *cool core* (CC) clusters. Thus, the name reflects only an observational fact rather than an inferred physical property, the flow. The characterization of cool core clusters include a low central entropy and a systematic central temperature drop, differently from non-cool core (NCC) clusters, which appear to be isothermal with no strong signs of cooling (Cavagnolo et al., 2009; Cimatti; Fraternali; Nipoti, 2019). Besides, CC clusters present, in general, circular symmetry, indicating a virialized system. On the other hand, NCC clusters seem to be at an earlier stage of the dynamic relaxation process, being more dispersed and asymmetrical. This dichotomy naturally leads us to the question: what is the mechanism behind the dichotomy between CC and NCC clusters? The answer is still unknown. Recent studies suggest that mergers play a significant role in this classification (Ritchie; Thomas, 2002; Valdarnini; Sarazin, 2021). It is believed that NCC clusters are (or have been recently) undergoing a merger process (Cimatti; Fraternali; Nipoti, 2019), which can disrupt cold cores through a process called *ram pressure* (see Sect. 1.2) (Gomez et al., 2000). If NCC and CC clusters are in different stages of relaxation, it is natural to wonder how the galaxies that compose them are affected. In the next section, we review some well-known environment physical processes responsible for changing galaxies physically and morphologically.

Figure 1.2 – Fraction of elliptical, lenticular and spiral+irregular galaxies as a function of projected density. The plot shows the morphology-density relation, where early-type galaxies tend to be found in denser regions while late-type ones present the opposite behavior (Dressler, 1980).

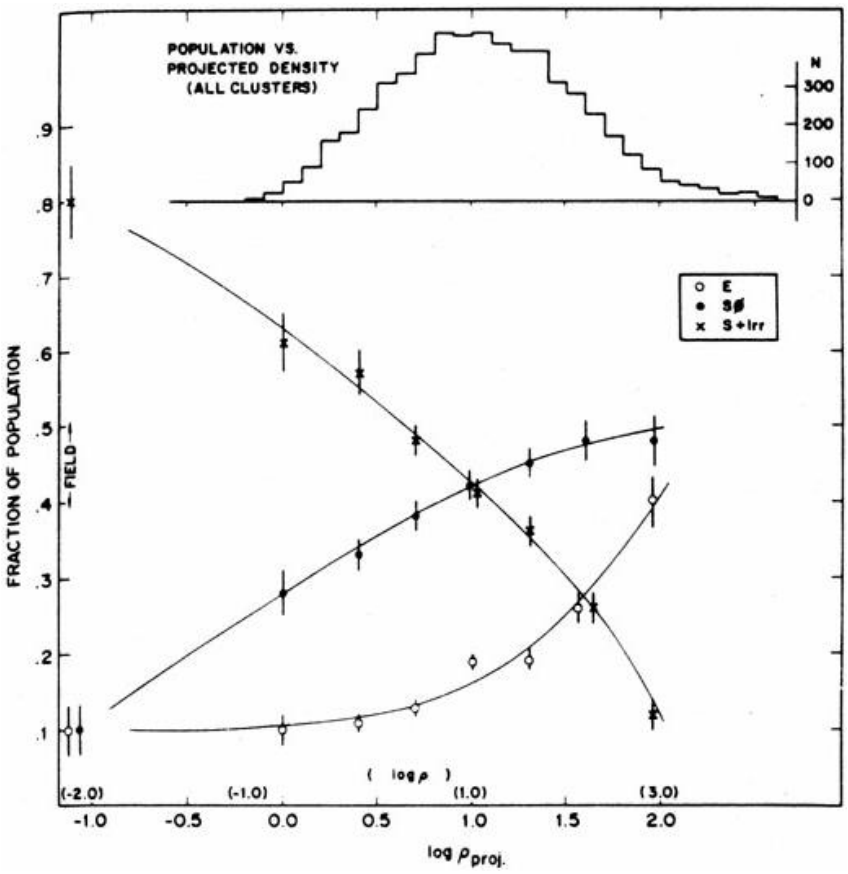

1.2 HOW DO GALAXIES IN CLUSTERS EVOLVE?

As discussed in Sect. 1.1, galaxies in clusters have a consistent dependence on the environment. Once they enter or become part of a denser environment, they can undergo physical and morphological transmutations. Such processes usually include the loss of their gas reservoir and their gas cooling capacity, which explains the dominance of early-type galaxies in clusters. In general, these mechanisms can be divided into three main scenarios: tidal interactions and interactions with the ICM. Processes related to these three classes will be discussed in the next subsections.

1.2.1 Tidal interactions

One of the most popular scenarios associated to tidal interactions, galaxy harassment is probably the main mechanism behind of the BO effect in clusters (Moore et al., 1996). In this scenario, many galaxies are moving at velocities of several thousand $\mathrm{km\,s^{-1}}$, turning the

interplay between galaxies very common and fast. As a result of these high-speed encounters, galaxies can change their morphology, often inducing new bursts of star formation, transforming low-luminosity cluster galaxies into disturbed spirals (Bialas et al., 2015). This gravitational interaction can cause the formation of "tidal tails" and other deformations in the mass distribution (Moore et al., 1996), making the involved galaxies more vulnerable to disruptions by further encounters and by tidal interactions with the global potential of the cluster. When fragile disks spirals participate, they experience a loss of large amounts of mass as impulsive heating pushes the stars into free orbits. Stars that remain attached to the galaxy are also heated, resulting in a spheroidal component much like a dwarf elliptical. Therefore, the dwarf elliptical galaxies observed in nearby clusters are likely to be remnants of disk galaxies that suffered galaxy harassment (Farouki; Shapiro, 1981; Moore et al., 1996).

Interactions between galaxies are very common in galaxy clusters. The relation between velocity dispersion and density (Bahcall, 1981) implies that in the clusters outskirts (lower density regions) velocity dispersion decreases which favors the coalescence. Besides, high-speed encounters that cause tidal tails, galaxies can incorporate each other in a process called galaxy merger. Depending on the size of the galaxies involved in this process, the merger is called "minor" or "major". A minor merger, or galactic cannibalism, refers to the scenario where smaller galaxies are consumed by a much larger companion. This type of merger stands out when it comes to the evolution of central galaxies. These massive galaxies, residing close to the clusters potential well, consume smaller galaxies that are driven in their direction through a process called dynamical friction (Ostriker; Hausman, 1977a; Chandrasekhar, 1943), resulting in an increase in their size, mass and amount of gas. In contrast, a major merger happens when two galaxies of approximately the same size collide and merge into a single object. When this type of merger happens between spirals galaxies, it may drive off much of the dust and gas of the original galaxies through feedback mechanisms, resulting in an elliptical galaxy. This process is thought to be one of the main mechanisms responsible for formation of elliptical galaxies (Toomre; Toomre, 1972), often found in clusters.

1.2.2 Interactions with the ICM

Galaxies are believed to be surrounded by substantial amounts of hot/warm gas at halo. Over time this gas eventually cools and falls towards the galaxy disk. This cold gas deposition allows galaxies to continue forming new stars. When a galaxy falls into a cluster, this hot gas reservoir can be lost due to environmental processes (e.g. ram pressure, tides by the main cluster potential (Fujita 1998), etc.). Without their gas supply, the galaxy will not be able to keep forming stars so longer.

Star formation will continue until the galaxy runs out of available cold gas, and this time there will be no source to replace it. The loss of the galaxy source of cold gas, resulting

in a gradual star formation quenching, is called strangulation or starvation (Larson; Tinsley; Caldwell, 1980; Peng; Maiolino; Cochrane, 2015; Trussler et al., 2018). During this phase the gas metallicity increases more steeply due to the lack of inflowing gas. The stellar mass also increases slightly. The general product of strangulation is a quiescent galaxy with a stellar metallicity significantly higher than its star forming progenitor, and slightly higher stellar mass. This process also contributes, even on longer timescales, to transforming galaxies that fall into clusters into red and passive ones.

Interactions between galaxies and the gas pressure of the ICM are sometimes strong enough to overcome the galaxy gravity and remove its dust and gas. The removal of the interstellar medium (ISM) from the galaxy, instantly stopping the star formation process, is called ram pressure stripping (RPS - Gunn; Gott J. Richard, 1972). Galaxies undergoing this process may have their dust and gas distributions skewed to one side of the galaxy, indicating that the galaxy is unable to shield its ISM completely from the "wind".

RPS is often invoked to explain why dense environments have a clear deficit of gas-rich, star-forming galaxies. Steinhauser, Schindler & Springel (2016) show that this process is efficient in removing the hot gas halo. Without its gas reservoir the galaxy cannot replenish its cold gas and therefore form new stars, leading the galaxy to a morphological transformation. Meanwhile, cold disks are remarkably resistant to RPS, not being removed easily. Ricarte et al. (2020) suggest that ram pressure is capable not only of extinguishing star formation but is also responsible for triggering enhanced accretion into the galaxy's supermassive black hole (SMBH). Feedback from the nuclear activity induced by the accretion process can, in turn, aid in quenching star formation (see Sect. 1.3.1), in cooperation with ram pressure. Being capable of removing (most of) the ISM of (and quenching star formation in) galaxies, this process may explain why clusters contain a larger fraction of early-type galaxies.

Indeed, an accreted galaxy is likely to suffer tidal effects and to interact with the ICM. As described in this section, these environmental mechanisms change the properties of galaxies in clusters, transforming their physical and morphological properties. However, the impact of each one is still an open question. In the next section we describe in more detail how central galaxies of clusters can be affected by the environment and its internal processes.

1.3 CENTRAL GALAXIES

Close to the center of thermalized clusters, one usually finds a dominant massive galaxy, referred to as *central galaxy* (e.g. Hashimoto; Henry; Boehringer, 2014). Even in clusters at an earlier stage of dynamic relaxation, we can identify a central galaxy as the galaxy endowed with the most massive DM sub-halo (Yang et al., 2011). Usually characterized by a spheroidal mor-

phology (see Figure 1.1), central galaxies are the most massive ($\sim 10^{13}\,M_{\odot}$; Dressler, 1979) and luminous galaxies of the local Universe ($L \sim 10^{11} h^2 L_{\odot}$; e.g. Sandage & Hardy (1973), Schombert (1986). Central galaxies (i.e. the most massive galaxy in a halo) generally correspond to Brightest Cluster Galaxies (BCGs). Such population of galaxies, besides their large masses, present distinct physical properties when compared to non-central spheroidal galaxies with similar mass, probably due to their privileged location.

Being ~ 10 times more luminous than an ordinary elliptical galaxy (Katayama et al., 2003), central galaxies do not follow a simple extrapolation of the luminosity function defined by other cluster members (Dressler, 1978). Their surface brightness profiles are characterized by higher values of the Sérsic index n (which can reach up more than 3 orders of magnitude) than elliptical galaxies in general (Graham; Guzmán, 2003; Donzelli; Muriel; Madrid, 2011; Bai et al., 2014), and follow a distinct Faber-Jackson relation (Von Der Linden et al., 2007). Centrals are more likely to be radio–loud than other galaxies of the same stellar mass (by a factor of up to 10) and present higher [α/Fe] ratios (~ 0.1 orders of magnitude) – indicating that their stars may have formed over a shorter time interval – and less intense optical emission lines (Von Der Linden et al., 2007). Moreover, they have little rotational support (Von Der Linden et al., 2007) and, particularly when they are part of massive clusters, often present peripheral light envelopes of a stellar nature unseen in conventional elliptical galaxies, constituting the cD morphological type (Dressler, 1979; Zhao; Aragón-Salamanca; Conselice, 2015a, 2015b). Massive central galaxies are characterized by an old stellar population ($\sim 10^{10}$ yr - La Barbera et al., 2014), with few or no star formation and, for the most part, high metallicity ($[Z/H] \sim 0.31$ - Loubser et al., 2009).

We can classify central galaxies as group/cluster centrals, i.e. massive galaxies in the center of host halos containing satellites (galaxies in the cluster other than the central) or as field (or isolated) centrals, when the host halos do not contain massive satellites which are expected to be less affected by external physical processes. Comparing both classes, group/cluster centrals are redder and more massive than centrals located in halos without satellites. Also, at a fixed velocity dispersion, field centrals have older ages, higher [α/Fe] ratios, and lower internal reddening than centrals in groups/clusters (La Barbera et al., 2014). La Barbera et al. (2014) also found that stars in central galaxies are younger in more massive halos, suggesting that cluster centrals formed their stellar component on longer timescales than isolated centrals. Zhao, Aragon-Salamanca and Conselice (2015a) also showed that more massive BCGs tend to inhabit denser regions and more massive clusters than lower mass BCG. These studies suggest that the assembly history of centrals must be told differently depending on the combination of galaxy mass and DM halo mass. Another connection between centrals and their host clusters is the alignment observed between them. In clusters with well-defined orientations in the optical, the orientation of the major axis of centrals tends to align significantly with the host cluster's major axis (Carter; Metcalfe, 1980; Plionis; Tovmassian; Andernach, 2009; Ragone-Figueroa et al., 2020), reinforcing the evidence that the evolution of centrals depends on their environment.

Studies suggest that central galaxies assemble most of the stellar mass at relatively early times during virialization of their host halos (Merritt, 1985; Ruszkowski; Springel, 2009; Nipoti, 2017). De Lucia & Blaizot (2007) found that the stars in these systems start forming very early: about 50% of the stars in these systems have already formed by redshift $z \sim 5$, although the centrals as we see today are assembled from and after $z \sim 0.7$. All these properties indicate that centrals may have quite an unusual formation history compared to ordinary elliptical galaxies. However, it is still unclear how the process of formation and evolution of these galaxies occurs, as it involves many internal and external processes. Such processes include transformation of gas into stars, feedback processes, merging between galaxies, cooling flow, etc.

In the literature, several well-known scenarios have been proposed to explain the assembly of the stellar content in central galaxies. These include major mergers during cluster collapse within a hierarchical cosmological scenario (Merritt, 1985); galactic cannibalism, which involves minor mergers or the accretion of galaxies into an existing system (Ostriker; Hausman, 1977a), a process facilitated by dynamical friction that draws galaxies towards the cluster potential well; and star formation triggered by cooling flows, typically expected to occur in cluster centers (Fabian, 1994). Galactic mergers was proposed to explain the formation of central galaxies by Merritt (1983), Aragon-Salamanca, Baugh & Kauffmann (1998). In the galactic merger scenario centrals obtain most of their masses through mergers between several massive galaxies which take place in groups or low-mass clusters in the early times of the formation of massive galaxy clusters. Major mergers are invoked to explain the growth in stellar mass in centrals by Lidman et al. (2013, 2012). Lidman et al. (2013), analyzing the contribution to the stellar mass growth of BCGs by mergers between bright satellite galaxies and the central galaxy found a major merger rate of 0.38 ± 0.14 events per Gyr at $z \sim 1$. The authors argue that if this rate of major mergers remains until the present time ($z \sim 0$) and if half of the mass of the accreted galaxies is added to the BCG in this process, the growth of the stellar mass of the BCG could mostly explained via major mergers. However, it is well known that other mechanisms also contribute to the growth of these objects. The inclusion of minor mergers between centrals with gas-poor galaxies (dry mergers) together with the major mergers scenario helps explain the observed growth in size in these galaxies since $z = 2$ (Laporte et al., 2013). The idea of galactic cannibalism, according to White (1976) and Ostriker & Hausman (1977b), offers an explanation for how cD galaxies form. In this process, a central galaxy slowly absorbs smaller ones around it, which are pulled into the cluster center by dynamical friction. These smaller galaxies add their stars mainly to the outer parts of the bigger galaxy, causing it to grow in size and mass.

As discussed in Sect. 1.2.1, it is common for satellite galaxies to be accreted by the central galaxy, so it is reasonable that this process needs to be included in the assembly history of centrals. Also, satellites are expected to be gas poor and passive (i.e, non-star forming galaxies) due to the environmental processes described in Sect. 1.2. So, the contribution for the growth of central galaxies by galactic cannibalism is expected to be dominated by dry mergers. Minor and

major merging are important mechanisms behind the assembly of the stellar content in central galaxies. Other mechanisms, however, can also participate in this process, like the capture of gas from the ICM into centrals and the feedback from nuclear activity, which we now discuss.

1.3.1 Active Galactic Nuclei

Active Galactic Nuclei (AGN), are luminous, compact regions at the centers of galaxies, whose emission is of a non-stellar nature. The mechanism responsible for such emission, following Antonucci (1993) and Urry & Padovani (1995), involves the accretion of matter by a SMBH at the galaxy center. This process leads to the formation of an accretion disk, where the intense gravitational forces heat the matter, leading to significant energy emission across the electromagnetic spectrum.

The distinction between AGNs based on their radio emissions has given rise to two main categories: radio-loud (RL) AGNs – galaxies with intense radio emissions ($L_{1.4\,\mathrm{GHz}} > 10^{23}\,\mathrm{W\,Hz^{-1}}$), exhibit either a compact or large scale relativistic jet and lobes (Wilson; Colbert, 1995), and radio-quiet (RQ) AGNs – galaxies with little or no radio emission (Silpa et al., 2020). AGNs are further differentiated into more specific categories such as Seyferts, QUASARs, Blazars, LINERs, and Radio Galaxies, based on detailed analyses of their spectral characteristics, including emission lines and continuum features. As central galaxies are more likely to be radio galaxies we discuss this type of AGN in more detail.

In radio galaxies, nuclear activity is primarily distinguished by the presence or absence of jets. The existence of these jets is attributed to synchrotron radiation from charged particles as they move through strong magnetic fields. When large-scale jet emissions are absent, it indicates a lower rate of matter accretion into the SMBH, leading to a reduced amount of energy available to sustain the jets. The morphologies of extended jets and lobes in radio-loud AGN are classified into two main different classes known as Fanaroff-Riley (FR) dichotomy (Fanaroff; Riley, 1974). In the first class, FR I, galaxies display radio jets that are brightest near the central galaxy and gradually fade with distance. In the second class, FR II galaxies feature jets that are initially faint near the center but dramatically increase in brightness at greater distances, forming hotspots at the edges of the lobes (see Figure 1.3). Recently, Baldi, Capetti & Giovannini (2015) suggested a third class FR 0. FR 0 consists of the radio galaxies which shares all the properties of FR Is except prominent extended radio emission. This morphological differentiation is closely linked to the dichotomy between High-Excitation Radio Galaxies (HERGs) and Low-Excitation Radio Galaxies (LERGs). According to Hine & Longair (1979), they are distinguished by the absence or presence, and the relative importance, of emission lines in their optical spectra. HERGs are marked by high excitation rates and strong spectral line emissions, indicating the presence of efficient accretion disks fueled by cold gas (Hardcastle; Evans; Croston, 2007). These galaxies tend to be associated with FR II types and

are more frequently observed at high redshifts. Conversely, LERGs, with their lower excitation rates and less prominent spectral emissions, are generally fueled by hot gas (Bondi accretion – Bondi, 1952) and are more commonly found in nearby galaxies. The accretion mechanisms in these galaxies also differ significantly. HERGs are associated to high accretion rates and intense emissions. LERGs, however, may exhibit an advection-dominated accretion regime, characterized by a less efficient conversion of gas energy into radiation.

The energy released by the AGN in the form of radiation or jets is called AGN feedback and is often divided into quasar and radio mode. The quasar mode feedback is radiatively efficient and occurs when the SMBH accretes at rates near the Eddington limit[1]. On the other hand, the radio mode feedback is associated with lower accretion rates onto the SMBH. In this mode, the feedback is predominantly mechanical and it is characterized by the emission of powerful jets that extend well beyond the galaxy. Both types of AGN feedback are thought to significantly impacts the surrounding environment, affecting both the host galaxy and the ICM (in the context of clusters of galaxies). In the quasar mode, intense radiation and powerful winds from matter accretion onto the SMBH can heat and expel gas from the host galaxy, reducing star formation rate. Additionally, this mode helps regulate the SMBH growth by expelling gas and limiting future accretion material. In the radio mode, relativistic particle jets emitted from the SMBH poles extend over vast distances, interacting with the ICM. The mechanical energy of these jets heats the surrounding medium, preventing the collapse and condensation of gas into new stars.

Understanding the dynamics of AGN feedback in both the quasar and radio modes is crucial for comprehending how SMBHs are fed in different galactic environments. The nature of AGN feedback, whether radiatively efficient as seen in quasar mode or mechanically dominant in radio mode, is intrinsically linked to the SMBH accretion mechanism. Understanding the dynamics of AGN feedback in both the quasar and radio modes is crucial for comprehending how SMBHs are fed in different galactic environments. The nature of AGN feedback, whether radiatively efficient as seen in quasar mode or mechanically dominant in radio mode, is intrinsically linked to the SMBH accretion mechanism. Cold mode accretion involves gas condensing into clouds and filaments, then falling towards the SMBH, fueling the AGN. In contrast, the Bondi model is a key reference for interpreting SMBH mass accretion where SMBHs accrete from hot, quasi-spherical interstellar mediums, meaning the gas is drawn uniformly from all directions towards the SMBH. In this model, the SMBH accretes, or draws in, material from its surrounding environment when its gravitational pull surpasses the thermal energy of that material. In this scenario, the critical region for accretion is defined by the Bondi radius. This radius marks the boundary where the gravitational influence of the SMBH becomes stronger than the internal pressure of the gas, leading to an inward flow of material. The rate at which the SMBH accretes mass from its surroundings, known as the Bondi accretion rate, depends on

[1]The Eddington Limit is the maximum luminosity an object can achieve at which its radiation pressure and the gravitational force on the gas are in equilibrium.

several factors: the mass of the SMBH, the density and temperature of the surrounding gas, and the speed of sound within that gas. Such accretion is radiatively inefficient and often controlled by mechanical feedback like radio jets. Since Bondi model emphasis on spherical symmetry, it provides crucial insights into SMBH feeding mechanisms in elliptical galaxies, then we will delve deeper into this topic in the next section.

Figure 1.3 – Left panel: This image shows the radio morphology of a FR I radio galaxy (NGC 383) at $z = 0.0169$. Right panel: Radio morphology of a FR II radio galaxy (Quasar 3C175) at $z = 0.76$. Both images are from Very Large Array 1.4 GHz image at $5.5''$ resolution. Credit: Legacy Astronomical Images, "Radio Galaxy 3C31" and "Radio Quasar 3C175", NRAO/AUI Archives.

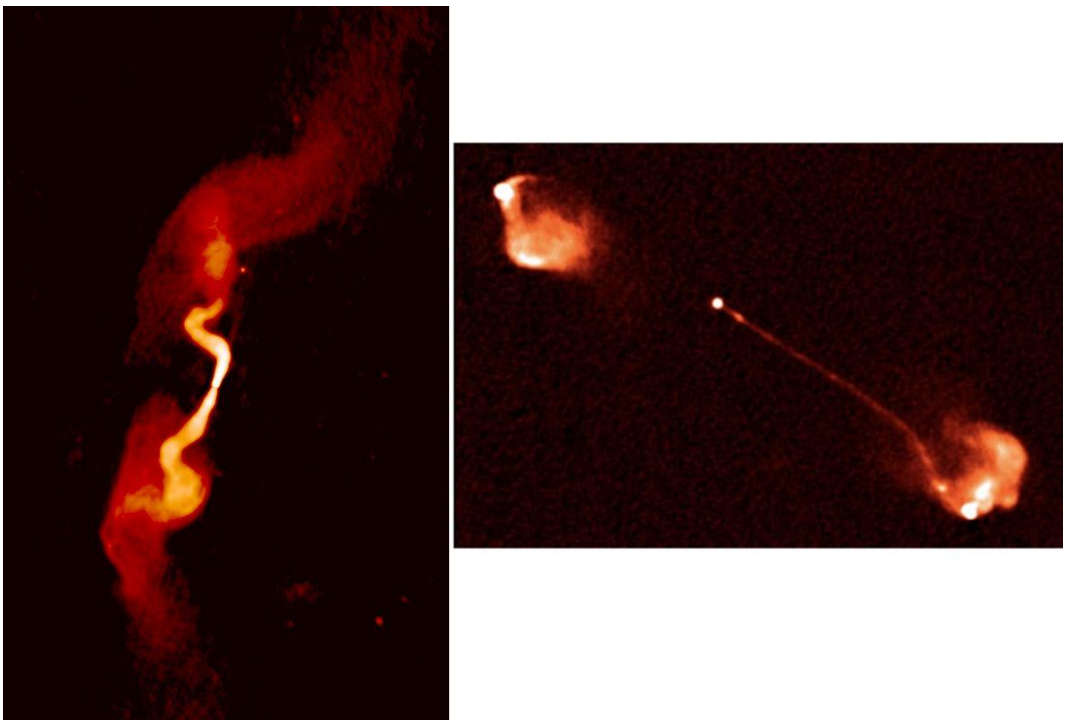

1.3.2 Interplay between the ICM and central galaxies

As discussed in the Sect. 1.1, the cooling of ICM gas by X-ray emission drives cold gas to the central regions of the cluster, giving the central galaxy the possibility to form new stars. This scenario of star formation via cooling flow is supported by a number of studies such as McNamara et al. (1996), who found blue and ultraviolet light excesses in a sample of central galaxies, indicating active star formation in the cluster core. Another indication is the discovery of cold molecular gas associated to the cooling flow and Hα-emitting filaments produced by young stars via photoionization close to center of clusters (Salomé; Combes, 2004; Revaz; Combes; Salomé, 2008; Salomé et al., 2006; McDonald et al., 2010), as show in Figure 1.4.

The classical cooling flow model (described in Sect. 1.1) predicts that the ICM gas should lose most of its thermal energy and pressure support by 10-100 Myr and present cooling rates reaching up to $\sim$1,000 $M_{\odot}$ year^{-1}, resulting in a huge amount of cold gas and stars in the cluster center (Fabian, 1994), which is not observed (McNamara; O'Connell, 1989). Actually, centrals are seen to form stars at a rate of approximately 1% of the predicted value by the cooling flow scenario (O'Dea et al., 2008; McDonald et al., 2010, 2011). This suggests that the ICM is reheated by some mechanism (Fabian, 1994). Many studies suggest that feedback from active galactic nuclei can explain this heating (Gaspari; Brighenti; Ruszkowski, 2013).

Figure 1.4 – Left panel: contours of CO emission, tracing cold gas in Perseus cluster. Right panel: filaments of Hα emission in the same cluster (Hα image with the same scale of left panel), Credit: Salomé et al. (2006), Conselice, Gallagher John S. & Wyse (2001)

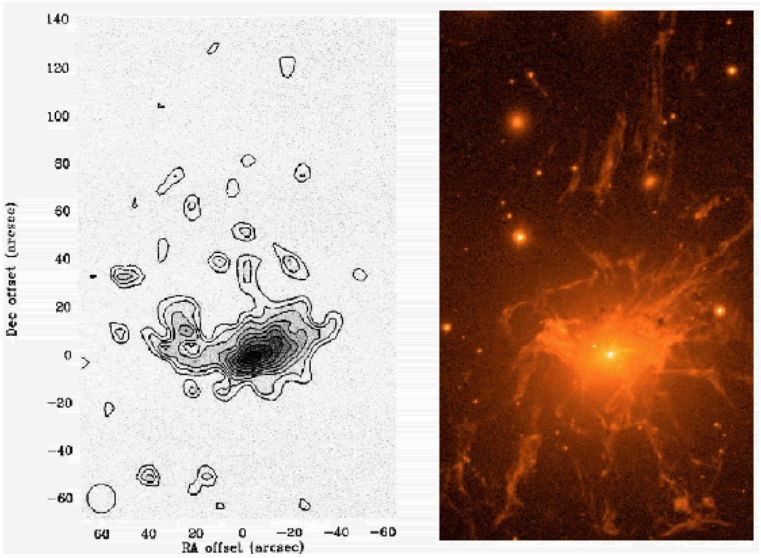

A number of observational studies show signatures in X-ray cavities in the ICM that are often filled with lobes of radio-emitting plasma (McNamara; Nulsen, 2007) – see Figure 1.5. This spatial coincidence suggests that radio jets are removing gas from the galaxy and regulating their star formation (Chon et al., 2012; Pasini et al., 2021; Tiwari; Singh, 2022). Therefore, the "cooling flow problem" could be explained by this mechanism (Stott et al., 2012; Croton et al., 2006; Vagshette et al., 2017). This would also explain the large values of [α/Fe] in massive galaxies as a result of suppression of star formation, preventing iron from long-lived intermediate-mass stars to be incorporated into new generations of stars.

The accretion mode efficiency to produce powerful jets capable of creating X-ray cavities is still discussed in the literature. McNamara, Rohanizadegan & Nulsen (2011) and Voit & Donahue (2015) argue that the Bondi accretion mode is not capable of producing jets powerful enough to regulate star formation, being the accretion by cold gas responsible for this phenomenon. In contrast, we find that the ionized gas emission in central galaxies is well described by a model that involves the Bondi accretion mechanism, producing a good relation between the emission-line features and both halo and galaxy masses (Lorenzoni; Rembold;

de Carvalho, 2024). Also, studies claim that the Bondi accretion rates and the power of jets associated with the SMBHs are correlated (Allen et al., 2006; Balmaverde, Baldi, & Capetti 2008; Fujita, Kawakatu & Shlosman, 2014). In short, AGN feedback is a mechanism capable of expelling gas from the galaxy and also preventing the ICM from cooling through interaction with jets, preventing centrals from forming new stars (eg Fabian 1999; Granato et al. 2004; Di Matteo et al. 2005; Hopkins et al. 2006).

Figure 1.5 – Multi-wavelength imaging of the central galaxy Hercules A (top panel). In visible light (bottom left panel), Hercules A looks like a typical elliptical galaxy. In X-rays (bottom middle panel), this galaxy is seen as a giant cloud which has been heated by AGN feedback. Radio light (bottom right panel) shows jets of particles streaming away from the black hole. Credit: Credit: X-ray: NASA/CXC/SAO; visual: NASA/STScI; radio: NSF/NRAO/VLA.

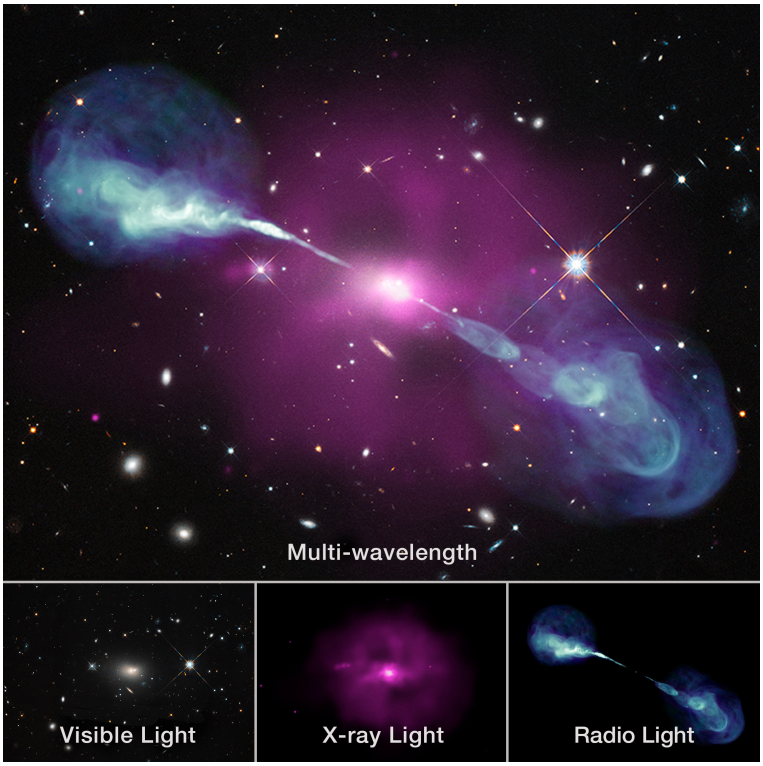

1.4 OBJECTIVES

We have seen in the previous sections that many studies on the development of central galaxies have already been done. We also describe some of the physical processes that participate in their assembly history which are cooling flow, mergers (minor, major, involving gas or not) and AGN feedback. This work focuses on early-type central galaxies in low redshift ($0.05 \leq z \leq 0.095$), how these objects develop their baryonic content, and how both external (driven by interactions with the environment) and internal mechanisms participate in this process. Our goal is to help answering the following questions: (1) What are the relative

contributions of internal and external processes to the baryonic mass assembly of central galaxies? (2) How do central galaxies develop their baryonic content depending on the environment in which they are located and their own mass? (3) How efficient is radio-mode AGN feedback in stopping star formation and how efficient is the cooling flow process in achieving the opposite effect? (4) How does the AGN feedback from central galaxies influence its surroundings, and how does that influence depend on how massive its host halo is? In order to address such questions, our specific objectives are:

- To study the properties of the stellar populations of early-type central galaxies in different environments (isolated and group systems), deriving mean stellar ages and metallicities, for different ranges of galaxy and halo mass, using the stellar population synthesis method.
- To measure the [α/Fe] abundance ratio in order to constrain the star formation history of central galaxies;
- To use radio photometric data in order to obtain information about radio-loud AGN activity on central galaxies, mapping the relative intensities as a function of galaxy and halo mass;
- To measure the emission line fluxes and equivalent widths, characterizing the properties of the ionized gas through diagnostic diagrams, and analyzing systematic differences as a function of environment and galaxy mass.

This thesis is structured as follows. In chapter 2 we present our sample of central galaxies and the spectrophotometric data that will be used in the work, as well as the characterization of the central galaxies environment. We also discuss the methodology of analysis, including the stellar population synthesis, α-enhancement measurements, the use of the diagnostic diagrams to classify the origin of gas emission and the analysis of radio emission. In chapter 3 the results are presented, the discussion in chapter 4 and finally, the conclusions are presented in chapter 5.

2 DATA AND METHODS

2.1 SAMPLE SELECTION

Our sample is derived from the SPIDER I (Spheroid's Panchromatic Investigation in Different Environmental Regions) survey (La Barbera et al., 2010), comprising a sample of 39,993 Early-Type Galaxies (ETGs) with redshifts spanning the range 0.05 to 0.095, extracted from the Sloan Digital Sky Survey Data Release 6 (Adelman-McCarthy et al., 2008, SDSS-DR6). We impose an absolute Petrosian magnitude limit criterion in the r-band of $M_r < -20$, which serves to delineate the separation between "bright" and "ordinary" elliptical galaxies, in accordance with Capaccioli, Caon & D'Onofrio (1992), Graham & Guzmán (2003). Notably, this threshold closely aligns with the upper redshift limit of $z = 0.095$, coinciding with the completeness of SDSS spectroscopic observations. The establishment of a lower redshift limit plays a pivotal role in reducing potential biases caused by the aperture effect in our measurements.

Our selection process for ETGs aligns with the criteria set forth by La Barbera et al. (2010). Specifically, we utilize the SDSS attribute $fracDev_r > 0.8$ to identify bulge-dominated systems and the attribute $eClass < 0$ for spectral classification through principal component analysis decomposition. Additionally, we carefully select objects with velocity dispersion (σ) exceeding $100\,\mathrm{km\,s^{-1}}$ to exclude low-mass ETGs. To minimize the influence of lenticular galaxies, we exclude those with minimal internal extinction ($E(B-V) < 0.1\,\mathrm{mag}$). We also apply signal-to-noise ratio (S/N) criteria to spectra in the H_β spectral region, requiring thresholds of 14, 27, and 21 for $\sigma = 100$, 200, and $300\,\mathrm{km\,s^{-1}}$, respectively. These S/N thresholds are chosen to match the lower quartile within their respective σ bins. To ensure the reliability of our morphological classification, we cross-reference our galaxy sample with the Galaxy Zoo project (Lintott et al., 2011). However, given the incomplete nature of the Galaxy Zoo classifications, we supplement our selection criteria by considering the quality of the two-dimensional Sérsic fits to the surface brightness distribution, as detailed in La Barbera et al. (2014). In summary, our final sample comprises 20,977 ETGs with optical spectra, along with the corresponding σ values and associated uncertainties ($\sigma_{\rm err}$) extracted from SDSS-DR12 (Alam et al., 2015). Notably, the uncertainties in σ typically remain well below $10\,\mathrm{km\,s^{-1}}$, except for a small subset of 95 central galaxies, where the maximum $\sigma_{\rm err}$ value reaches $\sim 14\,\mathrm{km\,s^{-1}}$. This minor difference is not significant in the context of the overall central galaxy sample.

2.2 USING OPTICAL DATA FROM SDSS

The Sloan Digital Sky Survey is a five-passbands (u, g, r, i and z) imaging and medium-resolution ($R \sim 2000$) spectroscopic survey. SDSS started operations in 2000 and is currently in its fifth stage (SDSS-V). It uses a 2.5 m telescope located at the Apache Point Observatory in southern New Mexico (Gunn et al., 2006). We extracted the SDSS DR12 (Alam et al., 2015) optical spectra to use in the analysis of the stellar population properties (stellar age and metallicity, etc.) of our sample of central galaxies. Besides, will be used in the measurements of emission lines to determine sources of ionization of gas in these galaxies and to characterize the star formation timescale from measurements of α enhancement. DR12 imaging and optical spectroscopic observations cover a total area of 14,555 deg^2 covering predominantly the northern hemisphere. The coverage of the southern hemisphere is more sparse and concentrated close to the celestial equator.

The twelfth data release *ugriz* imaging includes almost half a billion unique objects being a total of 2,401,952 galaxies. The exposure time per band is 53.9 s and typical full width at half maximum (FWHM) of the Point Spread Function (PSF) is $1.3''$. For the r-band, the relative photometric calibration accuracy (RMS) (Padmanabhan et al., 2008) is 0.8 % the wavelength has 95% completeness and a magnitude limit of 22.2. The camera consists of two arrays, a photometric array that uses 30 2048 $\times$ 2048 SITe/Tektronix CCDs (24 μm pixels) with an effective imaging area of 720 cm^2 and an astrometric array that uses 24,400 $\times$ 2,048 CCDs with the same pixel size. The pixel scale is $0.396''$.

The SDSS DR12 provides a total of 4,266,444 useful optical spectra with wavelength spaced on a logarithmic scale ranging from 3,800 to 9,200 Å with resolution of 1,500 at 3,800 Å and 2,500 at 9,000 Å. The spectra are integrated within a aperture $3''$ diameter around the center of each galaxy. Measurements are made using an aluminum plate that is placed in the focal plane of the telescope. This plate is pre-drilled where it corresponds to the positions of objects in the sky, so each area of the sky requires a new plate. The optical fibers are plugged into each hole bring the light from the focal plane to the pseudoslit of the spectrographs. Then, the SDSS spectrum is identified by the plate used to collect the spectrum, by MJD, an integer that denotes the Modified Julian Date of the night when the observation was carried out and by the FiberID that denotes the fiber number (1 to 640).

2.3 CHARACTERIZATION OF THE GALAXY HOST ENVIRONMENT

We characterize the environment that hosts the central galaxies in our sample using the Yang Catalog (Yang et al., 2007, hereafter Y07). This catalog is constructed by applying a halo mass-finding algorithm to the New York University Value-Added Galaxy Catalog (Blanton et al., 2005, NYU-VAGC). Within this catalog, galaxies that share a common DM halo are grouped

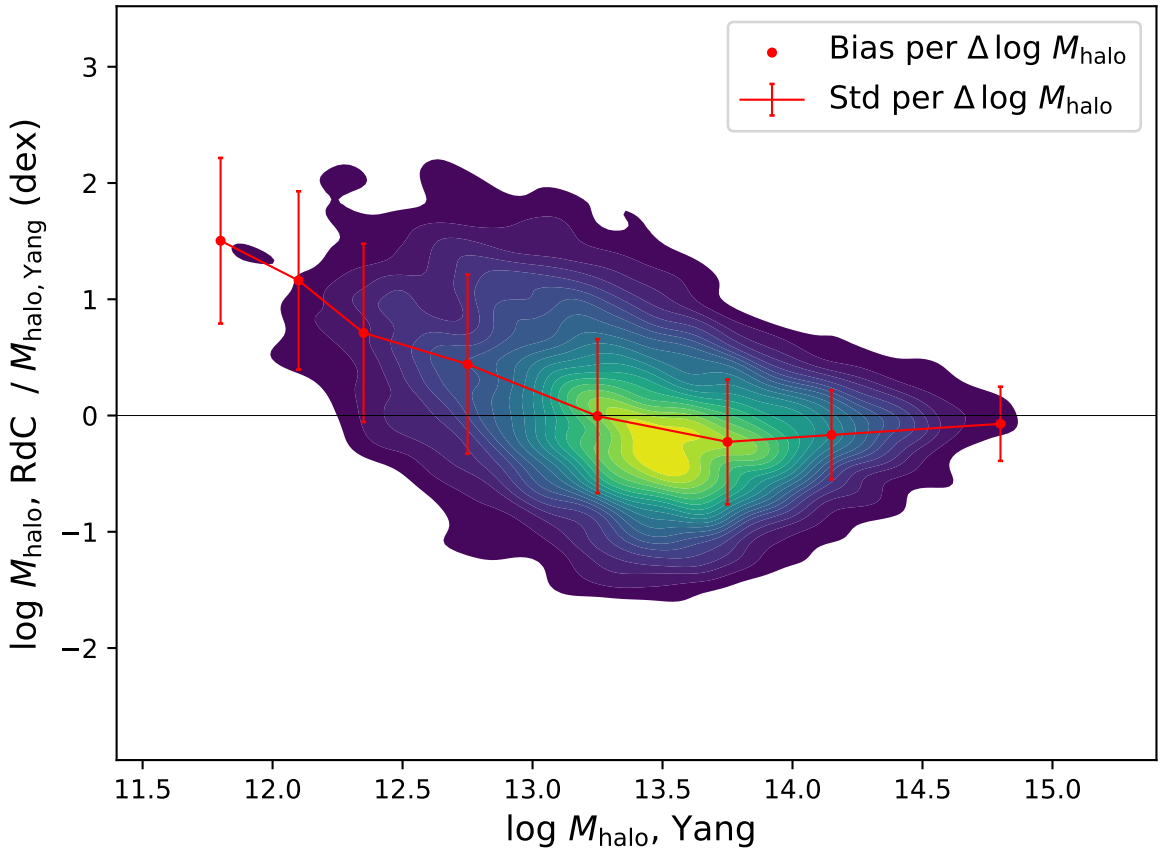

Figure 2.1 – Comparison between the halo mass measurements obtained by de Carvalho et al. (2017) and by Yang et al. (2007). The dots and lines indicate the bias and standard deviation for specific halo mass ranges, respectively.

and classified as either satellite or central galaxies based on their stellar mass.

Central galaxies are identified as the most massive galaxy within the DM halo and are categorized into two groups: 1) isolated centrals (IC), occupying a single DM halo without other galaxies, and 2) group centrals (GC), sharing a DM halo with other satellite galaxies. Different evolutionary processes may influence the physical properties of ICs and GCs. Hence, we analyze these two populations separately. Y07 determines the DM halo mass ($M_{\rm halo}$) based on the total stellar mass of the group, with a threshold of $M_{\rm halo} \gtrsim 10^{12}\,{\rm h}^{-1}\,{\rm M}_{\odot}$. Excluding the satellites, our sample comprises 15,107 early-type central galaxies, of which 10,575 are ICs, and 4,532 are GCs.

The systematic errors in $M_{\rm halo}$ measurements are obtained by comparing halo masses estimated using the shift-gapper technique (de Carvalho et al., 2017) with those determined by Yang et al. (2007). The comparison, illustrated in Figure 2.1, is based on the dispersion and bias introduced by these two methods for specific ranges of the Yang halo mass ($\Delta \log M_{\rm halo}$).

2.4 STACKING GALAXY SPECTRA BY THEIR σ AND $M_{\rm halo}$

To enhance the S/N in our optical spectra, we have employed the spectral stacking method. We combined the normalized individual spectra within specific bins determined by σ and $M_{\rm halo}$. The result of this process is a stacked spectrum that represents the median of all available spectra within each bin, with redshift corrections applied.

We calculated the flux uncertainties for each wavelength by computing the standard error of the median across all contributing spectra in the final stacked spectrum. Our sample is organized into 71 stacks (full sample, i.e, mixing ICs and GCs), where σ spans from 100 to 323 $\mathrm{km\,s^{-1}}$, and $M_{\rm halo}$ ranges from $10^{11.6}$ to $10^{15.3}\,\mathrm{M_\odot}$. We adjusted the bin size for σ with increments of $10\,\mathrm{km\,s^{-1}}$, except for the highest-value bins. For $M_{\rm halo}$, we chose bin widths of 0.25, 0.40, 0.50, and 1.00 dex. We define an initial range for $M_{\rm halo}$ starting at $10^{11.6}\,\mathrm{M_\odot}$ since our sample does not include halos below this threshold. To ensure meaningful analysis, we excluded stacks with fewer than 5 galaxies, guaranteeing a representative number of objects in each stack. We also separate our sample in ICs and GCs according to Y07 classification. Isolated centrals, primarily associated with halos below $10^{13.5}\,\mathrm{M_\odot}$, occupy 54 bins of σ and $M_{\rm halo}$. In contrast, group centrals, linked to higher $M_{\rm halo}$ values, produce 60 bins. This highlights the connection between galaxy properties and DM halos, as manifested in the stellar-to-halo-mass relation (SHMR), where more massive galaxies are typically situated within more massive halos. It is important to mention that while spectral stacking increases the spectral S/N, it does result in the loss of individual galaxy signatures, providing a representative spectrum of the entire population. Detailed information about the number of galaxies and S/N per bin are provided in Tables 1, 2, and 3 in the Appendix.

2.5 STELLAR POPULATION SYNTHESIS AND EMISSION LINE MEASUREMENTS

The stellar population of a galaxy can be studied using a method called stellar population synthesis. With this method, we can obtain information about the galaxy star formation history, mean stellar age and metallicity, chemical abundance, stellar mass, mass-luminosity ratio, extinction, etc. In this work we use the spectral synthesis software named STARLIGHT (Cid Fernandes et al., 2005). The STARLIGHT code is a computational stellar population synthesis routine that compares data from an observed galaxy with a set of simple stellar population models (SSP). The routine looks for the combination of SSPs that best describes the observed spectrum, creating a model spectrum as described by

$$M_\lambda = \sum_{j=1}^{N_\star} L_{\lambda,j} = \sum_{j=1}^{N_\star} L^0_{\lambda,j} \otimes G(v_\star, \sigma_\star) 10^{-0.4 A_\lambda}, \tag{2.1}$$

where $L^0_{\lambda,j}$ is the spectrum of the j-th SSP, G is the Gaussian function centered in $v_\star$ and with

standard deviation $\sigma_\star$, and $A_{\lambda,j}$ is the extinction of j-th SSP for each wavelength.

We provide to STARLIGHT the rest-frame spectra of the observed objects extracted from SDSS data, as outlined in Sect. 2.1. We convert the binary (FITS) optical spectra to ASCII format, transform vacuum wavelengths to air wavelengths following Ciddor (1996), correct for Galactic extinction, adjust the wavelength by a factor of $1+z$, and apply a dimming correction of $(1+z)^3$ to the flux density. To match the wavelength scale of the SSPs spectra, we re-sample the SDSS spectra to a linear scale, given that they are originally spaced on a logarithmic scale.

To run, STARLIGHT requires a file containing a list and description of the SSPs (base file), a configuration file with technical parameters, a mask file indicating pixels affected by non-stellar features, and a choice of extinction law. All this information is organized in a "grid" file (the input file of STARLIGHT)[1]. An illustrative example of the STARLIGHT output is depicted in Figure 2.2. The top panel shows a comparison between an observed spectrum of our sub-sample (in black) and the model spectrum (in blue) generated by STARLIGHT. Vertical lines aid in identifying important lines in the spectrum. The model spectrum is derived as previously described, and the bottom panel displays the residual spectrum.

Figure 2.2 – Comparison between a representative stacked spectrum (black line in the top panel) and its model spectrum (blue line in the top panel) created by the STARLIGHT code. The residuals of the fit are shown in the bottom panel (black line).

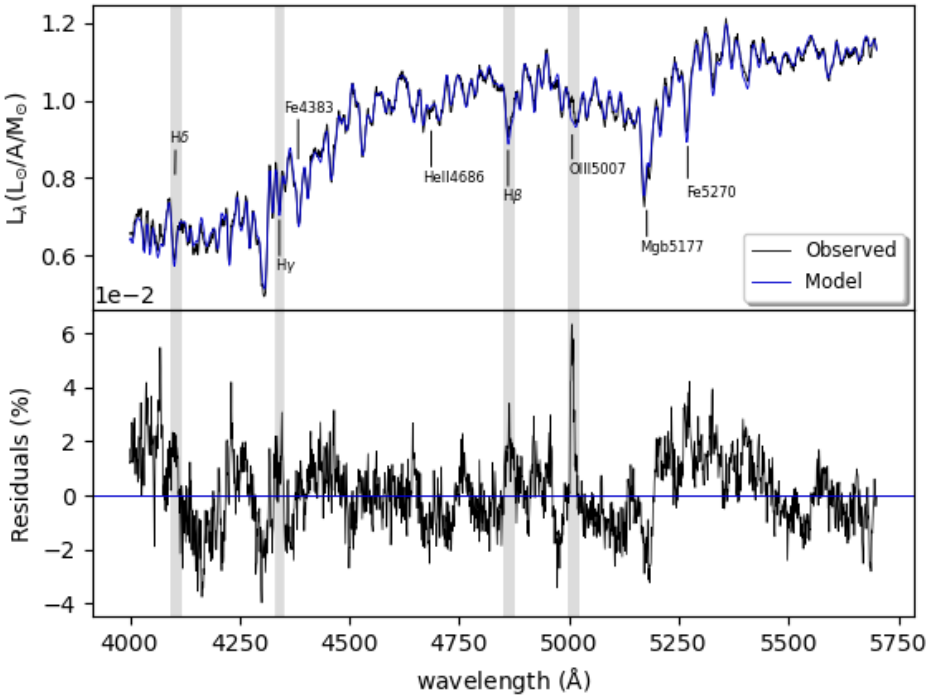

In this study, we employ 108 solar-scaled SSP models from the Medium resolution INT Library of Empirical Spectra (MILES) galaxy spectral library (Vazdekis et al., 2010). These

[1]Refer to STARLIGHT manual for details, available at http://www.starlight.ufsc.br/

models are constructed using the Kroupa universal Initial Mass Function (IMF) and encompass ages from 0.5 to 17.78 Gyr, with $Z = 0.004$, 0.008, 0.019, and 0.03. Non-solar abundance ratios in our galaxy sample are not expected to significantly affect the derived stellar population parameters, as discussed in La Barbera et al. (2014).

The MILES models have a spectral resolution of approximately 2.5 Å and span a wavelength range from 3,525 to 7,500 Å. As in La Barbera et al. (2014), we conduct the synthesis within the wavelength range from 4,000 to 5,700 Å, with 5,200 Å as the normalization wavelength. The exclusion of the spectral range above 5,700 Å is due to the presence of IMF-sensitive absorption features in this region. We apply the Cardelli, Clayton & Mathis (1989) extinction law (suitable for systems with low levels of star formation) and mask the main SDSS optical emission lines. We estimate the light-weighted Age and Z following Equations 2 and 5 from Cid Fernandes et al. (2005), while the A_V parameter is directly provided by the STARLIGHT output. In order to identify the presence of ionized gas in centrals, we have measured the equivalent width of the Hα line (EWHα). To perform this measurement, we extend the synthesis solution up to 7,000 Å to include Hα emission, then subtract synthetic and observed spectra to isolate emission lines. The Hα flux, measured by fitting Gaussian profiles, as shown in Fig 2.3, is divided by the mean stellar continuum level at the line position, obtained from the synthetic spectrum. To measure the EWHα we fitted three Gaussians simultaneously for [N,II]λ6548.05, Hα, and [N,II]λ6583.45. We fixed the center of the line to the wavelength corresponding to the measured line, and the width of each line was constrained so that all have the same width. The base of each line was defined as a straight line at the height of the continuum.

Uncertainties in the studied properties are estimated using the bootstrap method. In short, we perform a random selection of a single object among all galaxies in a given stack; this operation is repeated N times, where N is the total number of galaxies in the respective stack. In this process, not all galaxies of the stack are selected, because a given galaxy can be selected multiple times. Subsequently, the entire stack creation process is performed with the newly selected galaxies. Then, we conduct the stellar population synthesis and estimate each property mentioned before. This procedure is repeated 1,000 times for each stack. To obtain the uncertainty in the parameters, we calculate the standard deviation for each stack and property.

To ensure the reliability of our results, we also perform additional syntheses using an alternative set of SSPs, the Granada-MILES (GM) models (Cid Fernandes et al., 2013). These templates combine Granada models from González Delgado et al. (2005) (for ages younger than 63 Myr) and MILES models. The construction of the SSPs uses a Salpeter IMF and includes the evolutionary tracks by Girardi et al. (2000), with the exception of ages ≤ 3 Myr, where the Geneva evolutionary tracks are employed (Schaller et al., 1992; Schaerer et al., 1993b, 1993a; Charbonnel et al., 1993) and a spectral resolution of approximately 2.3 Å. We convolve the GM SSPs spectra to coincide the spectral resolution of the MILES models and also select only the templates with the same age and Z, enabling a direct comparison between them. We find (see Fig.1 in the Appendix) that differences in SSPs can affect stellar population parameters,

but EWHα values remain insensitive to the choice of SSP models. We are confident that the observed trends in σ and $M_{\rm halo}$ in Sect. 3 are independent of the SSPs choice.

Figure 2.3 – Gaussian fits (in orange) on the emission lines [NII]λ 6548.05, Hα and [NII]λ 6583.4 in the spectrum of a representative stack in our sample (blue line). The vertical dashed lines indicate the centers of the fitted emission lines.

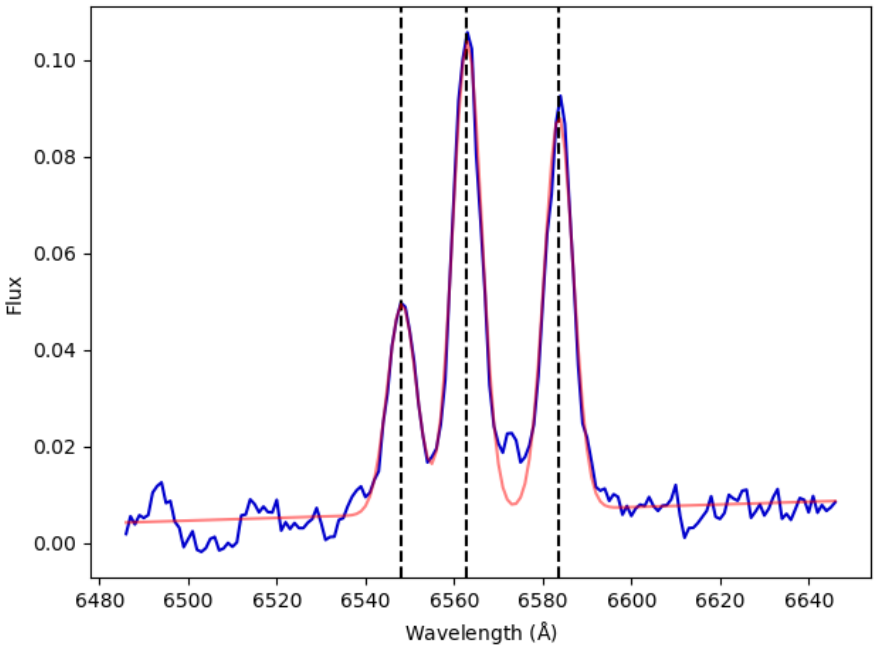

2.6 α-ENHANCEMENT AS A COSMIC CLOCK

As discussed in Sect. 1.3, central galaxies exhibit higher [α/Fe] ratios compared to ordinary elliptical galaxies, indicating that central galaxies generally do not undergo prolonged episodes of star formation. The STARLIGHT software is capable of generating [α/Fe] ratios; however, our analysis is based on SSPs with a fixed α abundance, which is set to be solar-scaled. Therefore, differences in the relative abundance of α elements and Fe between the galaxies in our sample and our SSPs will be evident in their respective spectral absorption features. Specifically, these differences will manifest as either excesses or deficits in the absorption features associated with these elements. This factor becomes critical when attempting to determine the metallicity of a galaxy from the equivalent widths of its spectral lines. If we use equivalent widths to infer metallicity and compare them with our solar-scaled SSPs, the results will differ depending if the the analysis is based on α - elements or Fe. In La Barbera et al. (2013), the [α/Fe] ratio is derived from determining metallicity using a particular α-element, Mgb, in relation to Fe. The authors demonstrated that these individual metallicities are good estimators of the [α/Fe] ratio through the equation

$$[\alpha/\mathrm{Fe}] \sim 0.55 \left[\frac{\mathrm{Z_{Mg}}}{\mathrm{Z_{Fe}}}\right] = 0.55\,([\mathrm{Z/H}]_{\mathrm{Mg}} - [\mathrm{Z/H}]_{\mathrm{Fe}}), \tag{2.2}$$

where Z_{Mg} and Z_{Fe} represent the stellar metallicities derived by measurements of the spectral index Mg*b* and Fe3, with Fe3 = (Fe4383 + Fe5270 + Fe5335) / 3. Here, Mg*b*, Fe4383, Fe5270, and Fe5335 represent the equivalent widths of absorption features at 5177, 4383, 5270, and 5335Å, respectively. Therefore, to investigate the correlation between [α/Fe], σ and M_{halo}, we adopt the same methodology employed by La Barbera et al. (2013) to estimate the [α/Fe] abundance ratio.

To calculate these metallicities, we estimate the spectral lines equivalent width using Lick index. The definition of the Lick system definition involves identifying specific spectral regions for measuring the flux of a given spectral line, i.e., the line of interest in addition to two neighboring regions necessary for establishing a pseudo-continuum. The central and continuum bandpasses for Mg*b*, Fe4383, Fe5270 and Fe5335 are displayed in Table 2.1. We perform a linear regression to fit a pseudo-continuum to the spectrum data. This fit provides an estimate of the stellar continuum in these regions. Subsequently, the equivalent width of the line is calculated by the ratio between the absorbed flux of the line and the continuum level (average flux density) at the center of the line.

We measure the Mg*b* and Fe3 indices for each stacked spectrum. Then, we chose MILES templates that closely matched the stellar ages obtained from STARLIGHT for each stacked spectrum. This process was repeated to determine the Mg*b* and Fe3 index for the template spectra. However, to accurately measure the indices for these templates, we needed to smooth the template spectra to match the resolution of each individual stacked spectrum. This step is crucial because the line indices are influenced by σ, affecting the broadening of spectral lines and thus the measurements of their fluxes. By adjusting the resolution, we ensure that the template indices are comparable with the expectations of stellar population models. In the Figure 2.4 we present the template's metallicity versus the Mg*b* index (left panel) and versus the Fe3 index (right panel). We fit a second-degree polynomial to these two relations. We then determine the metallicities Z_{Mgb} and Z_{Fe} for each stacked spectrum using these fits and the line indices measured for them. We derive the [α/Fe] values for our stacked spectra using the previously estimated metallicities into equation 2.2.

In order to check the robustness of our absorption line equivalent width measurements, we compare our results with those obtained by using the INDEXF tool – program written in C++ to measure line-strength indices in fully calibrated FITS spectra, (Cardiel, 2010).[2] The upper panels of Figure 2.5 illustrate the correlation between the Mg*b* and Fe3 measurements for GCs, derived from our method to those obtained using the INDEXF method. The scatter plots reveal a linear relation, with a dashed line indicating a good agreement between the two methods. In the lower panels, we display the residuals, which are the differences between the indices

[2]https://indexf.readthedocs.io/en/latest/description.html, for more information.

Table 2.1 – Bandpass definitions (extracted from Trager et al. (1998)) for the Lick Index System, adapted for vacuum wavelength.

Index name	Central Bandpass (Å)	Continuum Bandpasses (Å)
Mg*b*	5161.375 - 5193.675	5143.875 – 5162.625 5192.625 – 5207.625
Fe4383	4370.375 - 4421.625	4360.375 – 4371.625 4444.125 – 4456.625
Fe5270	5247.375 - 5287.375	5234.875 – 5249.875 5287.375 – 5319.875
Fe5335	5314.125 - 5354.125	5306.625 – 5317.875 5355.475 – 5365.375

measured by each method. The mean of these differences, along with their standard error, is annotated in the upper right corner of the residual plots. The magnitudes of the residuals are minor and are considered negligible relative to the spectral resolution. Then, given the demonstrated agreement with the results obtained using INDEXF, we continue by employing our current measurement method.

Uncertainties in the [α/Fe] estimates are assessed using the bootstrap method. The process of generating the stacks and measuring the [α/Fe] ratio is repeated 1,000 times to estimate the standard deviation of the measurements.

Figure 2.4 – Example of metallicity estimation using the Mg*b* and Fe3 spectral indices. The left panel displays the correlation between the Mg*b* index and the [Z/H] for the SSP. The right panel provides a comparable analysis for the Fe3 index. The green stars represent the estimated metallicities (Z_{Mgb} and Z_{Fe3}) derived from the stack spectrum.

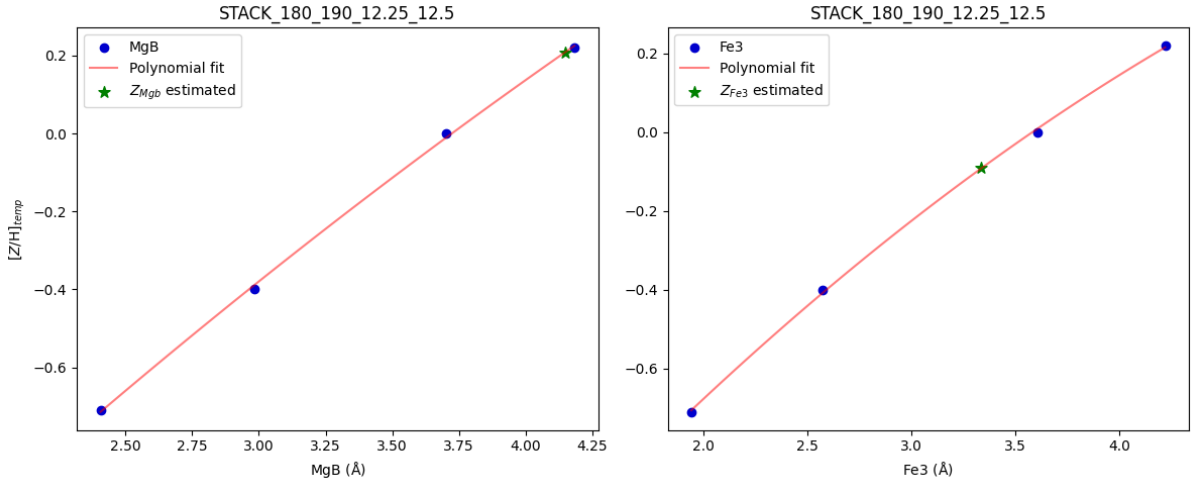

Figure 2.5 – The upper panels illustrate the comparison of Mg*b* and Fe3 measurements for GCs using our analytical approach versus the INDEXF method. In the bottom panels, we plot the residuals, representing the discrepancies between the index measurements from the two different methods. The symbols $\bar{x}$ and σ_x represent the mean value of the differences between the two methods and their respective standard error.

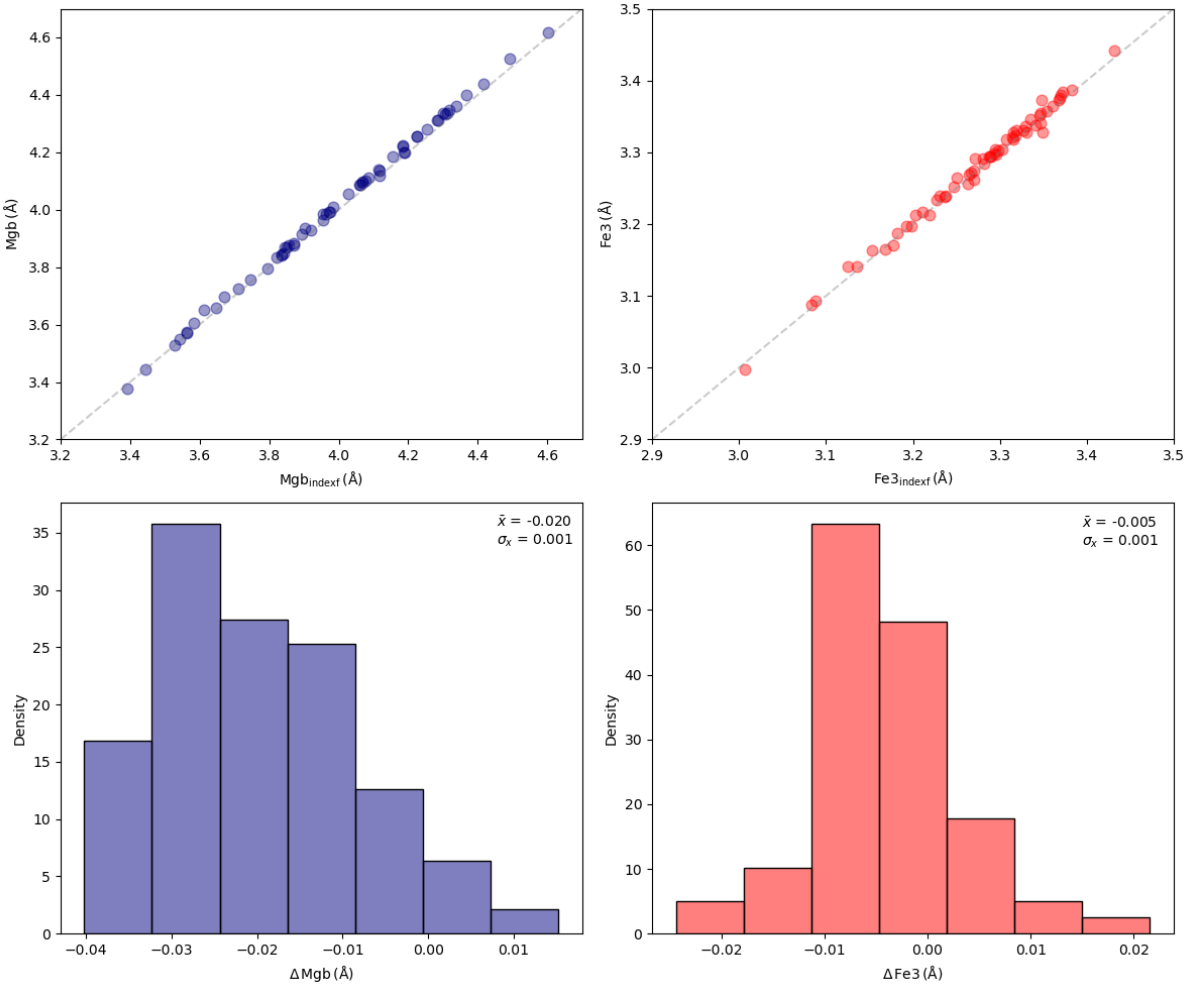

2.7 EXPLORING THE DIAGNOSTIC DIAGRAMS

The diagnostic diagrams are tools widely used for the classification of ionization sources in galaxies. The most commonly used optical diagnostic diagram, BPT diagrams (Baldwin; Phillips; Terlevich, 1981), performs a spectral classification of galaxies based on the intensity ratios of a number of emission lines. For this work, we use the BPT-NII diagram, which consists of measuring the intensity ratios [O III]λ5007/Hβ $\times$ [N II]λ6584/ Hα in order to differentiate galaxies dominated by star-forming regions (H II regions) from those ionized by AGNs.

An example of a BPT-NII diagram (which we will refer to simply as “BPT diagram”) is

presented in the left panel of Figure 2.6 for 403,015 objects described in Herpich et al. (2016). In the left panel of Figure 2.6, the purple line allows us to separate galaxies where the dominant ionization source is the AGN and those where star formation dominates, as proposed by Kewley et al. (2001). All objects to the left of this line have high levels of gas ionization, and may be purely star-forming or star-forming plus AGN (known as "composite" or "transition objects"). The curved black line delimits objects dominated by regions of star formation from composites and AGNs, being proposed by Kauffmann et al. (2003). Composites are located between the Kewley et al. (2001) and Kauffmann et al. (2003) lines. Objects below the Kauffmann et al. (2003) curve are dominated by star-forming regions. Finally, the diagonal straight black line proposed by Schawinski et al. (2007) separates low ionization (LINERs) and high-ionization active galaxies (Seyfert). Here, the high-ionization AGNs region described as Seyfert includes all optical strong AGNs, such as radio galaxies. So, throughout the text when we refer to Seyferts in the BPT diagram, we are referring to strong AGNs in general.

Over time, the diagrams were improved and adapted as a function of available ionization models and/or observations (Veilleux; Osterbrock, 1987; Osterbrock, 1989; Kewley et al., 2001; Kauffmann et al., 2003; Kewley et al., 2006; Stasińska et al., 2006; Schawinski et al., 2007). Although widely used, the BPT diagram is not efficient in separating LINERs from galaxies that do not have an active nucleus and are not forming new stars, but are ionized by hot evolved low-mass stars (HOLMES), dubbed "retired galaxies" (Cid Fernandes et al., 2011a). Using the equivalent width of Hα and the ratio [N II]λ6584/Hα, Cid Fernandes et al. (2011a) shows that this separation between retired galaxies and low luminosity AGNs can be performed, establishing a complementary diagram for the spectra classification of galaxies. This diagram is known as WHAN diagram, and the galaxies are classified as star-forming galaxies, strong AGNs, weak AGNs, retired galaxies and passive galaxies. The original separation between AGNs in the WHAN diagram is between strong AGNs and weak AGNs, but again, in the following we will refer to Seyferts as synonymous for strong AGN (same as in the BPT diagram) and LINERS for weak AGNs.

The right panel of Figure 2.6 shows the application of the WHAN diagram. We see from the distribution that the WHAN diagram is quite useful to make a separation between passive + retired galaxies and star forming + strong AGN + weak AGN, but not so efficient in separating star forming from AGNs, in which case the BPT diagram performs better. Thus, the WHAN diagram can be applied as a complementary diagram to the BPT. In this work we use both diagnostic diagrams to analyze the sources of gas ionization in central galaxies. To measure the emission lines fluxes, [OII]λ5007, Hβ and [NII]λ6584, we use the same methodology used to estimate the Hα flux in Sect. 2.5, using Gaussian fits. To measure the flux and the equivalent width of the emission lines for [N,II]λ6584 and Hα, we fitted three Gaussians simultaneously for [N,II]λ6548.05, Hα, and [N,II]λ6583.45. However, for [O,III]λ and Hβ, each Gaussian was measured individually. We fixed the center of the line to the wavelength corresponding to the measured line, and the width of each line was constrained so that all have the same width.

The base of each line was defined as a straight line at the height of the continuum.

Figure 2.6 – Example of diagnostic diagrams from Herpich et al. (2016). Left panel: BPT diagram; the black curve is the SF/AGN separator from Stasińska et al. (2006); the purple line is the 'pure AGN' classifier of Kewley et al. (2001); and the straight black line is the Cid Fernandes et al. (2010) Seyfert/LINER divisor. Right panel: WHAN diagram; the lines delimit the spectral classes defined in Cid Fernandes et al. (2011a) (Nikutta et al., 2014).

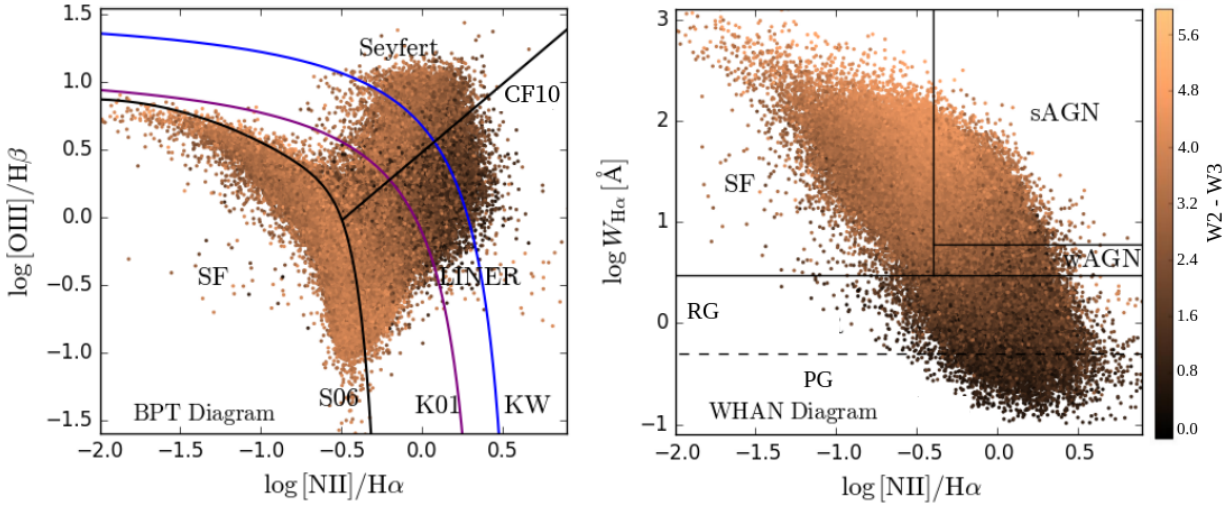

2.8 VLA FIRST RADIO DATA: SEARCHING FOR RADIO SIGNS

We aim to identify the presence of radio emissions linked to nuclear activity in the central galaxies within our sample. To achieve this, we have selected a radio survey that strikes a balance between a broad footprint, depth, and resolution. This approach is chosen to minimize the exclusion of galaxies from our sample while ensuring that we can effectively detect and analyze radio emissions indicative of nuclear activity. Therefore, we complement the optical spectrophotometry analysis we cross-match our central galaxy sample from the SDSS with radio observations from the VLA FIRST (Faint Images of the Radio Sky at Twenty-centimeters) survey (Becker; White; Helfand, 1995).

The VLA FIRST survey data includes frequencies at 1.3 and 1.4 GHz, covering around 10,575 square degrees of the sky, split between 8,444 square degrees in the northern Galactic cap and 2,131 in the southern cap. The 1.4 GHz frequency is commonly used for radio continuum observations, where we expect to find emissions derived from synchrotron radiation of relativistic electrons in galactic magnetic fields from AGNs and star-forming regions. This makes VLA FIRST an effective tool for detecting radio emissions mostly from AGNs in our galaxy sample (see discussion on the star formation history of our sample of central galaxies in Sect. 3.1).

The FIRST images have a pixel scale of $1.8''$/pixel and a resolution of $\sim 5''$, and the typical local noise estimate at the source position (rms) is 0.15 mJy. The detection limit is 1 mJy in most of the survey area and the astrometric accuracy of each source is $0.5 - 1''$ at the source detection threshold. As the detection threshold of the VLA FIRST survey is shallow (~ 1 mJy), even some radio galaxies will not have their radio counterparts. To achieve a confidence level of 3σ, galaxies need to satisfy the condition $S/N > 3$ to be classified as radio-detected. We look for radio sources in individual galaxies, but many of them have weak signatures or none at all. Therefore, we also perform the stack technique of the radio flux data, ranging in bins of σ and $M_{\rm halo}$. This technique allows us to increase the S/N of our radio data and therefore makes it possible to analyze the typical contribution of radio emission in sets of central galaxies that share similar properties.

Currently, the VLA FIRST catalog data is available through the FIRST search page[3]. We cross-match the RA and DEC positions of our sample of 14,862 central galaxies (outlined in Sect. 2.1) within a search radius of $2''$, resulting in 14,671 matched images in the VLA (not necessarily with radio emission present). Figure 2.7 shows an illustrative representation of the radio detection by the VLA FIRST of some representative galaxies of our sample. Panel 2.7a shows a case where there is no radio source detected at the galaxy position. In panels 2.7b and 2.7c respectively a weak and a strong nuclear compact source are presented, while in panel 2.7d the structure of radio jets from the supermassive black hole at the center of the galaxy is clearly seen.

[3]http://sundog.stsci.edu/cgi-bin/searchfirst

Figure 2.7 – Panel (a) illustrates a central galaxy devoided of detectable radio emission; panels (b) and (c) illustrate centrals presenting a compact nuclear radio source at two distinct brightness regimes; panel (d) depicts an extended radio source in the form of jets associated to a central galaxy.

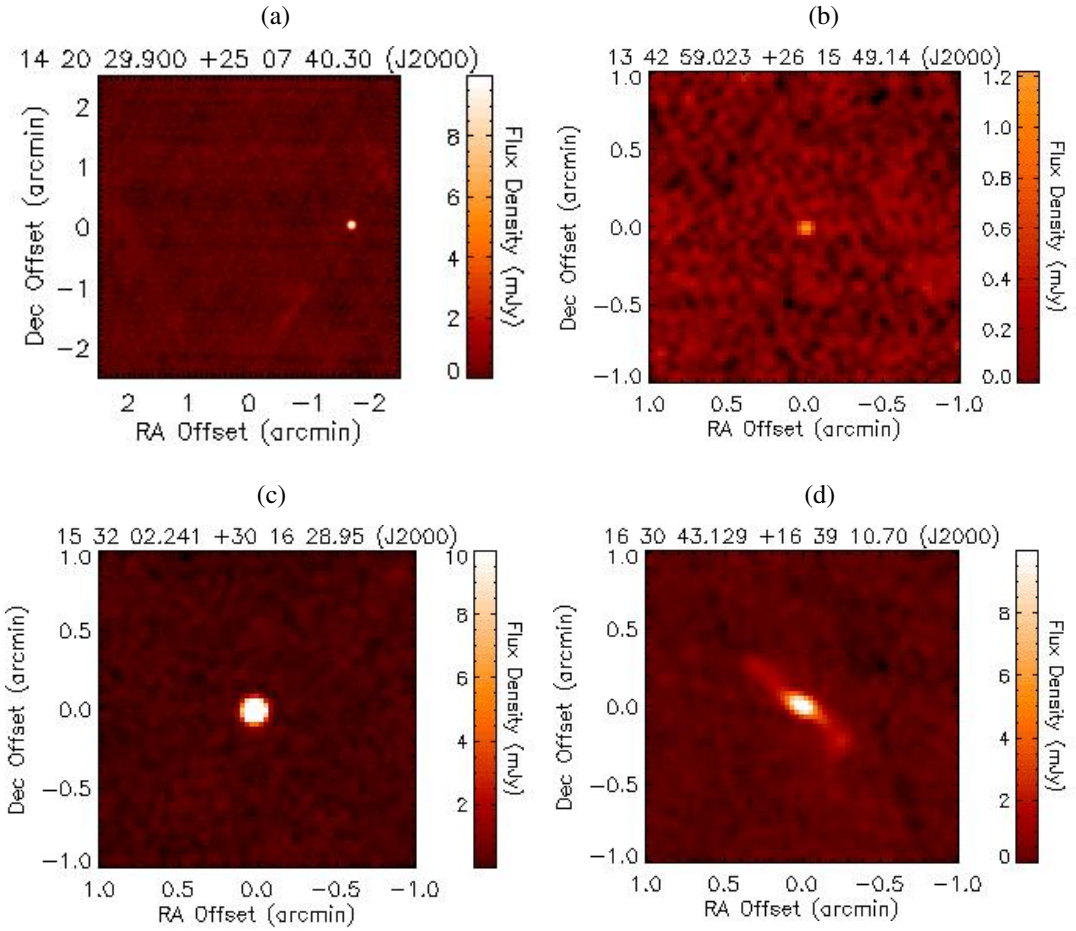

In this work, we employed two distinct methodologies to characterize the radio emission in the galaxies of our sample. The first methodology addresses a limitation of the VLA, which is not particularly deep, potentially leading to the omission of less luminous radio objects. To mitigate this issue, we enhance the S/N ratio of the radio observations by employing a stacking technique similar to what we applied to the spectra. This time, however, we stack the radio images of the galaxies. This process amplifies weaker signals, making it possible to detect radio emissions that might otherwise be missed in individual observations. The second approach involves examining each galaxy individually to identify whether it has a compact or extended radio source associated with it. This method allows us to evaluate the radio emission properties specific to each galaxy. Both methodologies are detailed below.

2.8.1 Stacking radio images by their σ and $M_{\rm halo}$

To amplify the signal from radio nuclear sources, we stacked VLA FIRST images within the same ranges of σ and $M_{\rm halo}$ as described in Sect. 2.4. This approach facilitates the comparison between optical and radio emissions. The image size was chosen to encompass an area of $5' \times 5'$, corresponding to 283×283 in pixel scale. As a result, some galaxies are not centered on the same pixel, which interferes with the calculation of median pixel values in the construction of the image stack. Therefore, we reduce the image size to 242×242 pixels, centering the central galaxies' RA and DEC at pixel coordinates 121×121.

The radio flux density $F_{\rm R}$ is calculated by summing all contributions within a 4-pixel radius from the central pixel. We estimate the $F_{\rm R}$ and the luminosity distance ($D_{\rm L}$) to calculate the radio luminosity density ($L_{\rm R}$), as this property is an intrinsic measure of the total energy emitted by the galaxy. For simplicity, we refer to the radio luminosity density ($L_{\rm R}$) as "radio luminosity" in the remainder of this work. Then, we estimate the median redshift of the galaxies in each stack and derive[4] the correspondent $D_{\rm L}$. We have then calculated the restframe 1.4 GHz radio luminosity $L_{\rm R}$ for each stack assuming that the radio continuum is well described by a power law, using $L_{\rm R}$ expressed as follows:

$$L_{\rm R} = \frac{4\pi D_L^2(z)\, S}{(1+z)^{1+\alpha}}, \tag{2.3}$$

The spectral index α is assumed to be $\alpha = -0.7$ for radio-loud galaxies at low redshift. This equation, adapted from Novak et al. (2017), presumes that radio sources exhibit a spectrum that can be characterized by a simple power law $S \propto \nu^{\alpha}$, where S denotes the monochromatic flux density. Consequently, this results in the standard radio K-correction of $K(z) = (1+z)^{-(1+\alpha)}$. The final formula for the rest-frame radio luminosity $L_{\rm R}$ is derived from the redshift z, and the luminosity distance $D_{\rm L}$.

2.8.2 Searching for radio emission in individual central galaxies

In addition to the analysis using the stacking method, we also examined the presence of radio sources in individual galaxies from our sample, thereby incorporating a study of objects with extended emission. This approach is crucial not only for confirming the galaxies already identified in the VLA FIRST as radio galaxies but also for ensuring that no potential radio galaxies, especially those with extended emissions and no central emission, are missed. These galaxies, which might display only jet signatures without central emission, are often overlooked by the VLA FIRST due to the lack of emission at the galaxy central position.

For this purpose, we apply the SExtractor software (Bertin; Arnouts, 1996) to the

[4]This was performed using the Cosmology Calculator, available in https://www.astro.ucla.edu/ wright/CosmoCalc.html.

VLA FIRST images. SExtractor automates the detection and characterization of celestial sources in digital images. Using SExtractor requires the user to specify a number of detection parameters that have to be chosen according to the nature of the imaging and the detection sensitivity desired. In our tests, we find that setting a detection threshold of 2.5 RMS and a minimum detection area of 17 square pixels above the threshold. This value for minimum detection area corresponds to the region within 2σ around the center of the PSF, which is the expected size for any unresolved source in the VLA. This approach allows SExtractor to efficiently identify evident sources while ignoring artifacts produced by the VLA image reconstruction pipeline.

We consider that a potential radio source is associated with the central galaxy whenever it is located at a maximum of 40 pixels of radius from the location of the central galaxy. This corresponds to a linear distance of ~ 140 kpc at the low redshift limit of our sample, a distance large enough to encompass virtually all extended jets (that extend up to typically 10 times the effective radius of the galaxy) while reducing the contamination by extended sources unrelated to the central. As a result, we identify radio sources associated to 1,673 central galaxies ($\sim 11\%$). We then visually inspect each image to determine whether shape, morphology and orientation of the radio source are compatible with it being originated from the central galaxy (i.e. jets pointing away from the central galaxy and/or a pair of lobes, or a central unresolved source). We have also separated the radio emission between point-like nuclear emission and extended emission; a radio source was classified as nuclear point-like if it was located at a maximum distance of 6 pixels from the central galaxy, corresponding to the 5" FWHM of the VLA FIRST PSF, while extended sources should be at least partially located at a maximum distance of 40 pixels, which corresponds to approximately 10 times the apparent extension corresponding to the typical effective radius of the galaxies in our sample, assuming $z = 0.05$.

We confirm that 508 sources (172 ICs and 336 GCs), out of those 1,673 galaxies for which a potential radio source is present, are associated with radio nuclear activity. Most of these sources have also been detected by the VLA pipeline; interestingly, our methodology resulted in 36 extra sources that were not detected by VLA. Of these 508 sources, 440 were classified as point-like, 59 as point-like plus extended sources, and 9 as extended sources with no point-like nuclear emission. Figure 2.8 presents an example of each type of radio emission in the SExtractor image output.

The first step in estimating the radio luminosity, as outlined in Equation 2.3, is to calculate the fluxes attributed to individual galaxies. In the case of extended sources, it is necessary to account for any additional fluxes identified by SExtractor that contribute to the emission. We visually inspected each output generated by SExtractor for the extended sources and subsequently calculated the total emissions by summing the contributions from each detected source clearly associated with the central galaxy radio emission. For the point-like sources, we have used the radio flux of the source closest to the central galaxy. We compare the fluxes obtained by SExtractor for the point-like sources with those from VLA FIRST and find

them to be consistent (see Figure 2.9). The left panel shows the relation between the radio flux provided by VLA FIRST and the flux estimated by SExtractor for point-like sources only, demonstrating good agreement between the two measurements, as confirmed by the Pearson coefficient (r = 0.965). The right panel displays the same relation but includes galaxies that have both point-like and extended emissions. The observed dispersion is expected since VLA FIRST does not include the flux from extended sources, only the nuclear part, in contrast to the flux measured by SExtractor, which includes these extra sources not included in the VLA FIRST.

Figure 2.8 – Examples of radio emission features from our sample, generated from the SExtractor output. From left to right: a point-like radio emission, a point-like source with extended jets, and extended jets without nuclear emission.

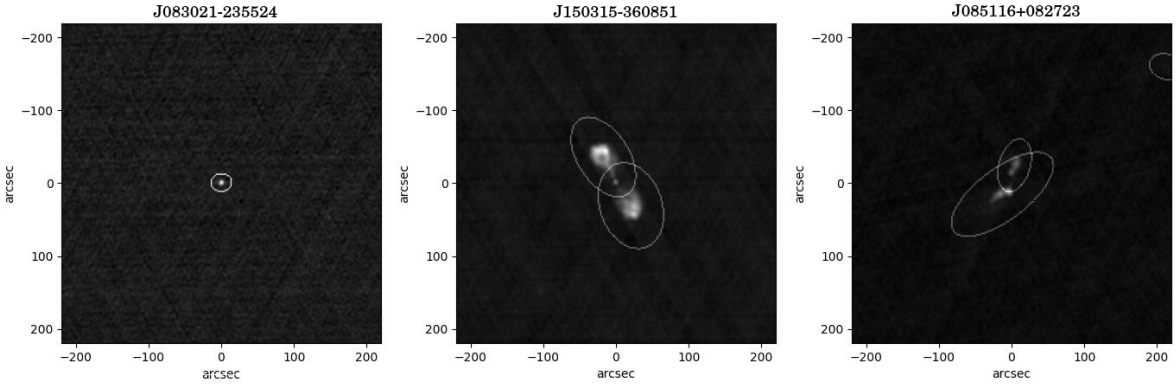

Figure 2.9 – Comparison between the flux measured by the VLA FIRST and by SExtractor, for point-like and point-like plus extended sources.

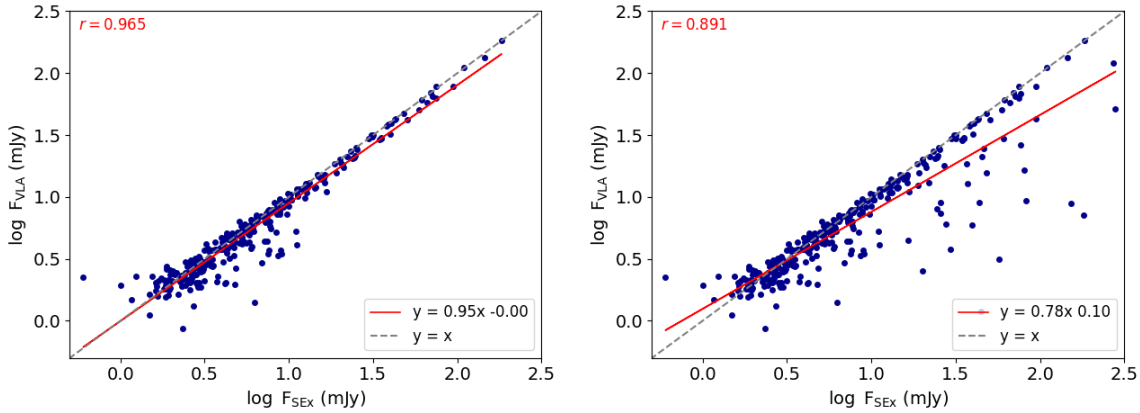

3 RESULTS

3.1 OPTICAL ANALYSIS

3.1.1 Exploring the trends in stellar population and interstellar medium properties

In this section, we present the results of the stellar population analysis of the central galaxies in our sample by means of the stacking method presented in Sect. 2.4. In Figure 3.1, we present an overview of the derived parameters (Age, Z, A_V, EWHα and [α/Fe]) as a function of the velocity dispersion σ (horizontal axis) and halo mass $M_{\rm halo}$ (vertical axis). The numerical values of the parameters for each stack are indicated by the color bars to the right of each panel; from left to right, we present the values obtained for the full sample, for ICs and GCs respectively. For most, if not all of the panels, there is a visual impression that the parameter values depend on both σ and $M_{\rm halo}$. To highlight these dependence, we present in Figure 3.2 each parameter as a function of σ for three $M_{\rm halo}$ ranges. The selected $M_{\rm halo}$ ranges are applied to coincide with both ICs and GCs. We also include the ICs trends as dotted lines in the GCs panels to facilitate the comparison.

Based on the observations from Figures 3.1 and 3.2, we will discuss the general behavior of each parameter in relation to σ and $M_{\rm halo}$. Special attention will be given to potential differences between ICs and GCs.

3.1.1.1 Stellar Age – Age

As far as ICs are concerned, we see that Age increases up to approximately $\sigma \sim 200\,{\rm km\,s^{-1}}$ and then reaches a plateau (panel b of Figure 3.2). Higher values of $M_{\rm halo}$ are associated with older stellar populations at a given σ. However, for σ values lower than $150\,{\rm km\,s^{-1}}$, the large uncertainties make it more difficult to interpret the trend. Notably, there is an age difference of approximately 2 Gyr between the low and high $M_{\rm halo}$ bins at a given σ. These trends are basically the same as those exhibited by GCs (panel c of Figure 3.2), although with a greater scatter due to the lower number of galaxies per bin. It is worth noticing that there are no GCs with $\sigma \geq 200\,{\rm km\,s^{-1}}$ in $12.0 \leq \log M_{\rm halo} \leq 12.25$. Despite these findings being consistent with those presented by (La Barbera et al., 2014), we do not observe any discernible difference between ICs and GCs, contrary to their discussion. This distinction will be further addressed in Sect. 4.

Figure 3.1 – Variations in Age, Z, A_V, EWHα and [α/Fe] as a function of σ (horizontal axis) and M_{halo} (vertical axis) are shown from the top to bottom, respectively. The parameters for the full sample, the ICs and the GCs are presented from left to right, respectively. The numerical values of the physical properties are indicated by the colorbar.

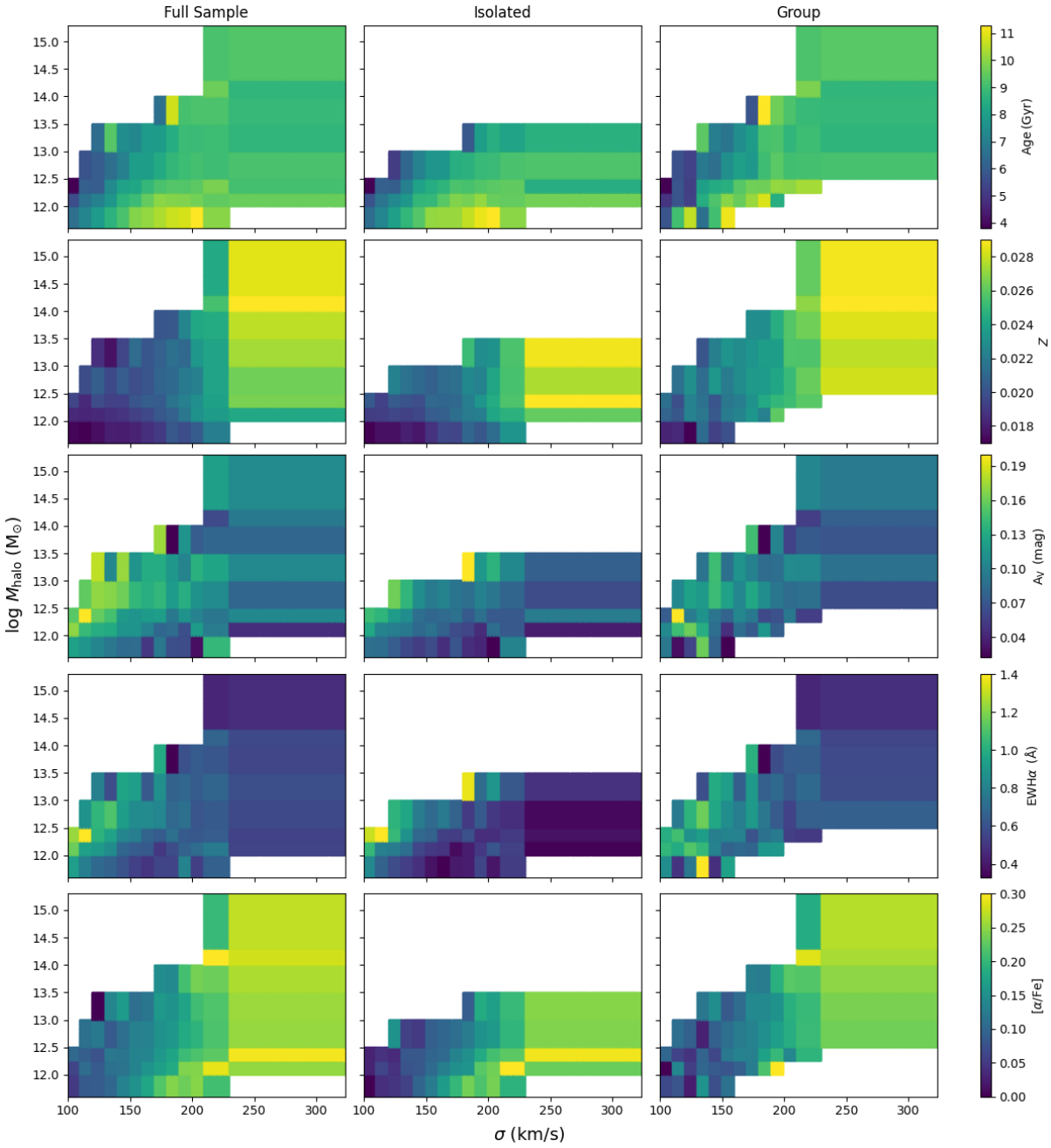

Figure 3.2 – Relation of Age, Z, A_V, EWHα and [α/Fe] with σ, depicted from top to bottom respectively, for three representative ranges of halo mass. The full sample, ICs and GCs, are presented from left to right, respectively. The M_{halo} ranges are distinguished by colors whose numerical values are indicated in panel a.

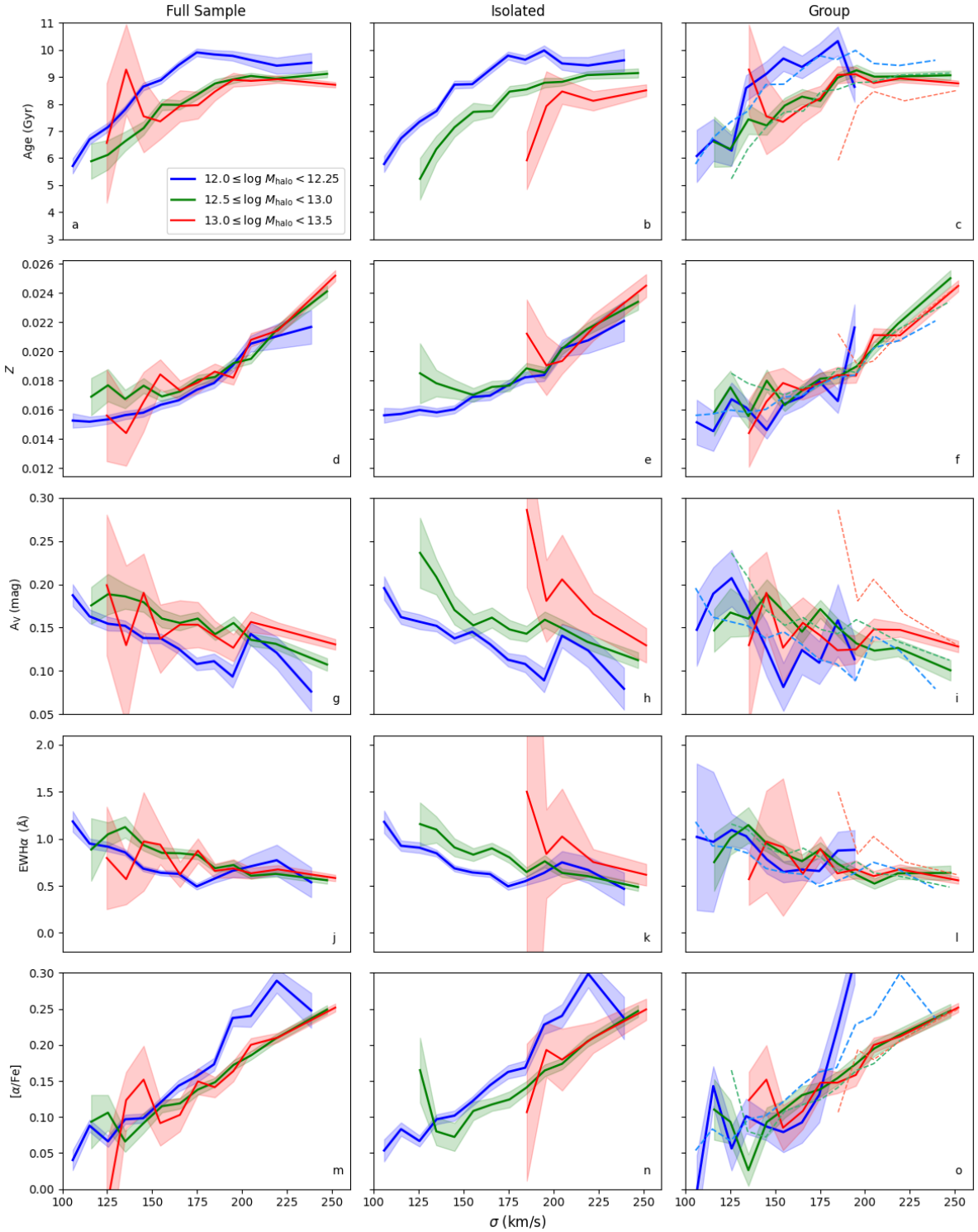

3.1.1.2 *Stellar Metallicity – Z*

Regarding the stellar metallicities, we note a tendency for the stellar population to be more metal-rich as σ increases, the so called *mass-metallicity relation* (Tremonti et al., 2004); this holds for ICs and GCs indistinctly (panels e and f of Figure 3.2). We do not find any dependence on $M_{\rm halo}$, as indicated by the overlapping curves, except for centrals with $\sigma \lesssim 150\,{\rm km\,s^{-1}}$, for which we note a slight increase in Z for the intermediate $M_{\rm halo}$ bin. This result is in agreement with those reported by La Barbera et al. (2014). There seems to be no difference between ICs and GCs as far as the behavior of Z with σ is concerned, albeit with greater scatter for GCs.

3.1.1.3 *α-enhancement – [α/Fe]*

Analyzing the [α/Fe] abundance ratios we observe a positive correlation between σ and the [α/Fe] abundance ratios, consistent across all $M_{\rm halo}$ ranges. This suggests that, generally, more massive central galaxies have experienced shorter periods of star formation compared to their less massive counterparts. This trend holds whether the galaxy is isolated or part of a group (see panels n and o from Figure 3.2). For a fixed σ value, ICs exhibit a decrease in the [α/Fe] with $M_{\rm halo}$, a trend that is visible at least within the two lower $M_{\rm halo}$ ranges. This pattern becomes less distinct at lower-σ values. For GCs, we do not observe a clear dependence with [α/Fe] with $M_{\rm halo}$ but also the uncertainty significantly increases.

3.1.1.4 *Visual Extinction – $A_{\rm V}$*

Examining panels h and i of Figure 3.2 we identify a decrease in $A_{\rm V}$ as σ increases, for ICs and GCs. Particular, for ICs we find a systematic increase in $A_{\rm V}$ as we go to centrals with $\sigma \lesssim 200\,{\rm km\,s^{-1}}$ and greater $M_{\rm halo}$. For $\sigma \gtrsim 200\,{\rm km\,s^{-1}}$ the curves overlap and $A_{\rm V}$ becomes insensitive to $M_{\rm halo}$. Conversely, there appears to be no correlation between $A_{\rm V}$ and $M_{\rm halo}$ for GCs. Nevertheless, the scatter is significantly large, making it inconclusive to assert that the same systematic difference with $M_{\rm halo}$ observed in ICs is also present in GCs.

3.1.1.5 *Equivalent width of* Hα – EWHα

In line with $A_{\rm V}$, ICs exhibit a decreasing trend in EWHα as σ increases. Notably, we observe a systematic variation with $M_{\rm halo}$, with centrals with higher EWHα inhabiting more massive halos. The difference in EWHα amounts to approximately 0.6 Å, which is significantly larger than the errors in EWHα for the two lowest $M_{\rm halo}$ bins in the plot. The relation between

EWHα and σ is less pronounced for GCs. Moreover, no apparent correlation between EWHα and $M_{\rm halo}$ is observed for GCs. The similarity in the results for $A_{\rm V}$ and EWHα holds true for both ICs and GCs, and further details will be discussed in Sect. 4.3.

3.1.2 Correlating central galaxies properties with σ and $M_{\rm halo}$

In the previous section, we detailed the behavior of the properties Age, Z, $A_{\rm V}$, EWHα and [α/Fe], in relation to σ and $M_{\rm halo}$ (illustrated in Figures 3.1 and 3.2). We conduct a quantitative analysis of these dependencies assuming a linear combination of σ and $M_{\rm halo}$ to represent the parameters:

$$Y \sim \sigma^{A} M_{\rm halo}^{B}, \tag{3.1}$$

where Y represent the variable under study, and A, B are coefficients to be determined.

The choice of a power law is motivated only by its simplicity. We apply a least squares regression to the logarithmic form of the model, $\log Y = A \log \sigma + B \log M_{\rm halo} + C$. To estimate the free parameters A, B, and C, we use the curve fit function from the SciPy Python library. This function employs non-linear least squares to fit a function to data and offers the option to include its uncertainty. In this work, the uncertainty is represented by the standard deviations of the data, estimated via bootstrap processes, as described in Section 2.5.

We incorporate uncertainties in σ and $M_{\rm halo}$ by applying the bootstrap approach, performing 1,000 iterations. The uncertainty for each σ bin ($\sigma_{\rm unc}$) is calculated via error propagation, using the mean σ and its 95th percentile error ($\sigma_{\rm err}$). Each iteration involves simulating a new σ value based on a normal distribution centered on the mean σ in each bin, with the corresponding uncertainty. To account for overlaps in $M_{\rm halo}$ due to its narrow range, we adjust each measurement by adding a random number between zero and 1.5 (the maximum absolute bias between the two methods, as derived from Fig. 2.1), allowing for both positive and negative variations. In each iteration, $M_{\rm halo}$ is recalculated by adding the product of this random number and the bias for each $M_{\rm halo}$ range, as indicated in Fig. 2.1, to the average $M_{\rm halo}$ of each bin spectrum. This method ensures a consistent directional adjustment across all $M_{\rm halo}$ ranges. Additionally, we incorporate random errors by applying a random distribution with a standard deviation equal to the galaxy-to-galaxy $\sigma_{\rm err}$ to the newly calculated $M_{\rm halo}$ value.

The coefficients A and B are determined by averaging the results from 1,000 bootstrap iterations. The uncertainties are estimated by calculating the standard deviation of the 1,000 coefficients, weighted according to their respective errors. The best-fit coefficients indicate a significant overestimation in the Age parameter at lower σ values. This overestimation is likely due to the wide range of stellar ages observed across different bootstrap realizations, possibly reflecting a larger variety in the stellar ages of galaxies in such stacks. As σ increases, this variability decreases, suggesting a more uniform age distribution in galaxies with higher

σ. To ensure our model accurately represents the observed trends, we decided to exclude Age uncertainties from our fitting process. Including these uncertainties resulted in unsatisfactory parameterization; bins with older central galaxies, which have narrower spreads, disproportionately influenced the solution, leading to less effective modeling for younger ages.

In the coefficient analysis, Age shows a weaker correlation with σ in GCs compared to ICs. The relation between Age and $M_{\rm halo}$ is notably stronger in ICs than in GCs. For Z, a more pronounced correlation with σ is observed in GCs, while its association with $M_{\rm halo}$ is more significant in ICs. However, the B coefficients for Z are quite small, suggesting a minimal dependence on $M_{\rm halo}$. The correlation of [α/Fe] with σ is consistent across all samples, with almost identical coefficients. In contrast, its relation to $M_{\rm halo}$ is weak for all sub-samples, showing a slight inverse trend, particularly in ICs, indicating that [α/Fe] tends to increase as $M_{\rm halo}$ decreases. Regarding $A_{\rm V}$, the correlation coefficients with σ are similar for both GCs and ICs, considering the uncertainties. However, the relation between $A_{\rm V}$ and $M_{\rm halo}$ is significantly stronger in ICs than in GCs, where it is very weak. For EWHα, the level of correlation with σ is comparable in both GCs and ICs, though it is marginally weaker in GCs. The correlation with $M_{\rm halo}$ is substantially lower in GCs, almost ten times less than in ICs. The correlation patterns between $A_{\rm V}$ and EWHα, as observed in Sect. 3.1.1, are also reflected in the coefficients A and B for both ICs and GCs, when taking uncertainties into account. In summary, the correlation between all properties, regardless of the sample, shows a stronger association with σ than with $M_{\rm halo}$.

To evaluate the quality of the parameterization, we introduce Figure 3.3, which shows the observed properties against the predicted values derived from Eq. 3.1 using the best-fit coefficients listed in Table 3.1. The panels of Figure 3.3 follow the same arrangement as Figure 3.2, presenting Age, Z, $A_{\rm V}$, EWHα and [α/Fe] from top to bottom, respectively. From left to right, the panels display the results for the full sample, ICs, and GCs. The solid circles represent the physical property, with their corresponding $M_{\rm halo}$ indicated by colors. We include vertical error bars, denoting the standard deviation from the bootstrap process (Sect. 2.5) and also the Pearson coefficient (r), provided as a metric for the correlation between observed and predicted values. Notice that the scatter for ICs sample is significantly smaller than for GCs. In panels b and c, a curvature in the relation, especially for ICs, suggests that our model tend to overestimate Age for $\log \mathrm{Age} < 0.8$. This curvature implies that Eq. 3.1 might not fully describe the relation among Age, σ, and $M_{\rm halo}$. Despite this curvature being a consistent feature for central galaxies across different $M_{\rm halo}$ ranges, the discrepancy between the observed and predicted values primarily arises from σ. The relation between Age and σ appears to be less steep than a simple power law suggest. However, the relatively high Pearson coefficients ($r = 0.798$, 0.872, and 0.708 for the full sample, ICs, and GCs, respectively) indicate that our parameterizations do capture most of the physical relation between Age, σ, and $M_{\rm halo}$, albeit with a note of caution in their interpretation. The parameterization for Z shows excellent performance across all sub-samples, with the scatter plot of observed versus predicted Z values closely following a 1:1

correlation, as shown by high Pearson coefficients ($r = 0.909, 0.895, 0.902$ for the full sample, ICs, and GCs, respectively). While Eq. 3.1 effectively models the relation of Z with both σ and $M_{\rm halo}$, it is important to recognize that this is largely due to the well established Mass-Metallicity relation, with $M_{\rm halo}$ contributing minimally to the overall correlation. For [α/Fe] we also have an excellent performance across all sub-samples. The full sample, displayed in panel m, shows a strong Pearson coefficient of $r = 0.913$. Similarly, ICs (panel n), exhibit a Pearson coefficient of $r = 0.918$ while GCs (panel o), although displaying a slightly lower Pearson coefficient of $r = 0.844$, still reflect a good fit to the observed data. For $A_{\rm V}$, a strong agreement between observed and predicted values is seen for ICs, as indicated by the Pearson coefficient of $r = 0.822$ (panel h). However, a lower Pearson coefficient of 0.287 for GCs (panel i) suggests a limitation of our model in accurately describe the relation between $A_{\rm V}$, σ, and $M_{\rm halo}$. In the case of EWHα, a satisfactory agreement between observed and predicted values is found for ICs, evidenced by a higher Pearson coefficient of $r = 0.839$ (panel k). The scatter in GCs is more pronounced, resulting in a lower Pearson coefficient of 0.572 (panel l). Despite the greater variance in GCs, the parameterization is a reasonable representation for both $A_{\rm V}$ and EWHα. In a nutshell, the main outcomes from the parameterization shown in Table 3.1 reveal that σ is more important in determining the observed properties of central galaxies than $M_{\rm halo}$. The impact of $M_{\rm halo}$ on these properties is typically small, particularly for GCs. ICs, on the other hand, show stronger correlations with most parameters in relation to both σ and $M_{\rm halo}$. An exception is observed in the correlation between Z and σ, which is more pronounced in GCs. This indicates that for ICs, it is easier to predict how these properties behave in relation to σ and $M_{\rm halo}$. The implications of these findings will be addressed in the following section.

Table 3.1 – Correlation coefficients A, B and C (column 1) obtained from Equation 3.1, for each sub-sample (column 2), between Age (column 3), Z (column 4), $A_{\rm V}$ (column 5), EWHα (column 6) and [α/Fe] (column 7), versus $\log\sigma$ and $\log M_{\rm halo}$. The errors are quoted at the 1σ level.

Coefficient	Environment	Age	Z	$A_{\rm V}$	EWHα	[α/Fe]
	Full Sample	0.62 ± 0.03	0.58 ± 0.04	-0.54 ± 0.15	-0.91 ± 0.18	0.69 ± 0.03
A	Isolated	0.70 ± 0.05	0.49 ± 0.04	-0.62 ± 0.12	-1.14 ± 0.15	0.64 ± 0.03
	Group	0.53 ± 0.05	0.75 ± 0.01	-0.55 ± 0.05	-0.82 ± 0.03	0.64 ± 0.01
	Full Sample	-0.03 ± 0.01	0.03 ± 0.01	0.07 ± 0.02	0.09 ± 0.03	-0.013 ± 0.003
B	Isolated	-0.08 ± 0.04	0.03 ± 0.02	0.13 ± 0.07	0.16 ± 0.08	-0.03 ± 0.02
	Group	-0.03 ± 0.01	0.012 ± 0.004	0.02 ± 0.01	0.011 ± 0.007	0.002 ± 0.004
	Full Sample	-0.03 ± 0.13	-3.35 ± 0.14	-0.34 ± 0.33	0.95 ± 0.45	-1.25 ± 0.06
C	Isolated	0.38 ± 0.55	-3.21 ± 0.24	-1.00 ± 0.82	0.56 ± 0.98	-0.96 ± 0.19
	Group	0.15 ± 0.14	-3.59 ± 0.07	0.27 ± 0.09	1.60 ± 0.08	-1.32 ± 0.04

Figure 3.3 – Comparison between observed properties and their corresponding predicted values obtained from Equation 3.1. The full sample, as well as ICs and GCs, are illustrated from left to right, respectively. Central galaxies are represented by dots, with their corresponding $M_{\rm halo}$ ranges indicated by colors. Vertical error bars are derived from the bootstrap process detailed in Sect. 2.5 and 2.6. Additionally, the degree of correlation between the observed and predicted values, estimated by the Pearson coefficient (r), is shown in all panels.

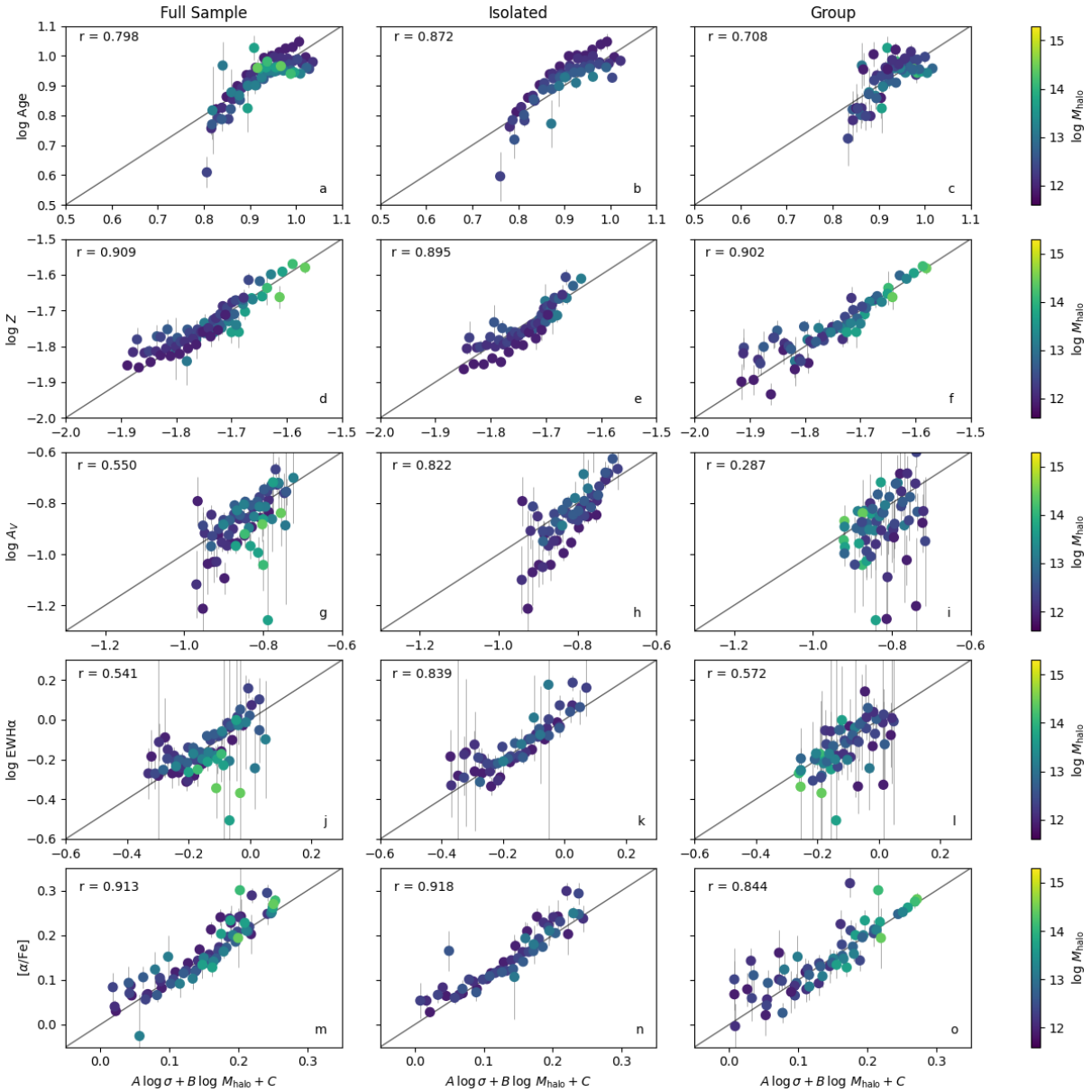

3.1.3 Exploring the trends in stellar population and interstellar medium properties for individual central galaxies

In this section, we present the results of the stellar population and ionized gas of the central galaxies in our sample by examining the individual behavior of these objects. We apply the STARLIGHT code to each galaxy and extract the stellar age, Z, A_V. Also, we measure the EWHα and the emission lines fluxes via Gaussian fits, following the same steps described in Sect. 2.5 and 2.7, with the difference that now we are doing these processes for each galaxy individually. In Figure 3.4 and 3.5, we present an overview of the derived parameters as a function of σ (horizontal axis) and $M_{\rm halo}$ (vertical axis), for ICs and GCs, respectively. Each colored square represents the average value of the property distributed across 14 bins of σ and 14 bins of $M_{\rm halo}$. The figures for ICs and GCs are identically structured, with the upper left, upper right, bottom left, and bottom right panels focusing on stellar Age, Z, A_V, EWHα and [α/Fe], respectively.

3.1.3.1 Characterizing trends in stellar populations and gas properties

As far as ICs are concerned (Fig. 3.4), we observe an old stellar population in direction of higher σ and lower $M_{\rm halo}$ values. Regarding the stellar metallicities, an increase in Z with both σ and $M_{\rm halo}$ is observed. Both panels displaying A_V and EWHα, exhibit a decrease with higher σ and lower $M_{\rm halo}$. The analysis of the plots for GCs (3.5) reveals trends similar to those found for ICs. However, for A_V and EWHα the trends for GCs are less clear and more challenging to discern compared to when we employ the stacking methodology.

The plots come with the challenge of using spectra that are noisier for each galaxy. Yet, they also provide an advantage. By mapping each galaxy individually,we produce a more a smoother variation map of these parameters across σ and $M_{\rm halo}$, which makes it easier to discern the trends of the properties with σ and $M_{\rm halo}$. It is noteworthy that these observations are in line with previous results obtained using the stacking methodology, increasing our confidence that these trends are heading in the right direction.

Figure 3.4 – Properties of central galaxies, including stellar Age (upper left panel), metallicity Z (upper right panel), extinction A_V, and equivalent width of Hα EWHα (bottom left and right panels, respectively), are shown as functions of σ and $M_{\rm halo}$ for ICs.

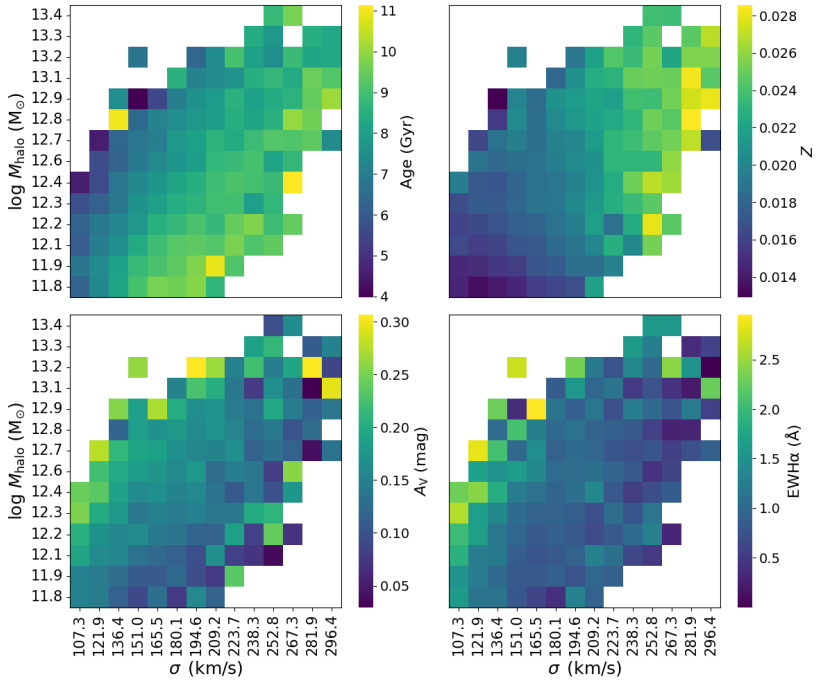

Figure 3.5 – Properties of central galaxies, including stellar Age (upper left panel), metallicity Z (upper right panel), extinction A_V, and equivalent width of Hα EWHα (bottom left and right panels, respectively), are shown as functions of σ and $M_{\rm halo}$ for GCs.

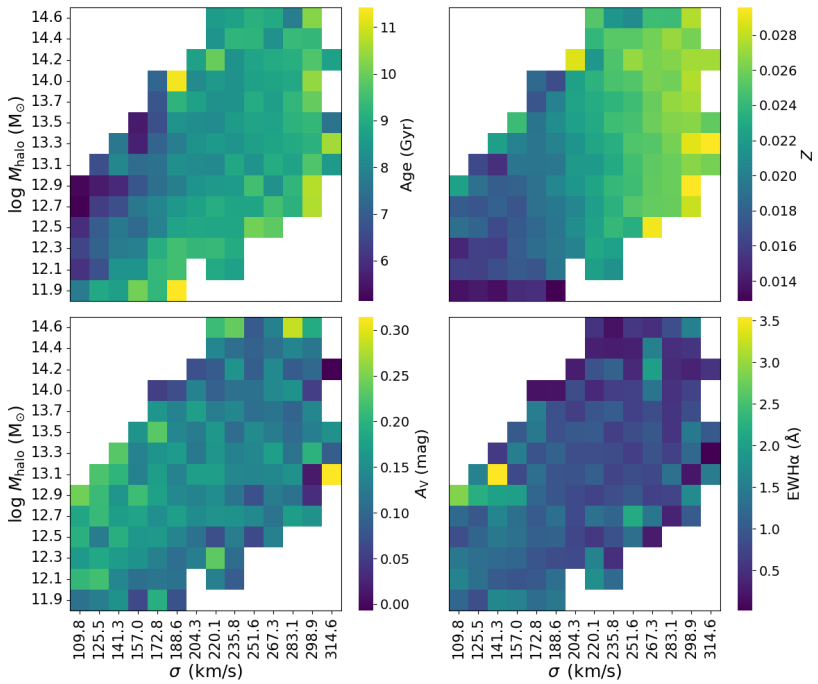

3.1.3.2 Ionization sources: Insights from BPT and WHAN diagrams

In order to investigate the nature of the ionizing agent of the gas observed in our sample of central galaxies, we have measured the fluxes and equivalent widths of the Hβ, [OIII]λ5007, [NII]λ6584 and Hα emission lines for full sample. Using these data, we derive the diagnostic diagrams BPT and WHAN, presented in figures 3.6a and 3.6b respectively. Inspection of the BPT diagram indicates that most galaxies fall in the LINER region; however, as we know that the BPT diagram is unable to distinguish LINERs from fake AGN (i.e. RGs). The composite region (SF+AGN) ranks second in number of galaxies. By analyzing the WHAN diagram, we confirm that most galaxies in our sample are indeed retired galaxies, i.e, galaxies whose gas is ionized by HOLMES. We used the conditions imposed to construct the WHAN diagram to separate our sub-sample in Seyferts, Star Forming, LINERs, Retired and Passive objects in order to investigate the occurrence of these ionization sources in different environments and across different σ ranges.

After separating the galaxies using the WHAN diagram, we obtained 24 star forming, 238 strong AGN, 495 LINERs, 8074 retired and 5445 passive central galaxies, corresponding to 0.17, 1.7, 3.5, 57 and 38% of the sample, respectively. We present the distributions of centrals for the full sample for each ionization source (except the star forming class, due to the very low number of galaxies in this class) in the space $M_{\rm halo}$ *vs.* σ in Figure 3.7. The panels RG, PG, LIN, and SEY depict the distributions corresponding to retired galaxies, passive galaxies, LINERs, and Seyferts, respectively. In the first column (η), all plots are identical, and the color of each hexagon represents the number of central galaxies in different regions of the plane σ-$M_{\rm halo}$, normalized to the largest value (notice that the maximum value indicated in the colorbar is 1.0). In the second column (η_{opt}), the plots are similar to the first column, except that we separate the counts of galaxies in each ionization class separately (RG, PG, LIN, SEY from top to bottom). The third column presents the ratios ρ between the number of galaxies N_i in the i-th ionization class (RG, PG, LIN, SEY) in a given hexagon and the total number of galaxies N in the same hexagon, i.e.

$$\rho_i = \frac{N_i}{N}. \tag{3.2}$$

Just as in the first column, we normalize the colormap to the largest value of ρ_i. The fourth column, $\rho_{\sigma_{err}<0.2}$, replicates the information from third column panels but is limited to hexagons where the error propagation is less than 0.2, thereby ensuring a higher level of measurement precision. Normalizing the number of galaxies from a specific class to the total number in each hexagon helps reduce any interpretative bias arising from the larger number of galaxies present in certain areas.

Analyzing of Figure 3.7, it becomes evident that RGs and PGs dominate our sample. This predominance is why their distribution more closely resembles the total galaxy distribution in the σ-$M_{\rm halo}$ space. However, there is a distinct upward trend in $\rho_{\sigma_{err}<0.2}$ with σ at a fixed $M_{\rm halo}$. This implies that, for a given $M_{\rm halo}$, a galaxy with a lower σ is more likely to be a RG

than one with a higher σ. In contrast, PG display the opposite behavior, becoming relatively less common at lower σ values in a fixed $M_{\rm halo}$. This trend is probably linked to the fact that PGs are found in a region with lower EWHα in the WHAN diagram, and as observed in the previous section, EWHα decreases with σ for a fixed $M_{\rm halo}$. LINERs appear to exhibit a similar pattern to RGs while SEY appear to be more uniformly distributed across the ranges of σ and $M_{\rm halo}$, showing no clear correlation with these parameters. Given the limited number of Seyfert galaxies in the sample, the statistical analysis is constrained, and thus any conclusions drawn should be considered with caution.

Figure 3.6 – BPT (left panel) and WHAN (right panel) diagrams for full sample.

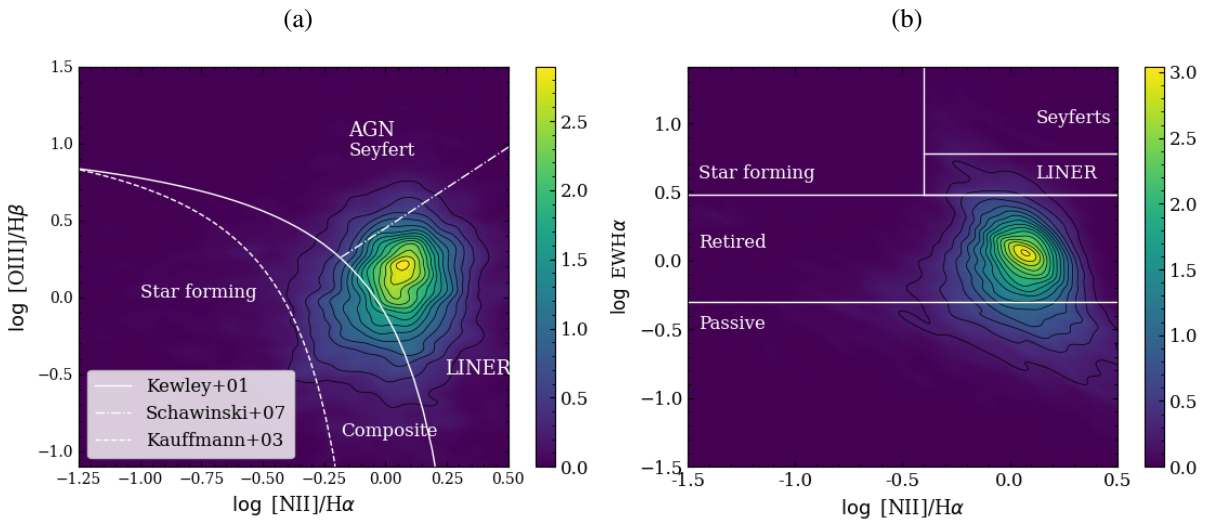

Figure 3.7 – Distributions of centrals for the full sample for each ionization source in the space $M_{\rm halo}$ *vs.* σ. The panels RG, PG, LIN, and SEY depict the distributions corresponding to retired galaxies, passive galaxies, LINERs, and Seyferts, respectively. The columns η and η_{opt} show the distributions of all central galaxies and those with the respective ionization sources in our sample, respectively. In panel ρ, each hexagon indicates the ratio of the number of galaxies with a determined ionization source to the total number of galaxies. The panel $\rho_{\sigma_{err}<0.2}$ replicates the information from Panel ρ but is limited to hexagons where the error propagation is less than 0.2.

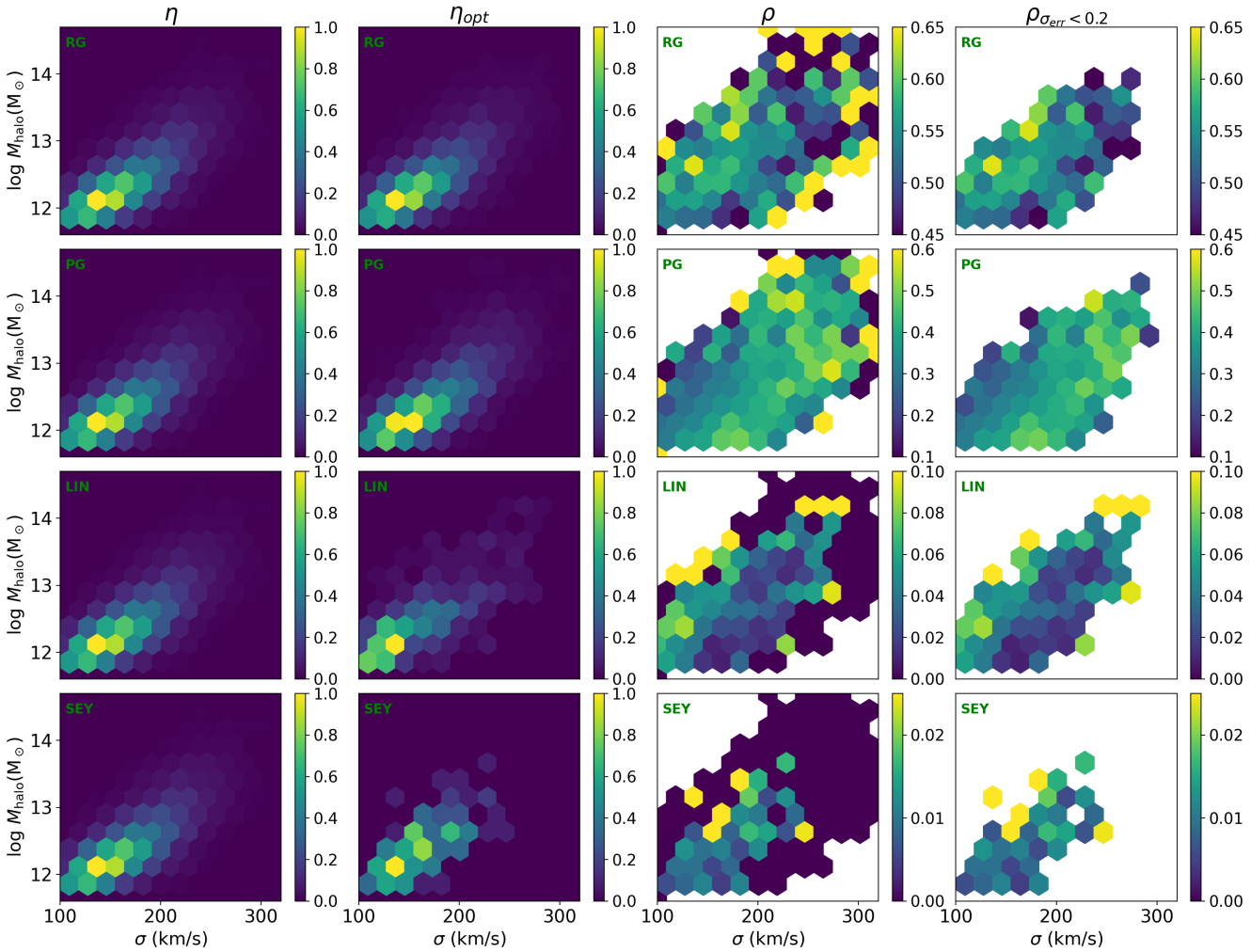

3.2.1 Investigating the trends of stacked radio data with σ and $M_{\rm halo}$

We now present the results of the analysis of the 1.4 GHz radio emission from the central galaxies in our sample using the methodology of radio image stacking presented in Sect. 2.8.1. Figure 3.8 presents the radio luminosity density $L_{\rm R}$ for each stack as a function of σ and $M_{\rm halo}$ using the same layout of Figure 3.1. The left panel illustrates the behavior of $L_{\rm R}$ in relation to σ and $M_{\rm halo}$ for the full sample, while the middle and right panels present the same relation for ICs and GCs, respectively. Analyzing the full sample panel, we observe an increase in $L_{\rm R}$ with both σ and $M_{\rm halo}$. For both ICs and GCs, the trend is less clear, but there still appears to be an increase in $L_{\rm R}$ with σ and $M_{\rm halo}$. Although the graphs are challenging to interpret visually, it is apparent that $L_{\rm R}$ is not independent of these parameters. Additionally, the dependencies of $L_{\rm R}$ on σ and $M_{\rm halo}$ do not seem to vary significantly between ICs and GCs, within the limits of $M_{\rm halo}$ that we can compare them.

To facilitate the interpretation of the results obtained in Figure 3.8, we have plotted the relation between $L_{\rm R}$ and σ for three representative ranges of $M_{\rm halo}$, as was done in Figure 3.2 for the stellar population parameters (Figure 3.9). We confirm the increasing trend of $L_{\rm R}$ with σ across all sub-samples. Additionally, we observe a rising trend of this property with $M_{\rm halo}$ for ICs. For GCs, the highest and the lowest $M_{\rm halo}$ range seem to follow the same trend, while the intermediate $M_{\rm halo}$ range falls below. Furthermore, in the lower $M_{\rm halo}$ range, with a fixed σ, GCs tend to exhibit higher $L_{\rm R}$ values compared to ICs.

Inspired by the parameterization conducted in Sect. 3.1.2, and considering that $L_{\rm R}$ evidently depends on both σ and $M_{\rm halo}$, we apply the same parameterization to $L_{\rm R}$ in terms of σ and $M_{\rm halo}$ that was used previously. The best-fit coefficients, presented in Table 3.2, support the trends shown in Figure 3.8. We measure the coefficients A, B, and C for $L_{\rm R}$ in each sub-sample using the CURVE_FIT function from the SciPy Python library. Uncertainties in σ and $M_{\rm halo}$ are accounted for by following the same steps described in Section 3.1.2. The coefficients A and B are determined by averaging the results from 1,000 bootstrap iterations while their uncertainties are estimated by calculating the standard deviation of these 1,000 realizations. The uncertainties in the correlation between $L_{\rm R}$ with σ and $M_{\rm halo}$ tend to be overestimated, as the fitting process assigns equal weight to all stacked images.

The A coefficient indicates a strong positive correlation between $L_{\rm R}$ and σ, with ICs and GCs showing the same correlation within the uncertainties. However, it is important to take these results with a grain of salt due to the higher uncertainties in both coefficients. The correlation between $L_{\rm R}$ and $M_{\rm halo}$ (coefficient B) is non-null and positive for all sub-samples. Notably, B is considerably smaller for GCs, clearly beyond the uncertainties, which likely results from the lack of a straight correlation with $M_{\rm halo}$ observed in Figure 3.9.

Figure 3.8 – Variations in radio luminosity ($L_{\rm R}$), represented by color as a function of velocity dispersion σ (horizontal axis) and halo mass $M_{\rm halo}$ (vertical axis). The full sample, as well as ICs and GCs, are illustrated from left to right, respectively.

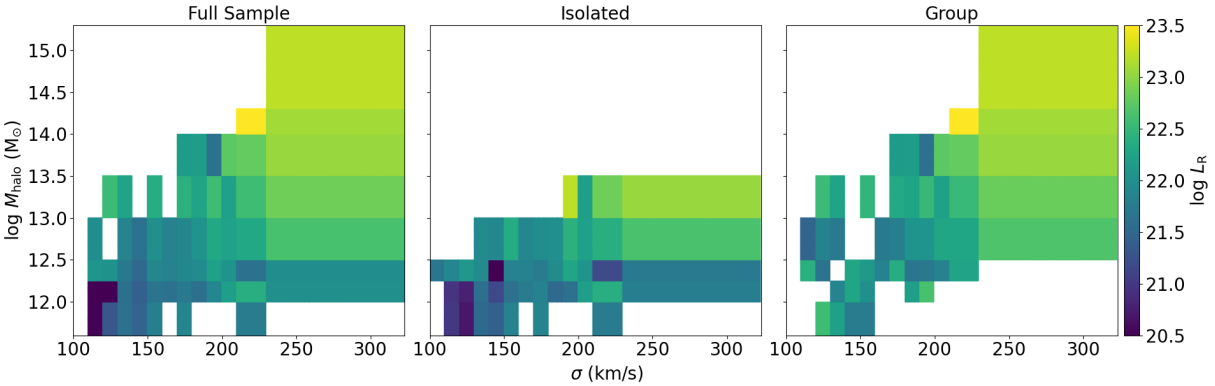

Figure 3.9 – Relation between radio luminosity ($L_{\rm R}$) and velocity dispersion (σ). The full sample, followed by ICs and GCs, are presented from left to right, respectively. We included three halo mass ($M_{\rm halo}$) ranges, distinguished by colors.

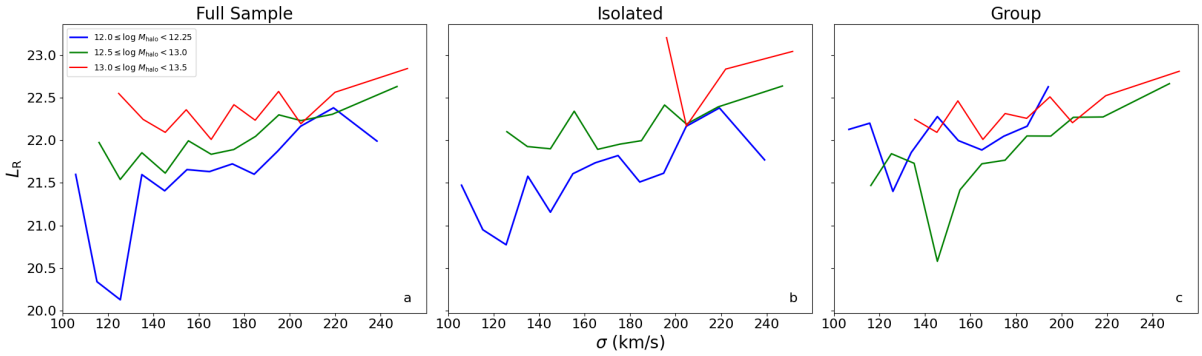

Table 3.2 – Correlation coefficients A, B and C (column 1) obtained from Equation 3.1, for each sub-sample (column 2), between radio luminosity $L_{\rm R}$ (column 3) versus $\log\sigma$ and $\log M_{\rm halo}$. The errors are quoted at the 1σ level.

Coefficient	Environment	$L_{\rm R}$
	Full Sample	3.12 ± 0.61
A	Isolated	1.80 ± 0.57
	Group	2.30 ± 1.11
	Full Sample	0.45 ± 0.10
B	Isolated	1.03 ± 0.17
	Group	0.37 ± 0.18
	Full Sample	9.64 ± 1.37
C	Isolated	5.53 ± 2.04
	Group	12.54 ± 1.97

3.2.2 Analyzing trends in radio-emitting central galaxies

As previously mentioned (Sect. 2.8.2), the individual radio sample analysis identify emission in 508 central galaxies. Distribution of radio sources relative to the full sample, ICs and GCs, from left to right, respectively. First row panels displays all central galaxies (η) in each sub-sample, while second row panels focus on those galaxies with radio emission (η_R). Third row panels illustrates the ratio between the number of galaxies with radio emission and the total number of galaxies in that hexagon (ρ). Fourth row panels ($\rho_{\sigma_{err}<0.2}$) replicate third row panels but consider only data where the error in the ratio ρ is less than 20%. All panels represent these properties as a function of velocity dispersion (σ) and halo mass ($M_{\rm halo}$). The second and third columns replicate the structure of the full sample column but are specific to ICs and GCs, respectively. These plots suggest that radio emissions are predominantly found at higher values of σ and $M_{\rm halo}$, with a more frequent occurrence in group environments.

To ensure that our results for $L_{\rm R}$ are not biased by redshift and consequently to eliminate potential selection bias in the radio data, we present Figure 3.11. This figure sets a limit, marked by the red line, based on the luminosity $L_{\rm R}$ that a source would have within our sample redshift range with a flux at the VLA FIRST survey detection threshold of 1 mJy. In subsequent analyses, only galaxies above the horizontal dashed line, at $\log L_{\rm R} \sim 22.55$, are considered. This approach ensures we are working with an unbiased sample in terms of z.

Figure 3.10 – Fraction of the number of radio sources detected relative to redshift z.

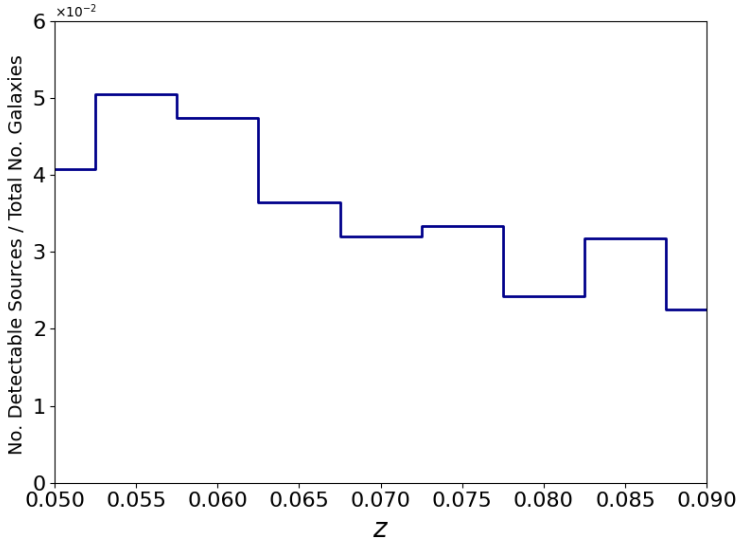

Figure 3.11 – Relation between radio luminosity (L_R) and redshift (z). The horizontal line indicates the completeness limit of the radio sample, established by the green line, which corresponds to the L_R of a source whose flux is defined by the detection threshold of the VLA FIRST (1 mJy).

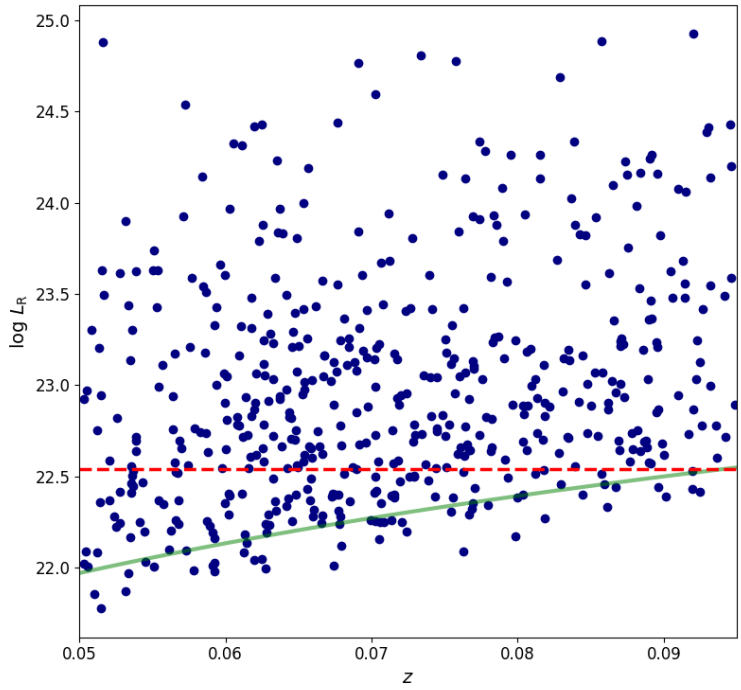

Figure 3.13 illustrates the relation between L_R and σ in the left panel, and M_{halo} in the right panel, for the full sample, ICs, and GCs, from top to bottom, respectively. In the full sample left panel, a plateau is evident up to around $\sigma \sim 230\,km/s$. Beyond this value, L_R seems to increase with σ, with a vertical rise observed at approximately $250\,km/s$. A similar pattern emerges in the right panel for M_{halo}, where L_R shows a gradual increase, followed by

a noticeable vertical increase around $\log M_{\rm halo} \sim 13.5$. In the ICs left panel, there appears to be a subtle decrease trend between $L_{\rm R}$ and σ up to $\sigma \sim 175\,{\rm km/s}$. Beyond this value, the trend transitions to a plateau, indicating no significant correlation. Contrary to what is observed in the $L_{\rm R}$ *vs*. $M_{\rm halo}$ panel for the full sample, the right panel for ICs reveals a decrease in $L_{\rm R}$ with increasing $M_{\rm halo}$. However, due to the low number of ICs with radio emission, caution is advised in interpreting these results. Additionally, we have estimated the p-value for the relations involving ICs and found that the correlation is not statistically significant. For GCs, both σ and $M_{\rm halo}$ appear to have a slight increase relation with $L_{\rm R}$. It is noteworthy that the GCs are the key contributors to the feature observed in the full sample, characterized by a vertical increase in $L_{\rm R}$ with both σ and $M_{\rm halo}$. In contrast, ICs contribute to the plateau observed below $\sigma \approx 230\,{\rm km/s}$.

Figure 3.12 – Distribution of radio sources relative to the full sample, ICs and GCs, from left to right, respectively. First row panels displays all central galaxies (η) in each sub-sample, while second row panels focus on those galaxies with radio emission (η_R). Third row panels illustrates the ratio between the number of galaxies with radio emission and the total number of galaxies in that hexagon (ρ). Fourth panels ($\rho_{\sigma_{err}<0.2}$) replicates third row panels but considers only data where the error propagation in the ratio is less than 0.2. All panels represent these properties as a function of velocity dispersion (σ) and halo mass ($M_{\rm halo}$).

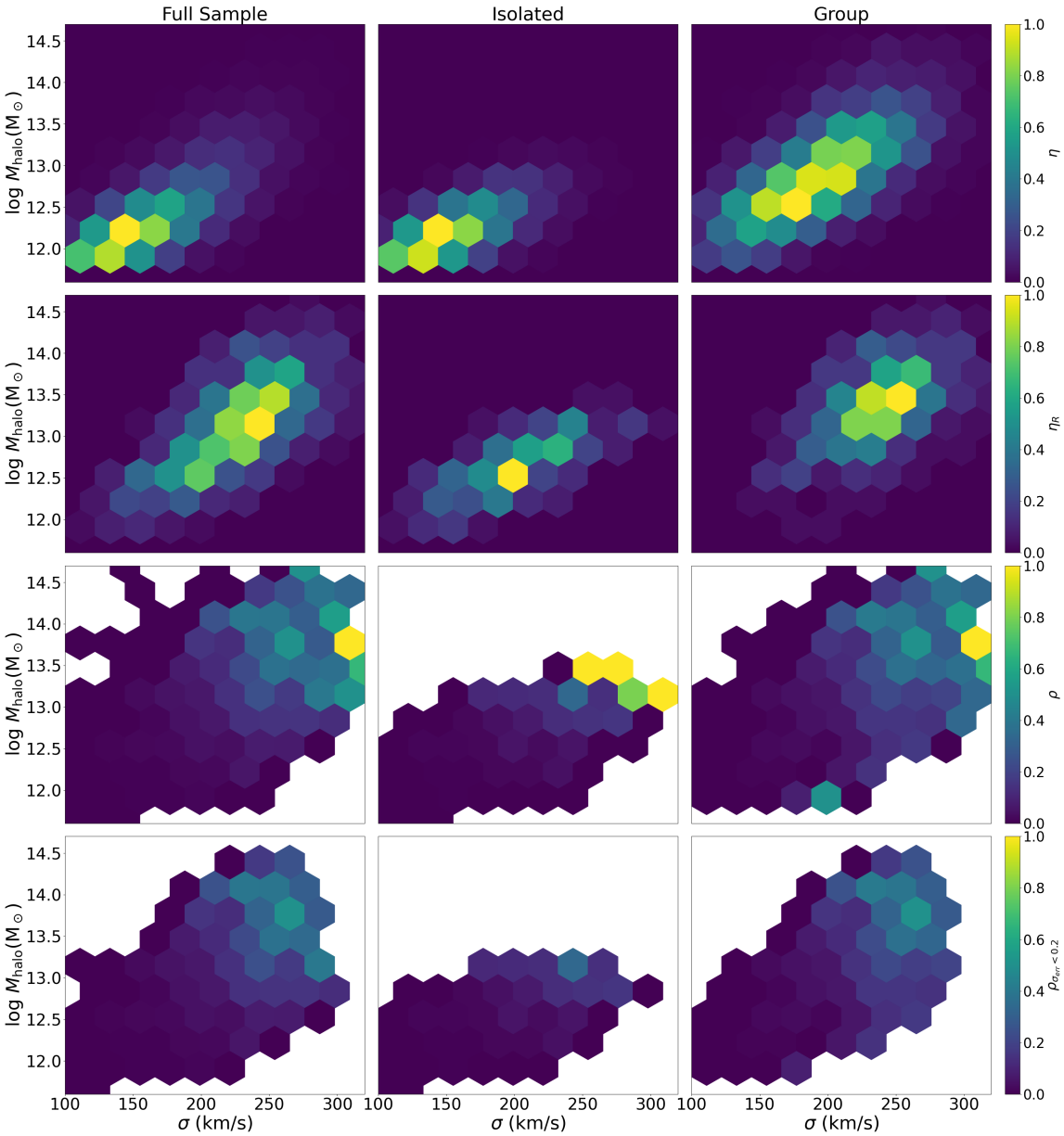

Figure 3.13 – Relation between radio luminosity ($L_{\rm R}$) and velocity dispersion (σ) and halo mass ($M_{\rm halo}$), from left to right, respectively.

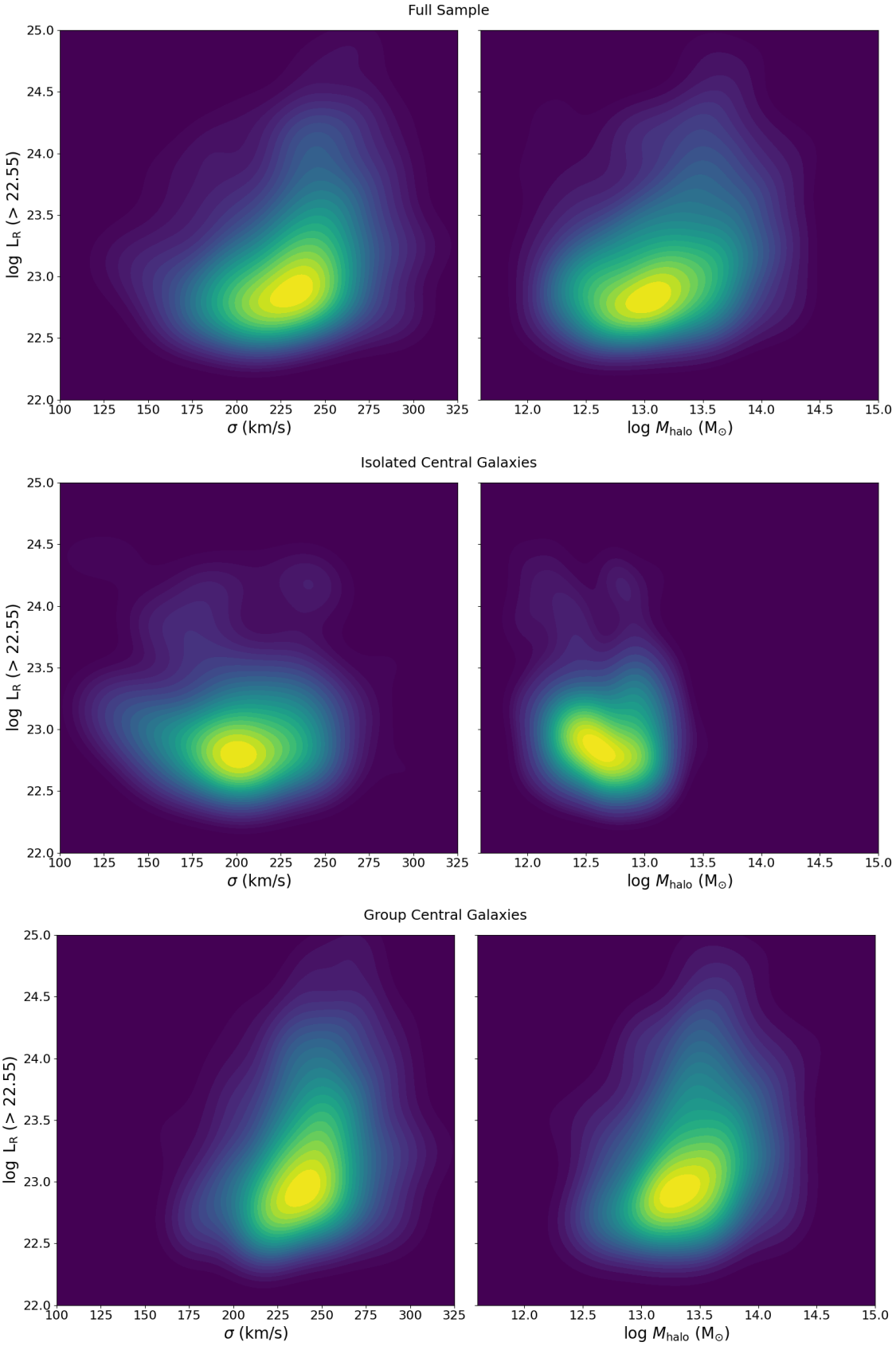

4 DISCUSSION

The evolution of central galaxies remains a challenging puzzle to solve. Both the $M_{\rm halo}$ in which these galaxies are located and their σ, are critical in determining their development. Research conducted by La Barbera et al. (2014) on early-type central galaxies has shown that an increase in σ corresponds with an older stellar population. Additionally, it has been noted that, for a constant σ, galaxies in more massive halos are generally younger. Further complicating this scenario is the dynamic interaction between the thermal energy of the ICM and the kinetic energy of AGN, which adds layers of complexity to an already intricate subject.

4.1 THE IMPACT OF THE ENVIRONMENT ON THE STAR FORMATION HISTORY OF CENTRAL GALAXIES

Analyzing the influence of the environment on galaxy attributes, to define "environment" is pivotal. La Barbera et al. (2014) utilize $M_{\rm halo}$ as an environmental indicator, categorizing a central galaxy as isolated if $\log M_{\rm halo} \leq 12.5$. But, an analysis using Yang structure classification alongside the definition by La Barbera et al. (2014) of isolated centrals (ICs) reveals overlap between ICs and group centrals (GCs). Specifically, around 15% of ICs (~ 2011 galaxies) have $\log M_{\rm halo} \geq 12.5$, and about 24% of GCs ($\sim 889$ galaxies) are under the 12.5 threshold. In this study, we employ the Yang classification to investigate discrepancies in stellar populations between ICs and GCs, while La Barbera et al. (2014) suggest that the difference primarily arises from defining ICs as centrals with lower halo mass. However, considering the contamination mentioned earlier, this assertion appears questionable.

We notice that trends in σ and $M_{\rm halo}$ are consistently similar for both ICs and GCs. This suggests a unified process for star formation history (SFH) in central galaxies, irrespective of whether they are replenishing gas from their halo (like ICs) or accreting gas-rich systems (as GCs). The trend between Age and σ is observed for galaxies in general, corroborating findings from González Delgado et al. (2015). Concerning Z, our observations, especially in panels e and f of Figure 3.2, align with La Barbera et al. (2014). We notice an increase in Z with σ, following the Mass-Metallicity relation initially established by Lequeux et al. (1979). Moreover, in agreement with La Barbera et al. (2014), we do not observe significant dependency on $M_{\rm halo}$, except for a marginal variance between ICs and GCs when $\sigma \leq 135\,{\rm km\,s^{-1}}$, with ICs being slightly more metal-rich than their counterparts in GCs.

The relation between Age, Z, and $M_{\rm halo}$ has been a topic of debate in the literature. A study by Oyarzún et al. (2022) on passive centrals from the MaNGA survey (Bundy et al., 2015) finds these galaxies to be older and more metal-poor in more massive halos, contrasting our observations. The discrepancy between their findings and ours could stem from their choice

of passive galaxies based on spatially integrated specific star formation rates, irrespective of morphology. Scholz-Díaz, Martín-Navarro & Falcón-Barroso (2022) observed more metal-poor central galaxies in massive halos at fixed σ. This difference may arise because our sample of central galaxies consists exclusively of ETGs, while the authors include both early- and late-type galaxies in their analysis.

The age of a galaxy reflects its entire SFH. However, numerical values of age alone cannot differentiate between an extended, continuous SFH and an old population followed by a quiescent phase with a recent burst. To address this, we present Figure 4.1, illustrating the cumulative SFH (for full sample) across different σ and $M_{\rm halo}$ bins. Each panel shows the cumulative mass fraction of each SSP as a function of look-back time (in Gyr). For a given σ, SFHs tend to be more extended with increasing $M_{\rm halo}$. Similarly, at a fixed $M_{\rm halo}$, galaxies with lower σ display more extended SFHs. Therefore, lower σ and $M_{\rm halo}$ values (bottom-left of Figure 4.1) correspond to more extended SFHs while the opposite holds true for the upper right part of the figure. This aligns with De Lucia et al. (2006) study, which combines N-body simulations with semi-analytic techniques to investigate the formation and evolution of elliptical galaxies in a hierarchical merger model. They find that lower-mass elliptical galaxies exhibit extended star formation time-scales.

Analyzing the [α/Fe] ratio as a function of σ and $M_{\rm halo}$ in Sect. 3.1.1.3, we observe an increase of the abundance of α elements relative to Fe as σ increases. This indicates that the more massive galaxies in our sample have shorter star formation time-scales compared to less massive ones, in agreement with what we find measuring the SFH as in Figure 4.1. This pattern seems to be independent of the environment. In terms of GCs, the [α/Fe] ratio does not appear to be influenced by their $M_{\rm halo}$. On the other hand, ICs, at a fixed sigma, show a decreasing relationship with $M_{\rm halo}$, particularly for the lowest halo mass bin, indicating more prolonged star formation in this regime. This trend is reflected in the B coefficient for the full sample in Table 3.1, where a non-zero value for the coefficient B is observed. However, when analyzing the B coefficients in this table for both ICs and GCs, it is evident that the dependency on $M_{\rm halo}$ diminishes to a null value within 2σ. This might explain why in La Barbera et al. (2014), the authors find a trend of higher [α/Fe] for less massive halos (which they called "isolated galaxies"). This shift to lower halo masses in their analysis might be influenced by the lower mass halos within the ICs, since they group all galaxies together. However, when we specifically look at the ICs as a whole and their relation with $M_{\rm halo}$, the dependency seems almost non-existent.

We would expect to see a decrease in [α/Fe] with increasing $M_{\rm halo}$, however, this trend is not observed. When we segment the data by $M_{\rm halo}$ and take the environment into account, it becomes more difficult to discern clear patterns as the parameter becomes noisier. Nonetheless, in the lower $M_{\rm halo}$ regime for ICs, there is an observed excess of α/Fe, which is in line with the findings reported in La Barbera et al. (2014). However, since the difference they find is small, about 0.1 dex, discerning variations across different $M_{\rm halo}$ ranges and comparing ICs and GCs

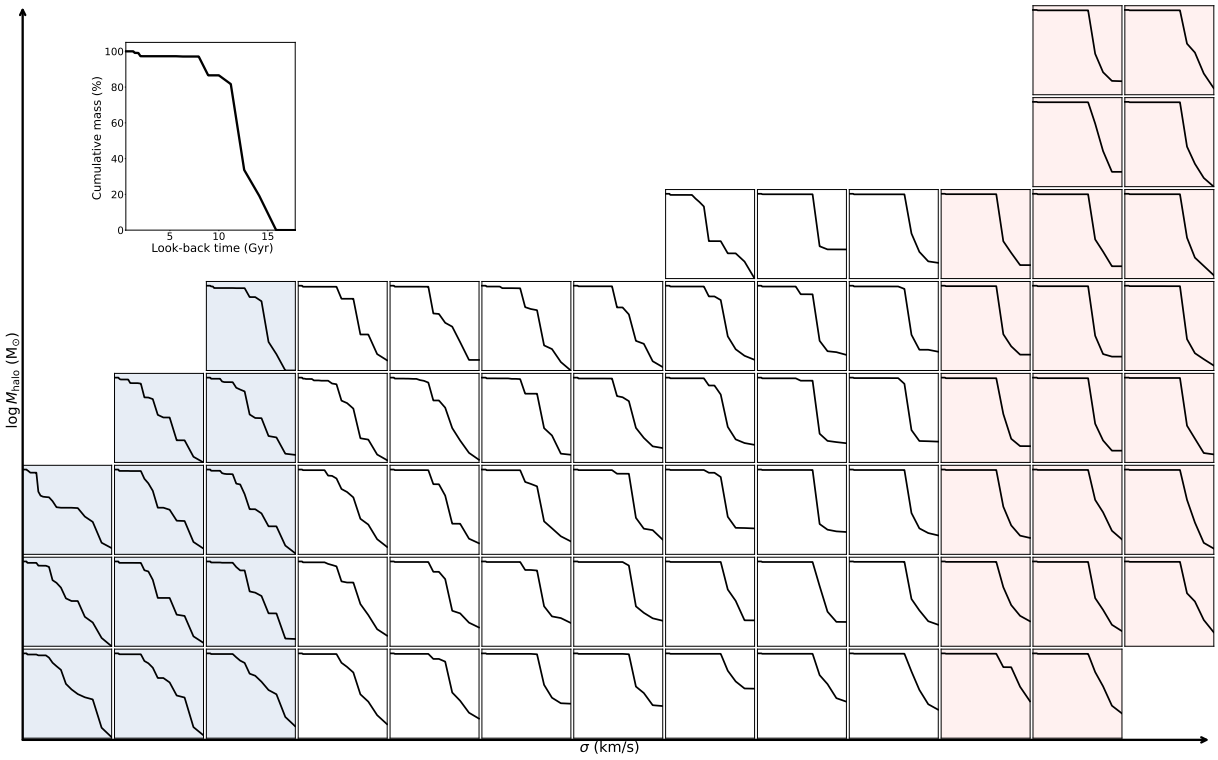

Figure 4.1 – Star formation history for each central galaxy in the full sample, across different ranges of σ (horizontal arrow) and $M_{\rm halo}$ (vertical arrow). Each box represents the cumulative initial mass contribution, attributed to each SSP, as a function of the look-back time (in Gyr). The blue and red shadows highlight the different SFH of low-and-high-σ central galaxies.

becomes more challenging. In summary, $M_{\rm halo}$ fails to effectively predict the α-Fe abundance ratio in the central galaxies of our sample, encompassing both ICs and GCs. This contrasts with σ, which has demonstrated a good indicator of this property.

4.2 PROBING THE ORIGIN OF THE EMISSION LINES

In this section, we focus on the ISM properties, analyzing $A_{\rm V}$ and EWHα which are indicators of gas content. Distinct mechanisms are responsible for producing emission lines and interstellar extinction. LINERs might show Hα signatures and other spectral lines from the narrow line region near the galaxy nucleus, while extinction can occur anywhere in the ISM, independent of nuclear activity.

Examining the gas component of the ISM, the variations in EWHα can be attributed to to different ionizing sources, including young main-sequence stars, nuclear activity, and hot evolved low-mass stars (HOLMES). To identify the ionizing agents in our galaxy sample, we use comparative techniques involving the relative fluxes of emission lines. It is noteworthy that elliptical galaxies, typically exhibiting weak emission lines, are predominantly ionized by HOLMES (Binette et al., 1994; Sarzi et al., 2010; Cid Fernandes et al., 2011b). We use the

BPT diagram to identify the ionization source in our sample. The BPT diagram, shown in the left panel of Figure 4.2, indicates that the dominant ionization pattern of all studied galaxies is LINER. However, while commonly used, Stasińska et al. (2008) show that the LINER region in this diagram contains a combination of two distinct galaxy families: those hosting a weak AGN and those ionized by HOLMES. Therefore, we employ the WHAN diagram (Cid Fernandes et al., 2010) as a supplementary tool. As shown in the right panel of Fig. 4.2, the WHAN diagram reveals that the typical ionization source for central galaxies in our sample is HOLMES. Using both diagrams, we show that the emission line ratios and equivalent widths observed in our stacked spectra are fully consistent with that of "retired" galaxies, objects whose gas ionization is due to HOLMES.

Each point in these diagrams shows the stacked data mentioned in Sect. 2.4. Even if galaxies in a stack have strong emission lines from nuclear activities or star formation, the spectrum still reflects the typical ionization pattern of that stacked spectra entire population. Our study indicates that HOLMES are still the main ionization source for central galaxies, including when we separate ICs and GCs (see Figure 2.

Our findings show that HOLMES is the ionizing agent, thereby eliminating the possibility of attributing variations in EWHα emission for others sources. We interpret these EWHα fluctuations relative to σ and $M_{\rm halo}$ as indicators of the mass fraction of ionizable gas within the galaxy. Herpich et al. (2016) confirms this findings, showing that elliptical galaxies with EWHα below 3 Å have the same ionizing agent, with differences in retired and passive galaxies mainly due to the variations in the amount of ionizable gas present in the galaxy.

In terms of $A_{\rm V}$, its value is influenced by the grains' geometry and the scattering efficiency's effect on the column density. If this column density correlates with the ionized gas column density, it naturally aligns with EWHα. Therefore, both $A_{\rm V}$ and EWHα are indicators of the ISM presence. Their coefficients will be indicators of the amount of gas in the galaxy and how these quantities change with σ and $M_{\rm halo}$. In our next discussion, we primarily focus on EWHα results, which indirectly is apply to $A_{\rm V}$ as well.

The decrease in EWHα with increasing σ (refer to Fig. 3.2, panels j, k, and l) might be attributed to various factors such as mergers, the re-absorption of expelled gas by the galaxy itself, or the absorption of peripheral gas. While we don't explore all possibilities, it is crucial to note that central galaxies, unlike other ETGs, are located in the centers of DM halos. This location makes them more susceptible to gas flows. Therefore, we propose that the variations in Hα emissions are due to differences in the efficiency of gas accretion and cooling, influenced by a combination of cooling flows and feedback mechanisms.

The observed increase in EWHα with $M_{\rm halo}$ suggests a potential association with a higher cold gas infall rate. Stott et al. (2012) propose an increased efficiency of the ICM cooling in massive halos to account for differences in the $L_X - T_X$ ratio between low and high $M_{\rm halo}$ systems. In order to provide a quantitative analysis, we develop a theoretical model that examines the interplay between two physical processes: AGN feedback and ICM cooling.

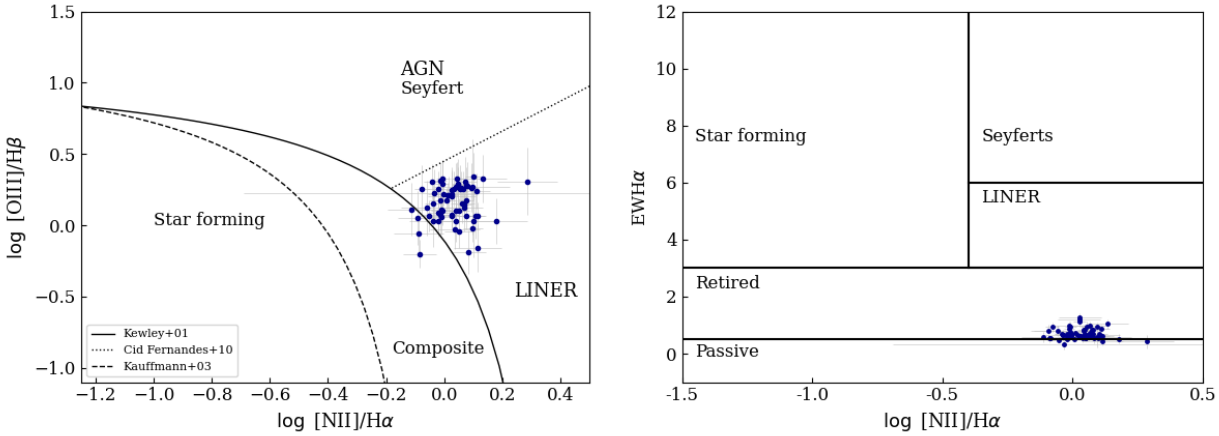

Figure 4.2 – The left panel shows the BPT diagram, which reveals that the dominant ionization pattern for central galaxies in the full sample is LINER, albeit with some cases exhibiting high uncertainty. In the right panel, the WHAN diagram indicates that HOLMES are the typical ionization source for the central galaxies in our sample.

4.3 MODELING THE GAS EMISSION VIA ICM COOLING FLOW AND AGN FEEDBACK

Aiming to understand systematic differences in some properties of BCGs in a sample of 123 X-ray emitting clusters, (Stott et al., 2012) investigated the relation between AGN feedback from the BCG and the ICM cooling. The authors argue that the thermodynamics of the ICM is set by the relative importance of the energy $E_{\rm AGN}$ released by AGN feedback over the cluster history to the thermal energy $E_{\rm ICM}$ of the ICM. An estimate of $E_{\rm AGN}$ was obtained for a typical radio-loud galaxy in their sample and expressed as a function of the feedback efficiency η, while considerations involving the dynamical equilibrium and the ICM temperature were then used to estimate the total thermal energy of the ICM as a function of M_{500}[1] and the ICM temperature T_X as

$$E_{\rm ICM} = \frac{3k_B}{2\mu m_p} T_X f M_{500}, \tag{4.1}$$

where f is the ICM mass fraction, k_B the Boltzmann constant, μ is the mean molecular weight of the constituent particles of the ICM and m_p is the proton mass.

If the presence of ionizable gas in a central galaxy is due to ICM cooling, the parameterisation of EWHα we have performed in Sect. 3.1.2 as a function of σ and $M_{\rm halo}$ maps the ICM cooling efficiency as compared to the energy output due to AGN feedback on the ICM. The typical timescales for ICM cooling in the center of clusters are much lower than 1 Gyr, and so we expect that, for a fixed total thermal energy for the ICM, the occurrence of an emission line in a central galaxy could be therefore the result of the interplay between the energy dissipation

[1]The mass contained in a radius within which the density of matter is 500 times the mean mass density of the Universe.

of the ICM by X-ray emission and the instantaneous kinetic energy output from AGN feedback, irrespective of the total energy that the latter has released to the ICM over cosmic time. In this case, the ξ is the ratio between the instantaneous kinetic power of the AGN feedback ($PE_{\rm BH}$) and the thermal energy of the ICM, ($E_{\rm ICM}$), i.e.

$$\xi = \frac{PE_{\rm BH}}{E_{\rm ICM}}, \tag{4.2}$$

effectively defines the Hα emission in central galaxies. Notice that ξ is equivalent (except for a multiplicative constant) to the $E_{\rm AGN}/E_{\rm ICM}$ ratio proposed by (Stott et al., 2012) for a fixed AGN lifetime.

In order to model the EWHα observed in our sample of central galaxies, we expand the above prescription, re-writing equation 4.2 as an explicit function of σ and $M_{\rm halo}$. We assume that the total mass $M_{\rm halo}$ of the cluster scales as $M_{\rm halo} \propto M_{500}$ and is also proportional to the cluster total volume, so that $M_{\rm halo} \propto R^3$, where R is a characteristic radius. We also assume an equilibrium condition where the temperature of the gas, T_X, scales with the average kinetic energy of the galaxies in the cluster, i.e. to the square of the dispersion in the values of the individual velocities of the galaxies of the system (Lubin; Bahcall, 1993). For a spherically symmetric, homogeneous and virialized distribution of particles of total mass M and radius R, σ^2 scales with M/R. We then obtain

$$E_{\rm ICM} \propto \frac{M_{\rm halo}}{R} M_{\rm halo} \propto \frac{M_{\rm halo}}{M_{\rm halo}^{1/3}} M_{\rm halo} \propto M_{\rm halo}^{1.67}. \tag{4.3}$$

We further assume that the instantaneous kinetic power of the AGN feedback $PE_{\rm BH}$ scales with the accretion rate by the SMBH with a constant efficiency ε, i.e.

$$PE_{\rm BH} = \varepsilon \dot{M_{\rm BH}} c^2. \tag{4.4}$$

We now need a recipe for expressing the accretion rate of the SMBH in terms of the physical parameters that describe the galaxies in each stack, i.e. their σ and $M_{\rm halo}$. The Bondi (Bondi, 1952) mechanism has been shown to be efficient in describing several properties of BCGs (Fujita; Kawakatu; Shlosman, 2014). In this scenario, the feeding of the SMBH occurs through the accretion of hot gas from its surroundings, when the gravitational potential exceeds the thermal energy of the gas. This accretion mode is radiatively inefficient, producing a feedback that is mostly mechanical, in the form of jets. The fact that radio galaxies present typically an early-type morphology, and that the probability of an ETG to be a radio galaxy is even higher if it is a central system, reinforces the use of the Bondi scenario as a first approximation. This model implies that the accretion rate of the SMBH is proportional to the square of its mass. Assuming that the gas densities, the speed of sound in the surrounding medium and the Bondi radii are homogeneous across all bins of σ and $M_{\rm halo}$, we get $\dot{M}_{\rm BH} \propto M_{\rm BH}^2$, what results in

$$PE_{\rm BH} \propto M_{\rm BH}^2. \tag{4.5}$$

To explicitly couple $PE_{\rm BH}$ with the global properties of their host galaxies, we use the parameters of the $M_{\rm BH} - \sigma$ relation derived by (Kormendy; Ho, 2013). This results in $M_{\rm BH} \propto \sigma^{4.38}$, and therefore

$$PE_{\rm BH} \propto \sigma^{8.76}. \tag{4.6}$$

Substituting the expressions for $PE_{\rm BH}$ and $E_{\rm ICM}$ in equation 4.2, we finally obtain

$$\xi \propto \sigma^{8.76} M_{\rm halo}^{-1.67}. \tag{4.7}$$

Low values of ξ imply that the power of the AGN feedback is small for a fixed total thermal energy of the ICM. This in turn results in large ICM cooling rates; the flow of gas into the central galaxy then enhances Hα emission. The effect of the ICM cooling in the Hα luminosity can therefore be parameterized as

$$L_{\rm H\alpha} \propto \xi^{\gamma}, \tag{4.8}$$

where γ is a *negative* coefficient whose absolute value depends on the detailed physics of ICM cooling and heating mechanisms.

The above prescription for $L_{\rm H\alpha}$ can be transformed into a similar one for EWHα in the following way. By definition,

$$\mathrm{EWH}\alpha = \frac{F_{\rm H\alpha}}{\overline{F_{\rm C}}}, \tag{4.9}$$

where $F_{\rm H\alpha}$ is the flux of the Hα line and $\overline{F_{\rm C}}$ is the average level of the spectral continuum at the position of the Hα line. This expression can be converted in a ratio involving $L_{\rm H\alpha}$ by means of

$$\mathrm{EWH}\alpha = \frac{F_{\rm H\alpha}}{\overline{F_{\rm C}}} \frac{4\pi D_{\rm L}^2}{4\pi D^2} \equiv \frac{L_{\rm H\alpha}}{L_{\rm C}}, \tag{4.10}$$

where $D_{\rm L}$ is the luminosity distance of the galaxy. The factor $L_{\rm C} \equiv \overline{F_{\rm C}} 4\pi D^2$ – the average luminosity density of the spectral continuum at the position of the Hα line – can be estimated by the (fiber) luminosity of the galaxy in a spectral window around the Hα line, what roughly corresponds to the high wavelength limit of the passband of the SDSS r filter at the typical redshifts of our sample of centrals. The r-band absolute magnitudes are available from the SDSS, but this is not a good proxy for $L_{\rm C}$, because in general only a fraction of the galaxy light is included in the SDSS spectroscopic fiber (and this fraction is strongly dependent on the redshift of the galaxy). Assuming that the galaxy is homogeneous and therefore the ratio between the fiber ($f_{r,F}$) and total ($f_{r,T}$) r-band fluxes of the galaxy is equal to the ratio between the respective luminosities ($L_{r,F}$, $L_{r,T}$), we get

$$L_{r,F} = \frac{f_{r,F}}{f_{r,T}} L_{r,T}. \tag{4.11}$$

Using the CASJOBS[2] environment, we obtain the values of $f_{r,F}$, $f_{r,T}$ and $L_{r,F}$ for the galaxies in each stack and derive $L_{r,F}$. Finally, we average the $L_{r,F}$ values across all galaxies in a stack to get $L_{\rm C}$.

It is important to note that $L_{\rm C}$ is the average r-band fiber luminosity per stack; just like other physical parameters, it may also be a function of σ and $M_{\rm halo}$. We have quantified such dependence in Figure 4.3, using the same fitting procedure described Sect. 3.1.2. The best-fit coefficients are obtained using a non-linear method of least squares using the curve fit from SciPy Python library. The uncertainties applied to this method are given by the standard deviation measured for each property for the individual galaxies in each stack. After performing these fits, the EWHα can finally be expressed as

$$\begin{aligned} \log {\rm EWH}\alpha \propto\ & [8.76\gamma - (0.75 \pm 0.04)] \log \sigma + \\ & [-1.67\gamma - (0.042 \pm 0.006)] \log M_{\rm halo} \end{aligned} \tag{4.12}$$

for the full sample, and

$$\begin{aligned} \log {\rm EWH}\alpha \propto\ & [8.76\gamma - (0.66 \pm 0.03)] \log \sigma + \\ & [-1.67\gamma - (0.153 \pm 0.008)] \log M_{\rm halo} \end{aligned} \tag{4.13}$$

and

$$\begin{aligned} \log {\rm EWH}\alpha \propto\ & [8.76\gamma - (0.86 \pm 0.04)] \log \sigma + \\ & [-1.67\gamma - (0.030 \pm 0.005)] \log M_{\rm halo}, \end{aligned} \tag{4.14}$$

respectively, for ICs and GCs.

Equations 4.12 to 4.14 contain a set of theoretical coefficients of the relation EWH$\alpha \sim \sigma^A M_{\rm halo}^B$ that can be directly compared to those obtained in Sect. 3.1.2. Such coefficients are numerically defined except for the exponent γ, which is an unknown in our model but whose value can be obtained directly by comparison with the measured coefficients in Table 3.1. It is important to note that, as γ is included in both theoretical coefficients, it can be solved for the value that produces the best agreement between the theoretical and measured ones. We obtain $\gamma_{\rm full} = -0.05 \pm 0.03$, $\gamma_{\rm iso} = -0.16 \pm 0.07$ and $\gamma_{\rm group} = -0.01 \pm 0.01$ for the full sample, ICs and GCs, respectively. Such values result in theoretical coefficients that are consistent with the measured ones (Tab. 3.1) within 2σ. The existence of a solution for γ that allows for a

[2] https://skyserver.sdss.org/casjobs/

good match between the theoretical and measured coefficients – and also presents the correct (negative) sign as expected – is suggestive that the AGN feedback power relative to the ICM internal energy indeed regulates the gas flow into the body of the central galaxy.

Isolated centrals are the population for which we obtain the highest absolute value of γ; taking into account its uncertainty, $\gamma_{\rm iso}$ is different from zero at more than 95% statistical confidence. This suggests that, for this sub-population, EWHα responds to the ratio between $PE_{\rm BH}$ and $E_{\rm ICM}$. The interpretation given earlier to explain the observed trends for the stellar populations for IC still holds: ICs are able to retain their halo of hot gas more efficiently than GCs, which often lose a considerable amount of their gas through environmental processes. By maintaining their halo of hot gas, ICs can continue cooling, forming new stars and replenishing their ionized gas budget, eventually triggering an active phase and repeating this process as long as the gas reservoir exists. This leads to a more extended SFH, a younger and more metal-rich stellar population, and an ionized gas signature regulated by AGN feedback.

On the other hand, the value of $\gamma_{\rm group}$ is consistent with zero within its uncertainty. If γ is set to zero, then $L_{\rm H\alpha}$ is independent of the ratio between the kinetic power of the AGN and the thermal energy of the ICM and our model fails to adequately describe the EWHα values. This suggests that the GCs are less efficient in retaining their hot gas halo compared to ICs and the signal of the interplay between such processes is confounded by other mechanisms that also participate in the heating and cooling of the ICM in GCs. In fact, gas sloshing due to galaxy mergers or simply by the motions of galaxies close to the central regions of the halo – e.g. (Ruszkowski; Oh, 2011) – may also be relevant sources of ICM heating in the group environment. Conversely, central galaxies in groups are subjected to merging, a phenomenon that can displace the central's SMBH and effectively disrupt the feeding-feedback cycle (Chu; Boldrini; Silk, 2023). The scenario of accretion of gas-rich, low-mass galaxies that we have already invoked to explain the SFH of GCs, may also play an important role in setting the Hα emission in such galaxies, as it introduces both younger stars and gas. Considering the mass fractions in central galaxies with low σ values shown in Figure 4.1, it is possible that a significant number of stars have recently been included into the system via mergers; the recently-acquired gas is then ionized by the radiation field of HOLMES, contributing to the EWHα signature observed in our sample. In short, the gas deposition in central galaxies in groups seems to be more complex than a single AGN power versus ICM thermal energy prescription, as opposed to ICs; instead, other mechanisms that also contribute to ICM heating and cooling processes must play an important role.

4.4 CORRELATING RADIO AND Hα EMISSIONS

In Section 3.2, we find that $L_{\rm R}$ increases with both σ and $M_{\rm halo}$ for all stacked radio data, independent of the environment. But for $M_{\rm halo}$, it looks like the increase is stronger for ICs than

Figure 4.3 – Following the same pattern of Fig. 3.1, we present the correlation of the fiber luminosity with σ and $M_{\rm halo}$ for each central galaxy bin in the full sample, ICs and GCs, from left to right, respectively.

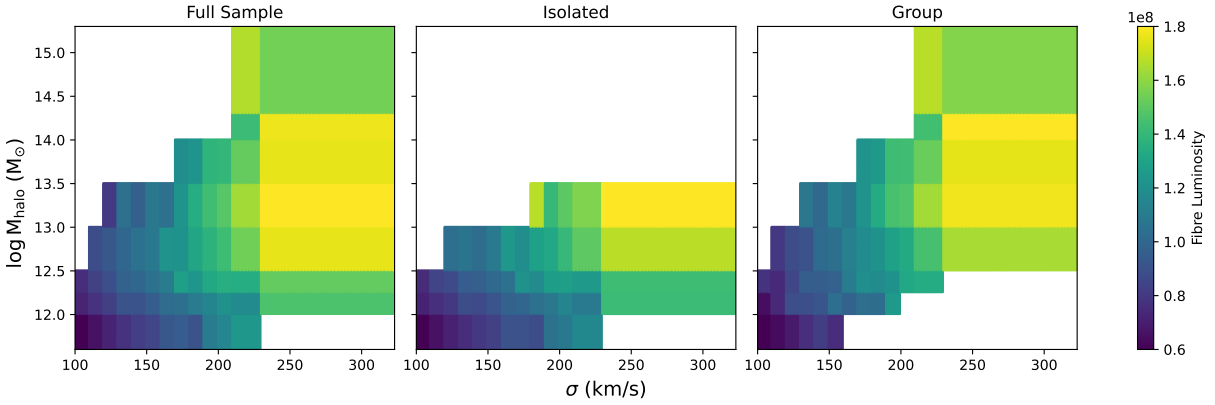

for GCs. The increase of $L_{\rm R}$ with σ, for both ICs and GCs, are indirectly linked to the increases of the SMBH mass given the σ - $M_{\rm BH}$ relation (Magorrian et al., 1998). An increase in the SMBH mass implies a higher accretion rate, considering the Bondi model, as seen in Sect. 4.3. Considering that an increased accretion rate of the SMBH results in more effective conversion of gravitational potential energy into mechanical energy, thereby enhancing radio emissions. However, the lack of a relation between $L_{\rm R}$ and $M_{\rm halo}$ is more challenging to interpret. We observe that radio galaxies tend to be in group environments, which naturally have more massive halos (Best et al., 2005).

When examining individual galaxies, it is observed that isolated ones show no significant dependence of their $L_{\rm R}$ on σ or $M_{\rm halo}$. However, for galaxies in clusters (GCs), there is a slight dependency of $L_{\rm R}$ on both these factors. Studying BCGs in group environments, (Yuan; Han; Wen, 2016) reports no substantial correlation between radio power and σ. The authors also notes a tendency, albeit weak, for more powerful radio BCGs in cluster environments to be hosted by more massive clusters. This is interpreted as a result of more massive clusters possessing greater gravitational potential, leading to BCGs more likely hosting SMBHs with higher accretion rates. Such an increased accretion rate could elevate AGN activity, thereby intensifying radio emissions from the BCGs. Moreover, Best et al. (2007) find that the distribution of radio luminosity for BCGs does not depend significantly on cluster mass.

Before drawing any conclusions from these observations, it is crucial to verify that the radio emissions we detect are indeed originating from AGNs. Typically, radio sources can be attributed to two main causes: AGNs or star formation processes. While AGNs are known for their powerful emissions and reach at high z, galaxies with intense star formation usually exhibit weaker radio emissions and are common in spiral and irregular galaxies.

In Figure 4.4, we investigate the ionizing sources of radio emitting galaxies in our sample. In the left panel, we present the percentage of galaxies with radio emission for each optical emission class (Star-forming, Seyfert, LINER, Passive and Retired galaxies, from left to right,

respectively). Notice that only one of the radio-emitting galaxies in our sample is star formation. Additionally, the majority of the observed galaxies exhibited radio emissions that exceeded the typical luminosity threshold associated with star formation ($L_{1.4\,GHz} \lesssim 10^{22}\,\mathrm{W\,Hz^{-1}\,sr^{-1}}$). Thus, our investigation reinforces that radio emission in our sample is predominantly caused by AGN activities.

Furthermore, Figure 4.4 reveals that, among the radio-emitting galaxies in our sample, the majority are retired, accounting for $\sim 64\%$. Interestingly, passive galaxies, which constitute the bulk of our sample, represent $\sim 22\%$ of the radio galaxies. LINERs are in third place with $\sim 8\%$, followed by Seyferts at $\sim 3\%$, while star-forming galaxies comprise only $\sim 0.2\%$ in this ranking. Based on our radio sample, it appears that the probability of a radio galaxy being classified as a retired galaxy is greater than for other categories. When we plot the percentage of galaxies of each class with radio emission, Seyferts exhibit the highest percentage among the classes ($\sim 14\%$), with LINERs in second place at $\sim 9\%$. Star-forming galaxies are third with $\sim 4\%$, while retired and passive galaxies account for $\sim 4\%$ and $\sim 2\%$, respectively. This could suggest that Seyfert galaxies have a higher propensity to be radio galaxies compared to other classes in our sample, implying that radio emission is somehow correlated with optical emission related to AGN in our sample galaxies. .

Figure 4.4 – Left panel: Percentage of radio-emitting galaxies that have optical emission, divided by each optical emission class. Right panel: Percentage of galaxies in each class that have radio emission.

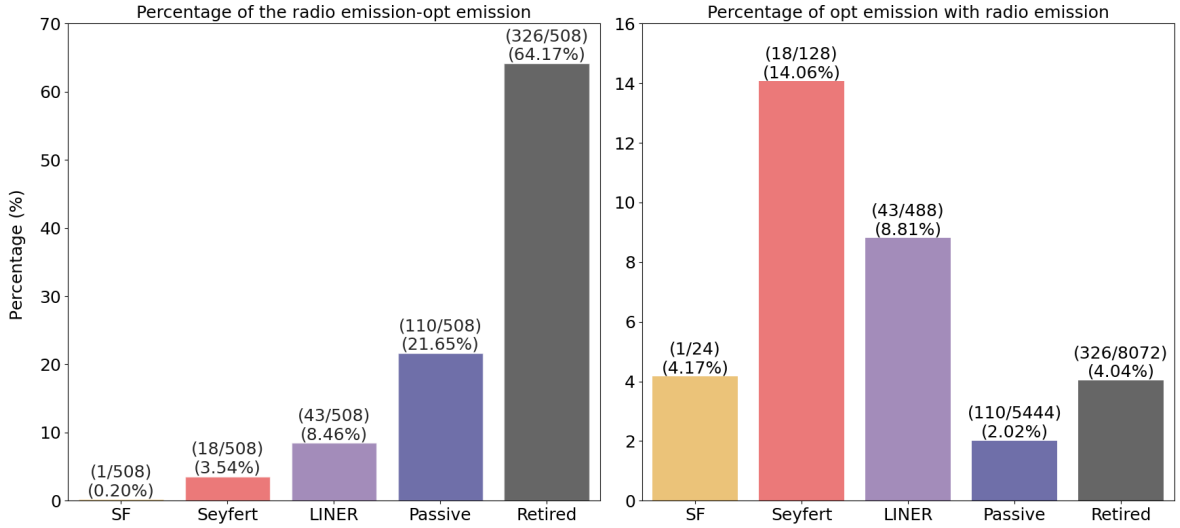

We further investigate the correlation between radio and optical emission by calculating the Hα luminosity ($L_{\mathrm{H}\alpha}$) and comparing it to L_{R}. We estimate $L_{\mathrm{H}\alpha}$ for both stacked spectra and for individual galaxies using the Hα flux measured in Sect. 2.5 and the luminosity distance, calculated from the galaxy redshifts; the luminosity distance for the stacked spectra is calculated by using the median redshift of the galaxies in each stack. In Figure 4.5, we see a small positive

correlation between the properties, with a Pearson coefficient (r) of about 0.15 and a p-value around 10^{-3}. This indicates some statistical significance. However, due to the weak correlation and high dispersion, we should consider if other factors are influencing the relation between these luminosities. To explore this, we compared $L_{\mathrm{H}\alpha}$ with redshift in Figure 4.6, especially since L_{R} also increases with redshift as seen in Figure 3.11. Additionally, we examine how $L_{\mathrm{H}\alpha}$ relates to σ and M_{halo} in GCs, shown in Figures 4.8. It is important to note that $L_{\mathrm{H}\alpha}$ data in these figures are only from galaxies with radio emission.

Despite the scatter, Figure 4.6 indicates an increase of $L_{\mathrm{H}\alpha}$ with z. The increase of $L_{\mathrm{H}\alpha}$ with z is more complex than we find for L_{R}. The SPIDER sample is already complete for the z range considered, indicating a different reason for this trend. Another possibility is that the Hα emission extends beyond the SDSS fiber capture area at higher z. Galaxies farther away seem smaller, then the fiber spans more of the galaxy area, leading to a higher $L_{\mathrm{H}\alpha}$. To address this issue, we plot the trend line for the luminosity correction in this diagram of $L_{\mathrm{H}\alpha}$ *vs.* z assuming a homogeneous distribution of Hα in the galaxy. Considering the idealization of the model and the scatter in the data, we conclude that the dependence of Hα with z is mostly due to aperture effects. In fact, inspecting the Hα flux maps of the 20 galaxies of our sample observed in MaNGA Survey (Bundy et al., 2015), we find that the Hα emission although predominantly concentrated in the nuclear region extends beyond the limits of the SDSS fiber diameter (see examples in Figure 4.7).

Figure 4.5 – Relation between the radio luminosity (L_{R}) and Hα luminosity ($L_{\mathrm{H}\alpha}$). The Pearson coefficient (r) and the p-value are displayed in lower right corner.

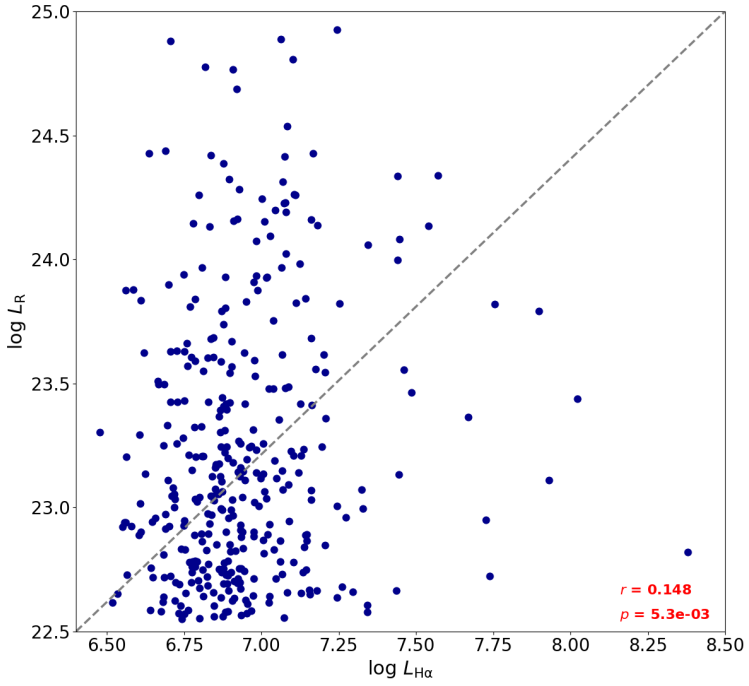

Figure 4.6 – Relation between Hα luminosity ($L_{\mathrm{H}\alpha}$) and the redshift (z).

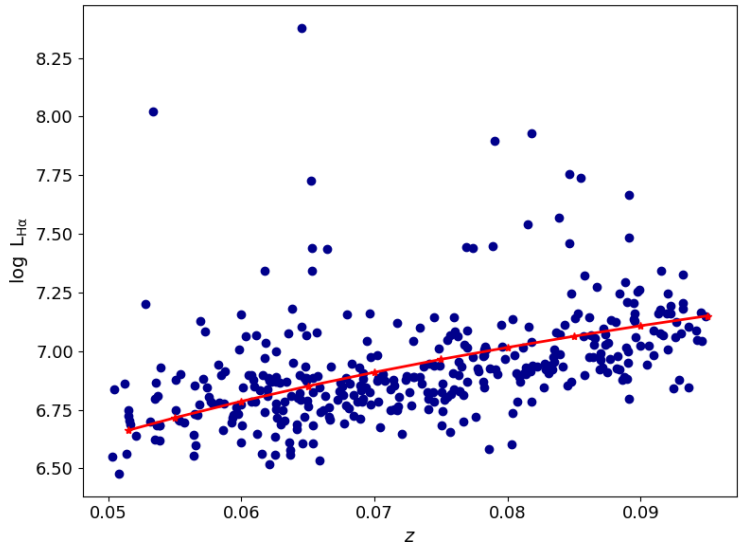

Figure 4.7 – Maps of Hα flux of six radio-emitting galaxies of our sample, extracted from the MaNGA Survey.

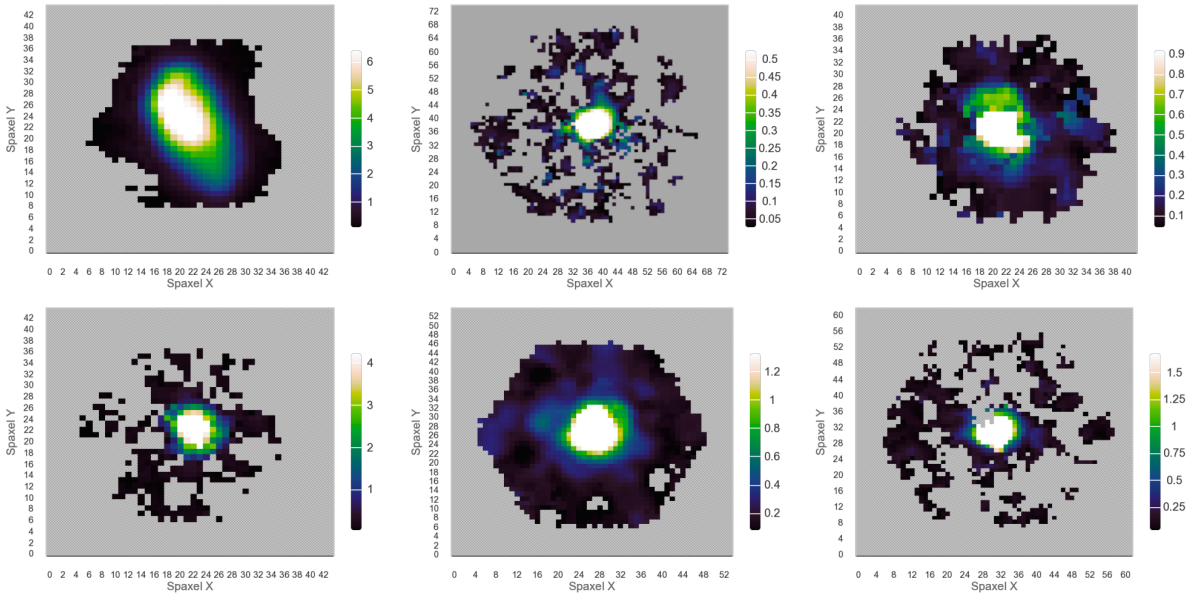

Regarding the relation between $L_{\mathrm{H}\alpha}$, σ, and M_{halo}, we turn our attention to Figure 4.8. The structure of this figure is consistent with that of Figure 3.13, showing the relation between $L_{\mathrm{H}\alpha}$ with σ and M_{halo} for the full sample in the upper left and right panels, respectively. This is followed by the data for ICs and GCs in the middle and bottom panels. An increase in $L_{\mathrm{H}\alpha}$ with σ is clearly observed, while its relation with M_{halo} is less distinct. It appears that

$L_{\mathrm{H}\alpha}$ increases up to $\log M_{\mathrm{halo}} \sim 13.0\,(\mathrm{M}_{\odot})$ and then levels off into a plateau. For ICs, there is a noticeable increase in $L_{\mathrm{H}\alpha}$ for both parameters, and this seems even more pronounced in relation to M_{halo}. In the case of GCs, $L_{\mathrm{H}\alpha}$ also increases with σ. However, while there seems to be an increase in $L_{\mathrm{H}\alpha}$ with M_{halo} for GCs, this trend is not as evident. This result is obtained for a specific sub-population of the sample, i.e., those with radio emissions. Therefore, we can assess the behavior of the entire population using the results we obtain through the stacked method. Figure 4.9 illustrates the relation between L_{R} and $L_{\mathrm{H}\alpha}$ for the stacked spectra/radio images, showing the trends for the full sample, ICs, and GCs, from left to right, respectively. We observe a more pronounced relation between these two properties when examining the panels for the full sample and ICs, compared to the analysis of the individual sample of radio-emitting galaxies. However, in the case of GCs, no significant relation between L_{R} and $L_{\mathrm{H}\alpha}$ is observed. This scatter observed for GCs likely reflects in the dispersion found in Figure 4.5, considering that the majority of galaxies with radio emissions are GCs (66% of the radio emission sample). It is noteworthy that to measure the radio and Hα luminosity for the stacked spectra/radio images, we must estimate the luminosity distance using the median z of the galaxies in each stack. We observe significant variations in luminosity distance within the bins of σ and M_{halo}. However, this effect is consistently observed across all ranges.

Figure 4.8 – Relation between the Hα luminosity ($L_{\mathrm{H}\alpha}$) of individual radio-emitting galaxies in our sample and their velocity dispersion (σ) and halo mass (M_{halo}) is presented for the full sample, isolated centrals (ICs), and group centrals (GCs), shown from top to bottom, respectively.

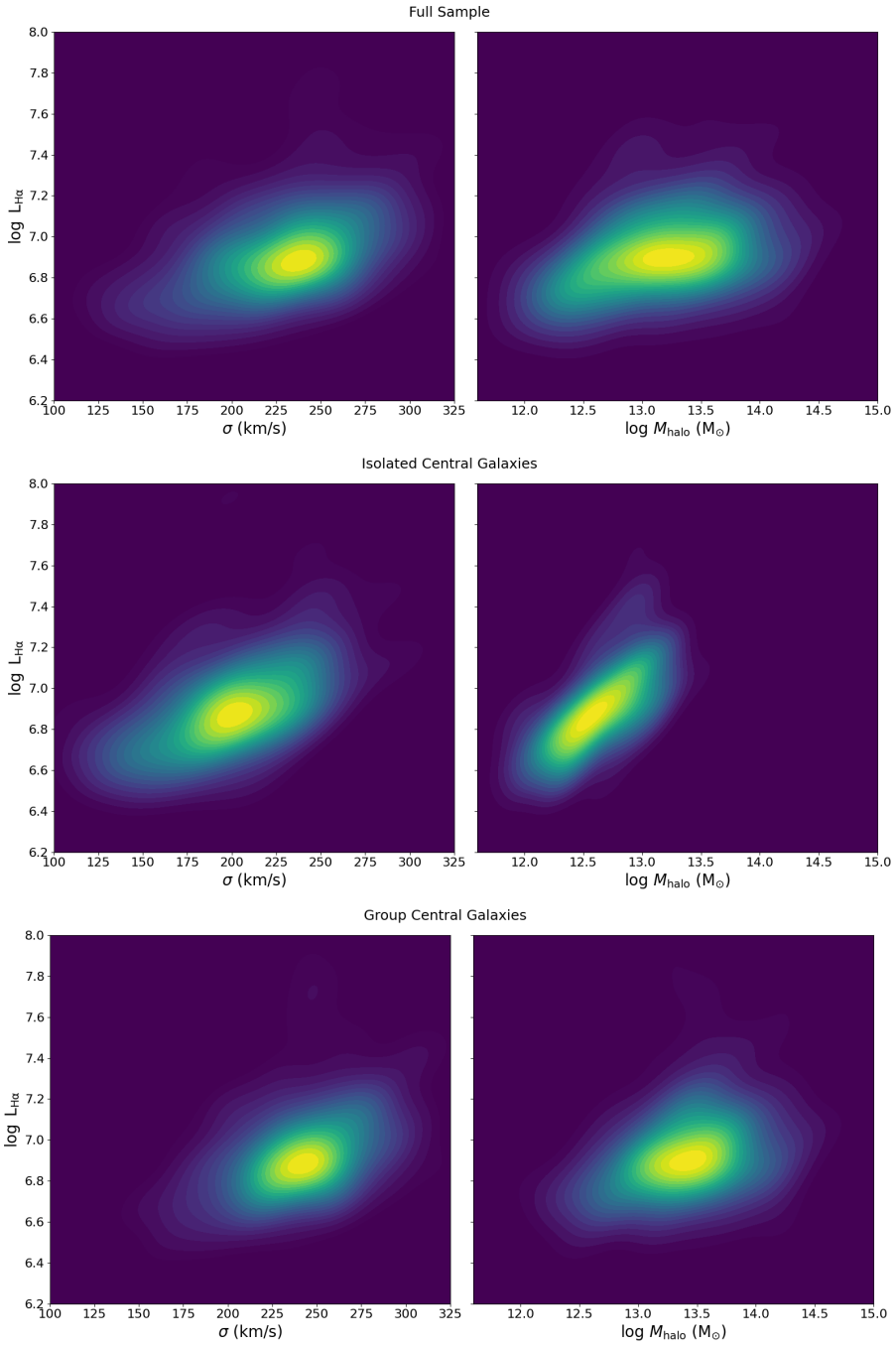

Figure 4.9 – Relation between radio luminosity ($L_{\rm R}$) and Hα luminosity ($L_{\rm H\alpha}$) for the stacked spectra/radio images in our sample, along with their velocity dispersion (σ) and halo mass ($M_{\rm halo}$). The full sample, isolated centrals (ICs), and group centrals (GCs) are displayed sequentially from left to right.

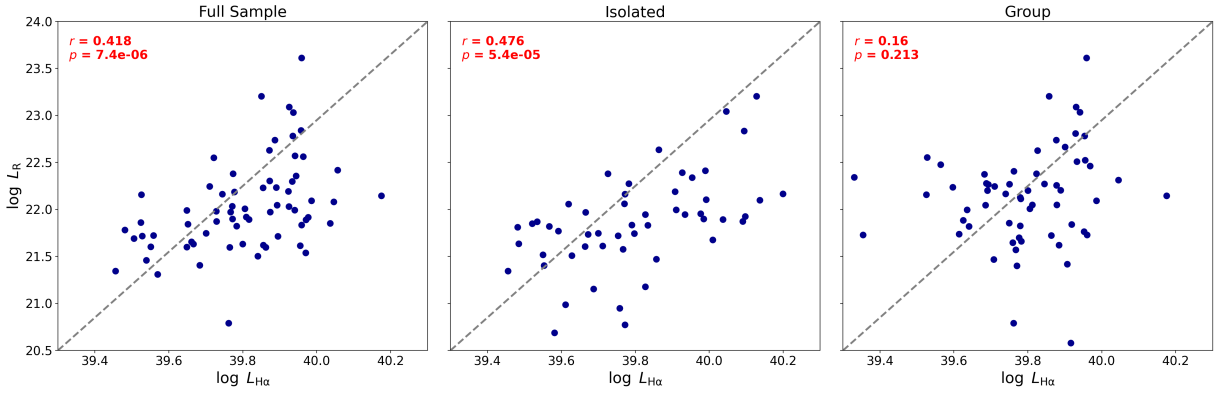

4.5 REVISING THE GAS EMISSION MODEL: ENHANCING THE RECIPE FOR AGN FEEDBACK POWER

In Sect. 4.3 we use only optical data to explain the occurrence of ionized gas in the galaxies of our sample as a function of σ and $M_{\rm halo}$. We now revisit our modeling in light of the radio results. We observed that the effect of ICM cooling on the Hα luminosity can be parameterized as $L_{\rm H\alpha} \propto \xi^{\gamma}$, where ξ represents the ratio between the instantaneous kinetic power of AGN feedback ($PE_{\rm BH}$) and the thermal energy of the ICM ($E_{\rm ICM}$), with γ being a negative value. We use the Bondi model to scale $PE_{\rm BH}$ with the SMBH mass and, indirectly, with the galaxy mass and consequently, with σ, given the $M_{\rm BH} - \sigma$ relation derived by (Kormendy; Ho, 2013).

Now, we have an observational indicator of AGN power, which is the radio luminosity ($L_{\rm R}$). We can review the model and instead of assuming an AGN power associated to the Bondi model, we use the dependency of $L_{\rm R}$ with σ and $M_{\rm halo}$ as a recipe for $PE_{\rm BH}$ estimate. Cavagnolo et al. (2010) propose a relation between the cavity power and radio luminosity given by

$$P_{\rm cav} = 5 \times 10^{43} \left(\frac{L_{1.4\,\rm GHz}}{10^{40}\,\rm erg\,s^{-1}} \right)^{0.7} \rm erg\,s^{-1}. \tag{4.15}$$

This cavity power represents an estimate of the minimum mechanical feedback into the ICM. As presented in Sect. X we have parameterized $L_{1.4\,\rm GHz}$ as a function of σ and $M_{\rm halo}$ and find coefficients presented in Table 3.2. We can therefore obtain an expression for the mechanical feedback from the AGN as a function of σ and $M_{\rm halo}$ by substituting such coefficients into Eq. 4.15, i.e.

$$P_{\rm cav} \propto L_{\rm R}^{0.7} \propto \sigma^{0.7A} M_{\rm halo}^{0.7B}. \tag{4.16}$$

This results in the following recipes for the mechanical feedback of the AGN, for the full sample, ICs and GCs, respectively:

$$P_{\rm cav,Full} \propto \sigma^{2.18\pm0.43} M_{\rm halo}^{0.31\pm0.07} \tag{4.17}$$

$$P_{\rm cav,IC} \propto \sigma^{1.26\pm0.40} M_{\rm halo}^{0.72\pm0.12} \tag{4.18}$$

$$P_{\rm cav,GC} \propto \sigma^{1.61\pm0.78} M_{\rm halo}^{0.26\pm0.13} \tag{4.19}$$

In comparison with our previous recipe for $PE_{\rm BH}$, we notice striking differences in the above prescriptions. First, the exponent of σ in the above set of equations is always much lower then the expected from a direct application of the Bondi model. This suggests that either the power of AGN mechanical feedback is not proportional to the accretion rate or the effective accretion rate scales to a sub-unit power of σ. Second, there appears a dependence on $M_{\rm halo}$ that does not appear explicitly in the Bondi model. This dependence probably reflects variations in the ICM density (which we have ignored in our previous modeling) as a function of $M_{\rm halo}$. These equations can therefore encompass aspects related to the accretion rate and available accretion material which we had previously marginalized due to our assumptions that the ICM density was uniform across all clusters, that the feedback power was proportional to the SMBH accretion rate, and that the accretion rate was exactly was prescribed in the Bondi model.

Substituting $PE_{\rm BH}$ by the $P_{\rm cav}$ expressions into Eq. 4.2 we obtain

$$\xi_{\rm full} \propto \sigma^{2.18\pm0.43} M_{\rm halo}^{-1.36\pm0.07}, \tag{4.20}$$

$$\xi_{\rm IC} \propto \sigma^{1.26\pm0.40} M_{\rm halo}^{-0.95\pm0.12}, \tag{4.21}$$

$$\xi_{\rm GC} \propto \sigma^{1.61\pm0.78} M_{\rm halo}^{-1.41\pm0.13}, \tag{4.22}$$

what results in the following predictions for the EWHα values:

$$\log \mathrm{EWH}\alpha_{\mathrm{full}} \propto \left[(2.18\pm0.43)\,\gamma-(0.75\pm0.04)\right]\log\sigma + \left[(-1.36\pm0.07)\,\gamma-(0.042\pm0.006)\right]\log M_{\mathrm{halo}} \quad (4.23)$$

$$\log \mathrm{EWH}\alpha_{\mathrm{iso}} \propto \left[(1.26\pm0.40)\gamma-(0.66\pm0.03)\right]\log\sigma + \left[(-0.95\pm0.12)\gamma-(0.153\pm0.008)\right]\log M_{\mathrm{halo}} \quad (4.24)$$

$$\log \mathrm{EWH}\alpha_{\mathrm{group}} \propto \left[(1.61\pm0.78)\gamma-(0.86\pm0.04)\right]\log\sigma + \left[(-1.41\pm0.13)\gamma-(0.030\pm0.005)\right]\log M_{\mathrm{halo}}. \quad (4.25)$$

Estimating the γ values by using the same methodology used in Sect. 4.3 we find $\gamma_{full} = -0.08\pm0.09$, $\gamma_{iso} = -0.37\pm0.18$ and $\gamma_{group} = +0.015\pm0.030$. Contrasting these γ values with the previous ones we find no differences for the group centrals, for which γ_{group} is essentially null. Likewise, the absolute value of γ_{full} still very small, suggesting that the Hα emission is mostly insensitive to an ICM cooling *vs*. AGN feedback for our full sample of centrals. In contrast, the absolute value of the new γ_{iso} is appreciably higher than the previous one. Once again, ICs stand out as a population for which the AGN feedback power relative to the ICM internal energy seems to regulate its Hα content. In fact, the differences between ICs and GCs become still stronger when using a modeling for PE_{BH} derived directly from the observed radio luminosity. This result suggests that modeling the PE_{BH} by parameterizing L_{R} gives us a better description about radio AGN feedback in central galaxies, increasing our sensibility to reveal the contribution of cooling phenomena *vs*. AGN feedback as a gas deposition mechanism in central galaxies.

5 CONCLUSIONS

In this work, we explore the characteristics of the stellar population and the interstellar medium in a sample of 15,107 early-type central galaxies, selected from the SPIDER survey (La Barbera et al., 2013). The primary goal is to understand the evolution of baryonic matter in these galaxies. We use optical spectra from the SDSS to estimate parameters such as Age, Z, $A_{\rm V}$, EWHα and [α/Fe]. We also derive information about radio emission in this sample by using images extracted from the VLA FIRST Survey. Our study mainly focuses on how these parameters correlate with the central velocity dispersion (σ) and the halo mass ($M_{\rm halo}$) in both isolated (ICs) and group (GCs) central galaxies. We use BPT and WHAN diagrams to identify the ionization sources and suggest a theory involving a Bondi accretion process to explain the gas dynamics in these central galaxies. Moreover, we integrate radio luminosity ($L_{\rm R}$) into our model to enhance our recipe for the AGN feedback power. Key conclusions of our study are summarized below:

- We find that ICs and GCs show a similar trend with σ – older and more metal rich stellar populations as σ increases. Additionally, when considering a fixed σ, we observe a trend of younger Ages associated with higher values of $M_{\rm halo}$s. Remarkably, both ICs and GCs display consistent correlations between these parameters, suggesting a coherent final star formation history. This holds true regardless of whether the central galaxy acquires gas from its own halo (as in ICs) or from accreted gas-rich systems (as in GCs).

- We observe an increase in the [α/Fe] ratio with higher values of σ. This suggests shorter star formation timescales in more massive galaxies, a finding that aligns with our analysis of their star formation history. In contrast, $M_{\rm halo}$ does not effectively predict the α-Fe abundance ratio in the central galaxies of our sample. However, in the lower $M_{\rm halo}$ regime for ICs, an excess of [α/Fe] is observed, consistent with the findings reported in La Barbera et al. (2014). Nevertheless, since the difference they find is small, about 0.1 dex, discerning variations across different $M_{\rm halo}$ ranges and comparing ICs and GCs becomes more challenging.

- In both ICs and full sample, we observe a consistent increase in $A_{\rm V}$ and EWHα as σ decreases and $M_{\rm halo}$ increases. The trends of these parameters with $M_{\rm halo}$ are not clear for GCs due to larger scatter. For ICs, the variation with $M_{\rm halo}$ becomes less evident at $\sigma > 200\,{\rm km\,s^{-1}}$. Also, the variation with sigma flattens out for all systems above $200\,{\rm km\,s^{-1}}$. The similarity between these properties is further supported by the values obtained through our parameterisation, indicating that both σ and $M_{\rm halo}$ serve as indicators of the ionizable gas content in the central galaxies of our sample. The linear combination of these parameters provides valuable insights into the properties of the ionizable gas in these systems.

- In the case of ICs, we successfully reproduce the observed values of EWHα by using a model that takes into account the interplay between the kinetic power of AGN ($PE_{\rm BH}$) and the thermal energy of the ICM ($E_{\rm ICM}$), providing an explanation for gas deposition in these central galaxies.

- We have identified a subset of 508 galaxies in our sample that exhibit radio emissions indicative of nuclear activity. This is evidenced by the absence of a young stellar population or star-forming activities in these galaxies, coupled with the trend we find linking these emissions to Seyferts. Additionally, applying the stacked images methodology reveals that radio luminosity density ($L_{\rm R}$) increases with both σ and $M_{\rm halo}$, a trend consistent across different environments. However, the correlation with σ and $M_{\rm halo}$ is not evident in the ICs when examining these radio-emitting galaxies individually. Notably, the trend observed in stacked images for GCs remains when analyzing the sample individually.

- Interpreting $L_{\rm R}$ as an indicator of the kinetic power of the AGN, and adapting our previous model to this new configuration for the $PE_{\rm BH}$, we successfully explain the Hα emission in the case of ICs. However, when applying the same model to GCs, it fails, again, to adequately describe the EWHα values. These findings suggest that ICs are more efficient in retaining their hot gas halo compared to GCs. In the case of GCs, the influence of AGN feedback on ICM thermodynamics may be confounded by other mechanisms that also contribute to the heating and cooling processes within the ICM in GCs.

Our findings indicate intrinsic differences between isolated and group central galaxies. Isolated central galaxies effectively retain their hot gas halo, enabling efficient cooling and reheating. In contrast, gas deposition in group central galaxies is a complex process, involving factors beyond the direct interaction between AGN power and the thermal energy of the intracluster medium. These observations suggest that the mechanisms governing gas dynamics in isolated and group central galaxies are likely influenced by additional factors.

5.1 NEXT STEPS

It is not so simple to build an assembly history for the stellar content of central galaxies. Many physical processes influence the formation and evolution of galaxies and using only analytical techniques becomes inconvenient, specially because we are capturing only a snapshot within a predominantly local universe. Using simulations and semi-analytical models together to try to describe the evolution of stellar content and gas deposition history has been widely used. The semi-analytical models use a set of analytical approximations that describe the physics involved in these processes of galaxy formation and evolution. On the other hand, simulations solve numerically the nonlinear equations that govern the same physical processes.

Therefore, comparing our findings with simulations is essential for a deeper understanding of the evolution of central galaxies. This comparison will allows us to observe the development of phenomena like early SFH, mergers, feedback processes and cooling mechanisms within these models and also to ensure that our parameterization is consistent with established in these models.

BIBLIOGRAPHY

Adami, C.; Biviano, A.; Mazure, A. Segregations in clusters of galaxies. **Astronomy and Astrophysics**, v. 331, p. 439–450, mar. 1998.

Adelman-McCarthy, J. K. et al. The Sixth Data Release of the Sloan Digital Sky Survey. **The Astrophysical Journal Supplement Series**, v. 175, p. 297–313, abr. 2008.

Alam, S. et al. The Eleventh and Twelfth Data Releases of the Sloan Digital Sky Survey: Final Data from SDSS-III. **The Astrophysical Journal Supplement Series**, v. 219, p. 12, jul. 2015.

Allen, S. W. et al. The relation between accretion rate and jet power in X-ray luminous elliptical galaxies. **Monthly Noticles of the Royal Astronomical Society**, v. 372, n. 1, p. 21–30, out. 2006.

Aragon-Salamanca, A.; Baugh, C. M.; Kauffmann, G. The K-band Hubble diagram for the brightest cluster galaxies: a test of hierarchical galaxy formation models. **Monthly Noticles of the Royal Astronomical Society**, v. 297, n. 2, p. 427–434, jun. 1998.

Bahcall, N. A. The relation between velocity dispersion and central galaxy density in clusters of galaxies. **The Astrophysical Journal**, v. 247, p. 787–791, ago. 1981.

Bai, L. et al. The Inside-out Growth of the Most Massive Galaxies at $0.3 < z < 0.9$. **The Astrophysical Journal**, v. 789, n. 2, p. 134, jul. 2014.

Baldi, R. D.; Capetti, A.; Giovannini, G. Pilot study of the radio-emitting AGN population: the emerging new class of FR 0 radio-galaxies. **Astronomy and Astrophysics**, v. 576, p. A38, abr. 2015.

Baldwin, J. A.; Phillips, M. M.; Terlevich, R. Classification parameters for the emission-line spectra of extragalactic objects. **Publications of the Astronomical Society of the Pacific**, v. 93, p. 5–19, fev. 1981.

Balmaverde, B.; Baldi, R. D.; Capetti, A. The accretion mechanism in low-power radio galaxies. **Astronomy and Astrophysics**, v. 486, n. 1, p. 119–130, jul. 2008.

Becker, R. H.; White, R. L.; Helfand, D. J. The FIRST Survey: Faint Images of the Radio Sky at Twenty Centimeters. **The Astrophysical Journal**, v. 450, p. 559, set. 1995.

Bertin, E.; Arnouts, S. SExtractor: Software for source extraction. **Astronomy and Astrophysics Supplement Series**, v. 117, p. 393–404, jun. 1996.

Best, P. N. et al. The host galaxies of radio-loud active galactic nuclei: mass dependences, gas cooling and active galactic nuclei feedback. **Monthly Noticles of the Royal Astronomical Society**, v. 362, n. 1, p. 25–40, set. 2005.

____. On the prevalence of radio-loud active galactic nuclei in brightest cluster galaxies: implications for AGN heating of cooling flows. **Monthly Noticles of the Royal Astronomical Society**, v. 379, n. 3, p. 894–908, ago. 2007.

Bialas, D. et al. On the occurrence of galaxy harassment. **Astronomy and Astrophysics**, v. 576, p. A103, abr. 2015.

Binette, L. et al. Photoionization in elliptical galaxies by old stars. **Astronomy and Astrophysics**, v. 292, p. 13–19, dez. 1994.

Blanton, M. R. et al. New York University Value-Added Galaxy Catalog: A Galaxy Catalog Based on New Public Surveys. **The Astronomical Journal**, v. 129, n. 6, p. 2562–2578, jun. 2005.

Bondi, H. On spherically symmetrical accretion. **Monthly Noticles of the Royal Astronomical Society**, v. 112, p. 195, 1952.

Bundy, K. et al. Overview of the SDSS-IV MaNGA Survey: Mapping nearby Galaxies at Apache Point Observatory. **The Astrophysical Journal**, v. 798, n. 1, p. 7, jan. 2015.

Butcher, H.; Oemler A., J. The evolution of galaxies in clusters. V. A study of populations since Z 0.5. **The Astrophysical Journal**, v. 285, p. 426–438, out. 1984.

Capaccioli, M.; Caon, N.; D'Onofrio, M. Families of galaxies in the mu.e-R.e plane. **Monthly Noticles of the Royal Astronomical Society**, v. 259, p. 323–327, nov. 1992.

Cardelli, J. A.; Clayton, G. C.; Mathis, J. S. The Relationship between Infrared, Optical, and Ultraviolet Extinction. **The Astrophysical Journal**, v. 345, p. 245, out. 1989.

Cardiel, N. **indexf: Line-strength Indices in Fully Calibrated FITS Spectra**. 2010. ascl:1010.046 p. Astrophysics Source Code Library, record ascl:1010.046.

Cardiel, N.; Gorgas, J.; Aragon-Salamanca, A. Spectral gradients in central cluster galaxies: further evidence of star formation in cooling flows. **Monthly Noticles of the Royal Astronomical Society**, v. 298, n. 4, p. 977–996, ago. 1998.

Carlberg, R. G. et al. The Average Mass Profile of Galaxy Clusters. **The Astrophysical Journal Letters**, v. 485, n. 1, p. L13–L16, ago. 1997.

Carter, D.; Metcalfe, N. The morphology of clusters of galaxies. **Monthly Noticles of the Royal Astronomical Society**, v. 191, p. 325–337, maio 1980.

Cavagnolo, K. W. et al. Intracluster Medium Entropy Profiles for a Chandra Archival Sample of Galaxy Clusters. **The Astrophysical Journal Supplement Series**, v. 182, n. 1, p. 12–32, maio 2009.

____. A Relationship Between AGN Jet Power and Radio Power. **The Astrophysical Journal**, v. 720, n. 2, p. 1066–1072, set. 2010.

Chandrasekhar, S. Dynamical Friction. I. General Considerations: the Coefficient of Dynamical Friction. **The Astrophysical Journal**, v. 97, p. 255, mar. 1943.

Charbonnel, C. et al. Grids of stellar models. III. From 0.8 to 120 Msolar at Z=0.004. **Astronomy and Astrophysics Supplement Series**, v. 101, p. 415, out. 1993.

Chon, G. et al. Discovery of an X-ray cavity near the radio lobes of Cygnus A indicating previous AGN activity. **Astronomy and Astrophysics**, v. 545, p. L3, set. 2012.

Chu, A.; Boldrini, P.; Silk, J. Off-centre supermassive black holes in bright central galaxies. **Monthly Noticles of the Royal Astronomical Society**, v. 522, n. 1, p. 948–955, jun. 2023.

Cid Fernandes, R. et al. Semi-empirical analysis of Sloan Digital Sky Survey galaxies - I. Spectral synthesis method. **Monthly Noticles of the Royal Astronomical Society**, v. 358, p. 363–378, abr. 2005.

____. Resolving galaxies in time and space. I. Applying STARLIGHT to CALIFA datacubes. **Astronomy and Astrophysics**, v. 557, p. A86, set. 2013.

____. A comprehensive classification of galaxies in the Sloan Digital Sky Survey: how to tell true from fake AGN? **Monthly Noticles of the Royal Astronomical Society**, v. 413, n. 3, p. 1687–1699, maio 2011.

____. A comprehensive classification of galaxies in the Sloan Digital Sky Survey: how to tell true from fake AGN? **Monthly Noticles of the Royal Astronomical Society**, v. 413, n. 3, p. 1687–1699, maio 2011.

____. Alternative diagnostic diagrams and the 'forgotten' population of weak line galaxies in the SDSS. **Monthly Noticles of the Royal Astronomical Society**, v. 403, n. 2, p. 1036–1053, abr. 2010.

Ciddor, P. E. Refractive index of air: new equations for the visible and near infrared. **Applied Optics**, v. 35, n. 9, p. 1566, mar. 1996.

Cimatti, A.; Fraternali, F.; Nipoti, C. Introduction to Galaxy Formation and Evolution. From Primordial Gas to Present-Day Galaxies. **arXiv e-prints**, p. arXiv:1912.06216, dez. 2019.

Conselice, C. J.; Gallagher JOHN S., I.; Wyse, R. F. G. On the Nature of the NGC 1275 System. **The Astronomical Journal**, v. 122, n. 5, p. 2281–2300, nov. 2001.

Couch, W. J. et al. Morphological Studies of the Galaxy Populations in Distant "Butcher-Oemler" Clusters with HST. I. AC 114 at Z = 0.31 and Abell 370 at Z = 0.37. **The Astrophysical Journal**, v. 430, p. 121, jul. 1994.

Croton, D. J. et al. The many lives of active galactic nuclei: cooling flows, black holes and the luminosities and colours of galaxies. **Monthly Noticles of the Royal Astronomical Society**, v. 365, p. 11–28, jan. 2006.

de Carvalho, R. R. et al. Investigating the Relation between Galaxy Properties and the Gaussianity of the Velocity Distribution of Groups and Clusters. **The Astronomical Journal**, v. 154, n. 3, p. 96, set. 2017.

De Lucia, G.; Blaizot, J. The hierarchical formation of the brightest cluster galaxies. **Monthly Noticles of the Royal Astronomical Society**, v. 375, n. 1, p. 2–14, fev. 2007.

De Lucia, G. et al. The formation history of elliptical galaxies. **Monthly Noticles of the Royal Astronomical Society**, v. 366, n. 2, p. 499–509, fev. 2006.

Donzelli, C. J.; Muriel, H.; Madrid, J. P. The Luminosity Profiles of Brightest Cluster Galaxies. **The Astrophysical Journal Supplement Series**, v. 195, n. 2, p. 15, ago. 2011.

Dressler, A. A comprehensive study of 12 very rich clusters of galaxies. I. Photometric technique and analysis of the luminosity function. **The Astrophysical Journal**, v. 223, p. 765–787, ago. 1978.

____. The dynamics and structure of the cD galaxy in Abell 2029. **The Astrophysical Journal**, v. 231, p. 659–670, ago. 1979.

____. Galaxy morphology in rich clusters - Implications for the formation and evolution of galaxies. **The Astrophysical Journal**, v. 236, p. 351–365, mar. 1980.

Dressler, A. et al. Evolution since z = 0.5 of the Morphology-Density Relation for Clusters of Galaxies. **The Astrophysical Journal**, v. 490, n. 2, p. 577–591, dez. 1997.

Erfanianfar, G. et al. Stellar mass-halo mass relation for the brightest central galaxies of X-ray clusters since z $\sim$ 0.65. **Astronomy and Astrophysics**, v. 631, p. A175, nov. 2019.

Fabian, A. C. Cooling Flows in Clusters of Galaxies. **Annual Review of Astronomy and Astrophysics**, v. 32, p. 277–318, jan. 1994.

Fanaroff, B. L.; Riley, J. M. The morphology of extragalactic radio sources of high and low luminosity. **Monthly Noticles of the Royal Astronomical Society**, v. 167, p. 31P–36P, maio 1974.

Farouki, R.; Shapiro, S. L. Computer simulations of environmental influences on galaxy evolution in dense clusters. II - Rapid tidal encounters. **The Astrophysical Journal**, v. 243, p. 32–41, jan. 1981.

Fujita, Y.; Kawakatu, N.; Shlosman, I. AGN jet power and feedback characterised by Bondi accretion in brightest cluster galaxies. **arXiv e-prints**, p. arXiv:1406.6366, jun. 2014.

Gaspari, M.; Brighenti, F.; Ruszkowski, M. Solving the cooling flow problem through mechanical AGN feedback. **Astronomische Nachrichten**, v. 334, p. 394, abr. 2013.

Girardi, L. et al. Evolutionary tracks and isochrones for low- and intermediate-mass stars: From 0.15 to 7 M_{sun}, and from Z=0.0004 to 0.03. **Astronomy and Astrophysics Supplement Series**, v. 141, p. 371–383, fev. 2000.

Gomez, P. L. et al. Do Cluster Cooling Flows Survive Head-on Galaxy Cluster Mergers? **arXiv e-prints**, p. astro–ph/0009465, set. 2000.

González Delgado, R. M. et al. Evolutionary stellar population synthesis at high spectral resolution: optical wavelengths. **Monthly Noticles of the Royal Astronomical Society**, v. 357, n. 3, p. 945–960, mar. 2005.

____. The CALIFA survey across the Hubble sequence. Spatially resolved stellar population properties in galaxies. **Astronomy and Astrophysics**, v. 581, p. A103, set. 2015.

Graham, A. W.; Guzmán, R. HST Photometry of Dwarf Elliptical Galaxies in Coma, and an Explanation for the Alleged Structural Dichotomy between Dwarf and Bright Elliptical Galaxies. **The Astronomical Journal**, v. 125, n. 6, p. 2936–2950, jun. 2003.

Gunn, J. E.; Gott J. RICHARD, I. On the Infall of Matter Into Clusters of Galaxies and Some Effects on Their Evolution. **The Astrophysical Journal**, v. 176, p. 1, ago. 1972.

Gunn, J. E. et al. The 2.5 m Telescope of the Sloan Digital Sky Survey. **The Astronomical Journal**, v. 131, n. 4, p. 2332–2359, Apr 2006.

Hardcastle, M. J.; Evans, D. A.; Croston, J. H. Hot and cold gas accretion and feedback in radio-loud active galaxies. **Monthly Noticles of the Royal Astronomical Society**, v. 376, n. 4, p. 1849–1856, abr. 2007.

Hashimoto, Y.; Henry, J. P.; Boehringer, H. Multiwavelength investigations of co-evolution of bright cluster galaxies and their host clusters. **Monthly Noticles of the Royal Astronomical Society**, v. 440, n. 1, p. 588–600, maio 2014.

Herpich, F. et al. The many faces of LINER-like galaxies: a WISE view. **Monthly Noticles of the Royal Astronomical Society**, v. 462, n. 2, p. 1826–1833, out. 2016.

Hine, R. G.; Longair, M. S. Optical spectra of 3CR radio galaxies. **Monthly Noticles of the Royal Astronomical Society**, v. 188, p. 111–130, jul. 1979.

Hubble, E.; Humason, M. L. The Velocity-Distance Relation among Extra-Galactic Nebulae. **The Astrophysical Journal**, v. 74, p. 43, jul. 1931.

Katayama, H. et al. Properties of the Brightest Cluster Galaxy and Its Host Cluster. **The Astrophysical Journal**, v. 585, n. 2, p. 687–693, mar. 2003.

Kauffmann, G. et al. The host galaxies of active galactic nuclei. **Monthly Noticles of the Royal Astronomical Society**, v. 346, n. 4, p. 1055–1077, dez. 2003.

Kewley, L. J. et al. Theoretical Modeling of Starburst Galaxies. **The Astrophysical Journal**, v. 556, n. 1, p. 121–140, jul. 2001.

____. The host galaxies and classification of active galactic nuclei. **Monthly Noticles of the Royal Astronomical Society**, v. 372, n. 3, p. 961–976, nov. 2006.

Kormendy, J.; Ho, L. C. Coevolution (Or Not) of Supermassive Black Holes and Host Galaxies. **Annual Review of Astronomy and Astrophysics**, v. 51, p. 511–653, ago. 2013.

La Barbera, F. et al. SPIDER - I. Sample and galaxy parameters in the grizYJHK wavebands. **Monthly Noticles of the Royal Astronomical Society**, v. 408, n. 3, p. 1313–1334, nov. 2010.

____. SPIDER VIII - constraints on the stellar initial mass function of early-type galaxies from a variety of spectral features. **Monthly Noticles of the Royal Astronomical Society**, v. 433, n. 4, p. 3017–3047, ago. 2013.

____. SPIDER - X. Environmental effects in central and satellite early-type galaxies through the stellar fossil record. **Monthly Noticles of the Royal Astronomical Society**, v. 445, p. 1977–1996, dez. 2014.

Laporte, C. F. P. et al. The growth in size and mass of cluster galaxies since z = 2. **Monthly Noticles of the Royal Astronomical Society**, v. 435, n. 2, p. 901–909, out. 2013.

Larson, R. B.; Tinsley, B. M.; Caldwell, C. N. The evolution of disk galaxies and the origin of S0 galaxies. **The Astrophysical Journal**, v. 237, p. 692–707, maio 1980.

Lequeux, J. et al. Chemical Composition and Evolution of Irregular and Blue Compact Galaxies. **Astronomy and Astrophysics**, v. 80, p. 155, dez. 1979.

Lidman, C. et al. The importance of major mergers in the build up of stellar mass in brightest cluster galaxies at z = 1. **Monthly Noticles of the Royal Astronomical Society**, v. 433, n. 1, p. 825–837, jul. 2013.

____. Evidence for significant growth in the stellar mass of brightest cluster galaxies over the past 10 billion years. **Monthly Noticles of the Royal Astronomical Society**, v. 427, n. 1, p. 550–568, nov. 2012.

Lintott, C. et al. Galaxy Zoo 1: data release of morphological classifications for nearly 900 000 galaxies. **Monthly Noticles of the Royal Astronomical Society**, v. 410, p. 166–178, jan. 2011.

Lorenzoni, V.; Rembold, S. B.; de Carvalho, R. R. Probing stellar populations and interstellar medium in early-type central galaxies. **Monthly Noticles of the Royal Astronomical Society**, v. 527, n. 2, p. 3542–3558, jan. 2024.

Loubser, S. I. et al. Stellar populations in the centres of brightest cluster galaxies. **Monthly Noticles of the Royal Astronomical Society**, v. 398, p. 133–156, set. 2009.

Lubin, L. M.; Bahcall, N. A. The Relation between Velocity Dispersion and Temperature in Clusters: Limiting the Velocity Bias. **The Astrophysical Journal Letters**, v. 415, p. L17, set. 1993.

Magorrian, J. et al. The Demography of Massive Dark Objects in Galaxy Centers. **The Astronomical Journal**, v. 115, n. 6, p. 2285–2305, jun. 1998.

McDonald, M. et al. On the Origin of the Extended Hα Filaments in Cooling Flow Clusters. **The Astrophysical Journal**, v. 721, n. 2, p. 1262–1283, out. 2010.

____. Star Formation Efficiency in the Cool Cores of Galaxy Clusters. **The Astrophysical Journal**, v. 734, n. 2, p. 95, jun. 2011.

McNamara, B. R.; Nulsen, P. E. J. Heating Hot Atmospheres with Active Galactic Nuclei. **Annual Review of Astronomy and Astrophysics**, v. 45, n. 1, p. 117–175, set. 2007.

McNamara, B. R.; O'Connell, R. W. Star formation in cooling flows in clusters of galaxies. **The Astronomical Journal**, v. 98, p. 2018–2043, dez. 1989.

McNamara, B. R.; Rohanizadegan, M.; Nulsen, P. E. J. Are Radio Active Galactic Nuclei Powered by Accretion or Black Hole Spin? **The Astrophysical Journal**, v. 727, n. 1, p. 39, jan. 2011.

McNamara, B. R. et al. Optical Structure in the Abell 1795 Cluster Central Galaxy: Evidence for Stripping and Deflection of Radio Jets. **The Astrophysical Journal Letters**, v. 466, p. L9, jul. 1996.

Merritt, D. Relaxation and tidal stripping in rich clusters of galaxies. I. Evolution of the mass distribution. **The Astrophysical Journal**, v. 264, p. 24–48, jan. 1983.

____. Relaxation and tidal stripping in rich clusters of galaxies. III. Growth of a massive central galaxy. **The Astrophysical Journal**, v. 289, p. 18–32, fev. 1985.

Molendi, S.; Pizzolato, F. Is the Gas in Cooling Flows Multiphase? **The Astrophysical Journal**, v. 560, n. 1, p. 194–200, out. 2001.

Moore, B. et al. Galaxy harassment and the evolution of clusters of galaxies. **Nature**, v. 379, n. 6566, p. 613–616, fev. 1996.

Navarro, J. F.; Frenk, C. S.; White, S. D. M. A Universal Density Profile from Hierarchical Clustering. **The Astrophysical Journal**, v. 490, n. 2, p. 493–508, dez. 1997.

Nikutta, R. et al. The meaning of WISE colours - I. The Galaxy and its satellites. **Monthly Noticles of the Royal Astronomical Society**, v. 442, n. 4, p. 3361–3379, ago. 2014.

Nipoti, C. The special growth history of central galaxies in groups and clusters. **Monthly Noticles of the Royal Astronomical Society**, v. 467, n. 1, p. 661–673, maio 2017.

Novak, M. et al. The VLA-COSMOS 3 GHz Large Project: Cosmic star formation history since z 5. **Astronomy and Astrophysics**, v. 602, p. A5, jun. 2017.

O'Dea, C. P. et al. An Infrared Survey of Brightest Cluster Galaxies. II. Why are Some Brightest Cluster Galaxies Forming Stars? **The Astrophysical Journal**, v. 681, n. 2, p. 1035–1045, jul. 2008.

Osterbrock, D. E. **Astrophysics of gaseous nebulae and active galactic nuclei**. [S.l.: s.n.], 1989.

Ostriker, J. P.; Hausman, M. A. Cannibalism among the galaxies: dynamically produced evolution of cluster luminosity functions. **The Astrophysical Journal Letters**, v. 217, p. L125–L129, nov. 1977.

____. Cannibalism among the galaxies: dynamically produced evolution of cluster luminosity functions. **The Astrophysical Journal Letters**, v. 217, p. L125–L129, nov. 1977.

Oyarzún, G. A. et al. SDSS-IV MaNGA: How the Stellar Populations of Passive Central Galaxies Depend on Stellar and Halo Mass. **The Astrophysical Journal**, v. 933, n. 1, p. 88, jul. 2022.

Padmanabhan, N. et al. An Improved Photometric Calibration of the Sloan Digital Sky Survey Imaging Data. **The Astrophysical Journal**, v. 674, n. 2, p. 1217–1233, fev. 2008.

Pasini, T. et al. A First Chandra View of the Cool Core Cluster A1668: Offset Cooling and AGN Feedback Cycle. **The Astrophysical Journal**, v. 911, n. 1, p. 66, abr. 2021.

Peng, Y.; Maiolino, R.; Cochrane, R. Strangulation as the primary mechanism for shutting down star formation in galaxies. **Nature**, v. 521, n. 7551, p. 192–195, maio 2015.

Plionis, M.; Tovmassian, H. M.; Andernach, H. Richness dependence of the recent evolution of clusters of galaxies. **Monthly Noticles of the Royal Astronomical Society**, v. 395, n. 1, p. 2–10, maio 2009.

Ragone-Figueroa, C. et al. Evolution and role of mergers in the BCG-cluster alignment. A view from cosmological hydrosimulations. **Monthly Noticles of the Royal Astronomical Society**, v. 495, n. 2, p. 2436–2445, jun. 2020.

Revaz, Y.; Combes, F.; Salomé, P. Formation of cold filaments in cooling flow clusters. **Astronomy and Astrophysics**, v. 477, n. 3, p. L33–L36, jan. 2008.

Ricarte, A. et al. A Link between Ram Pressure Stripping and Active Galactic Nuclei. **The Astrophysical Journal Letters**, v. 895, n. 1, p. L8, maio 2020.

Ritchie, B. W.; Thomas, P. A. Hydrodynamic simulations of merging clusters of galaxies. **Monthly Noticles of the Royal Astronomical Society**, v. 329, n. 3, p. 675–688, jan. 2002.

Ruszkowski, M.; Oh, S. P. Galaxy motions, turbulence and conduction in clusters of galaxies. **Monthly Noticles of the Royal Astronomical Society**, v. 414, n. 2, p. 1493–1507, jun. 2011.

Ruszkowski, M.; Springel, V. The Role of Dry Mergers for the Formation and Evolution of Brightest Cluster Galaxies. **The Astrophysical Journal**, v. 696, n. 2, p. 1094–1102, maio 2009.

Salomé, P.; Combes, F. Mapping the cold molecular gas in a cooling flow cluster: Abell 1795. **Astronomy and Astrophysics**, v. 415, p. L1–L5, fev. 2004.

Salomé, P. et al. Cold molecular gas in the Perseus cluster core. Association with X-ray cavity, Hα filaments and cooling flow. **Astronomy and Astrophysics**, v. 454, n. 2, p. 437–445, ago. 2006.

Sandage, A.; Hardy, E. The Redshift-Distance Relation. VII Absolute Magnitudes on the First Three Ranked Cluster Galaxies as Functions of Cluster Richness and Bautz-Morgan Cluster Type: the Effect of q_{o}. **The Astrophysical Journal**, v. 183, p. 743–758, ago. 1973.

Sarzi, M. et al. The SAURON project - XVI. On the sources of ionization for the gas in elliptical and lenticular galaxies. **Monthly Noticles of the Royal Astronomical Society**, v. 402, n. 4, p. 2187–2210, mar. 2010.

Schaerer, D. et al. Grids of stellar models. IV. From 0.8 to 120 M_solar at Z=0.040. **Astronomy and Astrophysics Supplement Series**, v. 102, p. 339, dez. 1993.

____. Grids of stellar models. II. From 0.8 to 120 M_solar at Z=0.008. **Astronomy and Astrophysics Supplement Series**, v. 98, p. 523, maio 1993.

Schaller, G. et al. New Grids of Stellar Models from 0.8-SOLAR-MASS to 120-SOLAR-MASSES at Z=0.020 and Z=0.001. **Astronomy and Astrophysics Supplement Series**, v. 96, p. 269, dez. 1992.

Schawinski, K. et al. Observational evidence for AGN feedback in early-type galaxies. **Monthly Noticles of the Royal Astronomical Society**, v. 382, n. 4, p. 1415–1431, dez. 2007.

Scholz-Díaz, L.; Martín-Navarro, I.; Falcón-Barroso, J. The dark side of galaxy stellar populations - I. The stellar-to-halo mass relation and the velocity dispersion-halo mass relation. **Monthly Noticles of the Royal Astronomical Society**, v. 511, n. 4, p. 4900–4920, abr. 2022.

Schombert, J. M. The Structure of Brightest Cluster Members. I. Surface Photometry. **The Astrophysical Journal Supplement Series**, v. 60, p. 603, mar. 1986.

Silpa, S. et al. Probing the origin of low-frequency radio emission in PG quasars with the uGMRT - I. **Monthly Noticles of the Royal Astronomical Society**, v. 499, n. 4, p. 5826–5839, dez. 2020.

Stasińska, G. et al. Semi-empirical analysis of Sloan Digital Sky Survey galaxies - III. How to distinguish AGN hosts. **Monthly Noticles of the Royal Astronomical Society**, v. 371, n. 2, p. 972–982, set. 2006.

____. Can retired galaxies mimic active galaxies? Clues from the Sloan Digital Sky Survey. **Monthly Noticles of the Royal Astronomical Society**, v. 391, n. 1, p. L29–L33, nov. 2008.

Steinhauser, D.; Schindler, S.; Springel, V. Simulations of ram-pressure stripping in galaxy-cluster interactions. **Astronomy and Astrophysics**, v. 591, p. A51, jun. 2016.

Stott, J. P. et al. The XMM Cluster Survey: the interplay between the brightest cluster galaxy and the intracluster medium via AGN feedback. **Monthly Noticles of the Royal Astronomical Society**, v. 422, p. 2213–2229, maio 2012.

Takizawa, M. A Two-Temperature Model of the Intracluster Medium. In: Makishima, K.; Piro, L.; Takahashi, T. (Ed.). **Broad Band X-ray Spectra of Cosmic Sources**. [S.l.: s.n.], 2000. p. 621.

Tiwari, J.; Singh, K. P. The complex intracluster medium of Abell 1569 and its interaction with central radio galaxies. **Monthly Noticles of the Royal Astronomical Society**, v. 509, n. 3, p. 3321–3338, jan. 2022.

Toomre, A.; Toomre, J. Galactic Bridges and Tails. **The Astrophysical Journal**, v. 178, p. 623–666, dez. 1972.

Trager, S. C. et al. Old Stellar Populations. VI. Absorption-Line Spectra of Galaxy Nuclei and Globular Clusters. **The Astrophysical Journal Supplement Series**, v. 116, n. 1, p. 1–28, jan. 1998.

Tremonti, C. A. et al. The Origin of the Mass-Metallicity Relation: Insights from 53,000 Star-forming Galaxies in the Sloan Digital Sky Survey. **The Astrophysical Journal**, v. 613, n. 2, p. 898–913, out. 2004.

Trussler, J. et al. Starvation as the primary quenching mechanism in galaxies. **arXiv e-prints**, nov. 2018.

Vagshette, N. D. et al. Detection of a pair of prominent X-ray cavities in Abell 3847. **Monthly Noticles of the Royal Astronomical Society**, v. 466, n. 2, p. 2054–2066, abr. 2017.

Valdarnini, R.; Sarazin, C. L. A study of cool core resiliency and entropy mixing in simulations of galaxy cluster mergers. **Monthly Noticles of the Royal Astronomical Society**, v. 504, n. 4, p. 5409–5436, jul. 2021.

van den Bosch, F. C. et al. Satellite Ecology: The Dearth of Environment Dependence. **arXiv e-prints**, p. arXiv:0805.0002, maio 2008.

van der Marel, R. P. et al. The Velocity and Mass Distribution of Clusters of Galaxies from the CNOC1 Cluster Redshift Survey. **The Astronomical Journal**, v. 119, n. 5, p. 2038–2052, maio 2000.

Vazdekis, A. et al. Evolutionary stellar population synthesis with MILES - I. The base models and a new line index system. **Monthly Noticles of the Royal Astronomical Society**, v. 404, n. 4, p. 1639–1671, jun. 2010.

Veilleux, S.; Osterbrock, D. E. Spectral Classification of Emission-Line Galaxies. **The Astrophysical Journal Supplement Series**, v. 63, p. 295, fev. 1987.

Voit, G. M.; Donahue, M. Cooling Time, Freefall Time, and Precipitation in the Cores of ACCEPT Galaxy Clusters. **The Astrophysical Journal Letters**, v. 799, n. 1, p. L1, jan. 2015.

Von Der Linden, A. et al. How special are brightest group and cluster galaxies? **Monthly Noticles of the Royal Astronomical Society**, v. 379, p. 867–893, ago. 2007.

White, S. D. M. Dynamical friction in spherical clusters. **Monthly Noticles of the Royal Astronomical Society**, v. 174, p. 19–28, jan. 1976.

Wilson, A. S.; Colbert, E. J. M. The Difference between Radio-loud and Radio-quiet Active Galaxies. **The Astrophysical Journal**, v. 438, p. 62, jan. 1995.

Yang, X. et al. Galaxy Groups in the SDSS DR4. I. The Catalog and Basic Properties. **The Astrophysical Journal**, v. 671, p. 153–170, dez. 2007.

____. An Analytical Model for the Accretion of Dark Matter Subhalos. **The Astrophysical Journal**, v. 741, p. 13, nov. 2011.

Yuan, Z. S.; Han, J. L.; Wen, Z. L. Radio luminosity function of brightest cluster galaxies. **Monthly Noticles of the Royal Astronomical Society**, v. 460, n. 4, p. 3669–3678, ago. 2016.

Zhao, D.; Aragón-Salamanca, A.; Conselice, C. J. Evolution of the brightest cluster galaxies: the influence of morphology, stellar mass and environment. **Monthly Noticles of the Royal Astronomical Society**, v. 453, n. 4, p. 4444–4455, nov. 2015.

____. The link between morphology and structure of brightest cluster galaxies: automatic identification of cDs. **Monthly Noticles of the Royal Astronomical Society**, v. 448, n. 3, p. 2530–2545, abr. 2015.

6 APPENDIX

Table 1 – Number of Galaxies (Signal-to-noise ratio) per bin of σ and $M_{\rm halo}$ in the full sample.

	$\log M_{\rm halo}/{\rm M}_\odot$							
	11.60	12.00	12.25	12.50	13.00	13.50	14.00	14.30
σ (km s^{-1})	12.00	12.25	12.50	13.00	13.50	14.00	14.30	15.30
100-110	318 (289)	167 (220)	34 (107)					
110-120	458 (355)	359 (336)	105 (186)	24 (96)				
120-130	506 (392)	499 (396)	168 (245)	40 (127)	5 (74)			
130-140	467 (380)	679 (476)	324 (350)	98 (192)	6 (59)			
140-150	334 (330)	639 (483)	365 (385)	145 (258)	9 (71)			
150-160	248 (305)	617 (497)	520 (459)	243 (319)	21 (101)			
160-170	126 (220)	451 (435)	468 (461)	336 (395)	37 (136)			
170-180	69 (169)	293 (359)	428 (451)	374 (427)	50 (165)	9 (86)		
180-190	45 (142)	212 (311)	344 (421)	445 (474)	83 (219)	6 (77)		
190-200	20 (102)	104 (217)	215 (331)	380 (449)	91 (232)	23 (107)		
200-210	13 (83)	60 (170)	162 (313)	389 (465)	151 (311)	28 (146)		
210-230	14 (98)	42 (149)	114 (267)	448 (538)	306 (460)	78 (241)	6 (82)	6 (93)
230-323		24 (134)	30 (147)	301 (458)	383 (554)	231 (452)	51 (220)	26 (159)

Tables 1 to 3 present the numbers of central galaxies per σ and $M_{\rm halo}$ bin, along with the S/N (in parentheses) for the full sample, isolated, and group centrals respectively.

In Figure 1, we compare the results from Figure 3.2 (represented by dashed lines) to the results obtained using GM templates (solid lines). While the parameter values vary as expected, the trends with σ and $M_{\rm halo}$ are very similar.

Figure 2 presents the BPT and WHAN diagnostic diagrams for isolated (blue dots) and group (red dots) centrals. For both the BPT and WHAN diagram, the results for both samples remain consistent with Figure 4.2.

Table 2 – Number of Galaxies (Signal-to-noise ratio) per bin of σ and $M_{\rm halo}$ for the isolated centrals.

	$\log M_{\rm halo}/{\rm M}_\odot$							
	11.60	12.00	12.25	12.50	13.00	13.50	14.00	14.30
σ (km s^{-1})	12.00	12.25	12.50	13.00	13.50	14.00	14.30	15.30
100-110	292 (276)	148 (208)	18 (80)					
110-120	423 (339)	329 (324)	81 (165)					
120-130	458 (373)	454 (379)	128 (211)	14 (80)				
130-140	432 (364)	616 (451)	244 (300)	50 (152)				
140-150	303 (313)	564 (455)	312 (358)	67 (178)				
150-160	221 (289)	569 (475)	425 (415)	128 (228)				
160-170	115 (210)	412 (414)	384 (415)	182 (289)				
170-180	65 (164)	257 (333)	356 (412)	207 (311)				
180-190	41 (135)	183 (288)	283 (381)	269 (376)	5 (73)			
190-200	16 (92)	93 (204)	172 (295)	241 (356)	6 (90)			
200-210	13 (83)	56 (164)	123 (272)	217 (351)	13 (99)			
210-230	14 (98)	39 (142)	91 (238)	250 (393)	33 (157)			
230-323		20 (123)	23 (129)	182 (350)	56 (201)			

Table 3 – Number of Galaxies (Signal-to-noise ratio) per bin of σ and $M_{\rm halo}$ for the group centrals.

	$\log M_{\rm halo}/{\rm M}_\odot$							
	11.60	12.00	12.25	12.50	13.00	13.50	14.00	14.30
σ (km s^{-1})	12.00	12.25	12.50	13.00	13.50	14.00	14.30	15.30
100-110	14 (67)	10 (66)	12 (67)					
110-120	15 (82)	18 (80)	20 (84)	18 (86)				
120-130	16 (81)	24 (95)	33 (118)	26 (105)				
130-140	13 (78)	38 (125)	67 (172)	45 (123)	6 (59)			
140-150	17 (92)	38 (114)	42 (129)	70 (179)	9 (71)			
150-160	16 (81)	31 (121)	71 (171)	109 (222)	20 (98)			
160-170		28 (120)	66 (183)	142 (263)	36 (134)			
170-180		24 (118)	50 (161)	151 (283)	45 (155)	9 (86)		
180-190		15 (92)	44 (160)	160 (282)	74 (208)	6 (77)		
190-200		9 (86)	36 (147)	122 (259)	84 (220)	21 (101)		
200-210			29 (142)	156 (295)	132 (291)	27 (143)		
210-230			19 (117)	175 (353)	262 (425)	73 (235)	6 (82)	6 (93)
230-323				105 (287)	308 (503)	218 (437)	49 (217)	24 (156)

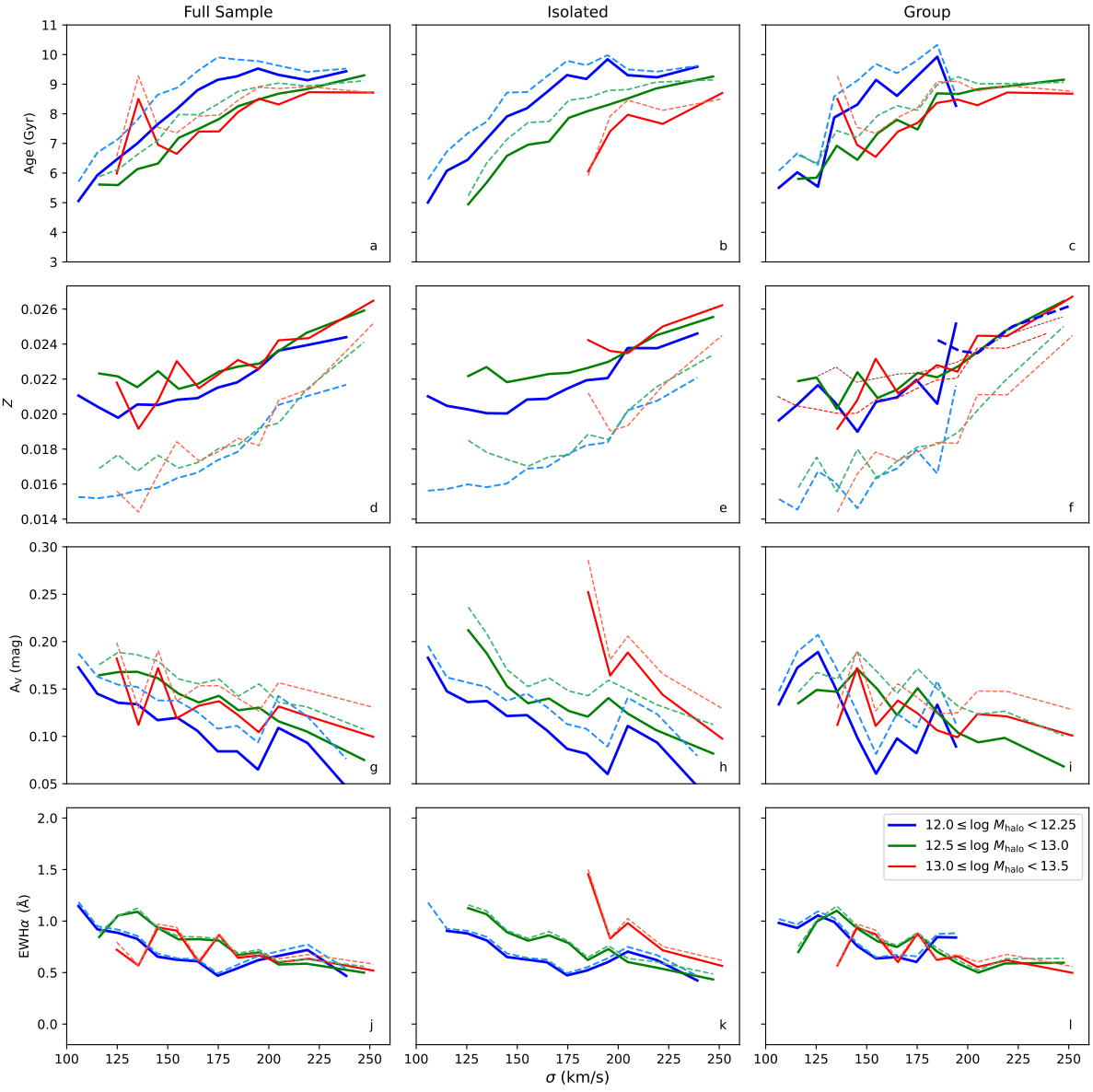

Figure 1 – Relation between Age, Z, A_V, and EWHα with σ, represented from top to bottom, respectively, for GM templates (solid lines) in comparison to MILES models (dashed lines). The full sample, along with ICs and GCs, is presented from left to right, respectively. Additionally, we included three M_{halo} ranges, distinguished by colors.

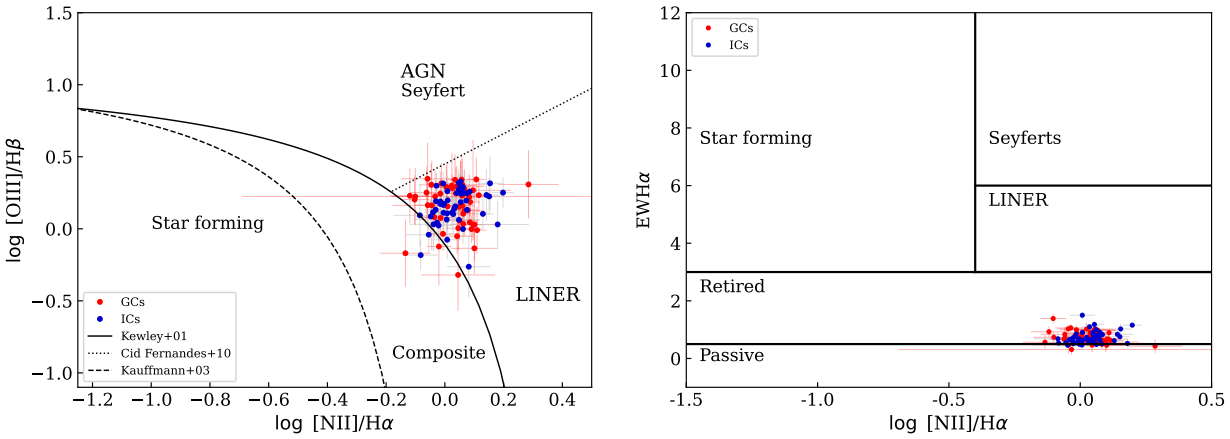

Figure 2 – The left panel shows the BPT diagram for ICs (blue dots) and GCs (red dots), which reveals that the dominant ionization pattern for central galaxies in both sub-samples is LINER, albeit with some cases exhibiting high uncertainty. In the right panel, the WHAN diagram indicates that HOLMES are the typical ionization source for ICs and GCs.